

PERFORMANCE EVALUATION OF LINEAR TUBE SOLAR RECEIVER AS  
STRATIFIED FLOW VAPOR GENERATOR/SEPARATOR FOR ABSORPTION  
MACHINES USING  $NH_3/LiNO_3$

A THESIS SUBMITTED TO  
THE GRADUATE SCHOOL OF NATURAL AND APPLIED SCIENCES  
OF  
MIDDLE EAST TECHNICAL UNIVERSITY

BY

SITKI BERAT ÇELİK

IN PARTIAL FULFILLMENT OF THE REQUIREMENTS  
FOR  
THE DEGREE OF DOCTOR OF PHILOSOPHY  
IN  
MECHANICAL ENGINEERING

SEPTEMBER 2020



Approval of the thesis:

**PERFORMANCE EVALUATION OF LINEAR TUBE SOLAR RECEIVER  
AS STRATIFIED FLOW VAPOR GENERATOR/SEPARATOR FOR  
ABSORPTION MACHINES USING  $NH_3/LiNO_3$**

submitted by **SITKI BERAT ÇELİK** in partial fulfillment of the requirements for the degree of **Doctor of Philosophy in Mechanical Engineering Department, Middle East Technical University** by,

Prof. Dr. Halil Kalıpçılar  
Dean, Graduate School of **Natural and Applied Sciences**

\_\_\_\_\_

Prof. Dr. M. A. Sahir Arıkan  
Head of Department, **Mechanical Engineering**

\_\_\_\_\_

Prof. Dr. İlker Tarı  
Supervisor, **Mechanical Engineering, METU**

\_\_\_\_\_

Prof. Dr. Antonio Lecuona Neumann  
Co-supervisor, **Fluid and Thermal Engineering, UC3M**

\_\_\_\_\_

**Examining Committee Members:**

Prof. Dr. Derek Baker  
Mechanical Engineering, METU

\_\_\_\_\_

Prof. Dr. İlker Tarı  
Mechanical Engineering, METU

\_\_\_\_\_

Assist. Prof. Dr. Ali Karakuş  
Mechanical Engineering, METU

\_\_\_\_\_

Prof. Dr. Atilla Bıyıkoglu  
Mechanical Engineering, Gazi University

\_\_\_\_\_

Prof. Dr. Maria Carmen Rodriguez Hidalgo  
Escuela Tecnica Superior de Ingenieros Navales, UPM

\_\_\_\_\_

Date: 15.09.2020

**I hereby declare that all information in this document has been obtained and presented in accordance with academic rules and ethical conduct. I also declare that, as required by these rules and conduct, I have fully cited and referenced all material and results that are not original to this work.**

Name, Surname: Sıtkı Berat Çelik

Signature :



## ABSTRACT

### **PERFORMANCE EVALUATION OF LINEAR TUBE SOLAR RECEIVER AS STRATIFIED FLOW VAPOR GENERATOR/SEPARATOR FOR ABSORPTION MACHINES USING $NH_3/LiNO_3$**

Çelik, Sıtkı Berat

Ph.D., Department of Mechanical Engineering

Supervisor: Prof. Dr. İlker Tarı

Co-Supervisor: Prof. Dr. Antonio Lecuona Neumann

September 2020, 129 pages

A parabolic trough solar collector acting as a desorber (vapor separator) has been recently suggested (Lecuona-Neumann, Rosner, & Ventas-Garzón, 2016) and (Famiglietti et al. 2018). The desorber significantly reduced the complexity and cost of a solar driven absorption heat pump. However, it introduced an innovative flow layout, which is a two-phase, boiling, gravity driven and stratified counter flow. The comprehension of its capabilities is necessary in order to unveil its potential. In the current work, a simplified assumption of the complex flow is suggested and implemented in finite difference and thermodynamic simulations of a single-effect absorption cycle acting as an air cooled chiller using  $NH_3/LiNO_3$  as the working fluid. The performance of the cycle has been investigated for satisfying the cooling demand of a representative living apartment in the Mediterranean climate. The results of the simulations are compared with experimental data.

Keywords: Absorption, Solar energy, Solar Cooling

## ÖZ

### **$NH_3/LiNO_3$ KULLANARAK ABSORPSİYON MAKİNELERİ İÇİN ÇOK FAZLI BUHAR ÜRETİCİSİ/AYRIŞTIRICISI OLARAK ÇİZGİSEL GÜNEŞ ALICISININ PERFORMAN DEĞERLENDİRMESİ**

Çelik, Sıtkı Berat

Doktora, Makina Mühendisliği Bölümü

Tez Yöneticisi: Prof. Dr. İlker Tarı

Ortak Tez Yöneticisi: Prof. Dr. Antonio Lecuona Neumann

Eylül 2020 , 129 sayfa

Desorber görevi gören bir parabolik oluklu güneş kolektörü (buhar ayırıcı) yakın zamanda önerilmiştir (Lecuona-Neumann, Rosner, & Ventas-Garzón, 2016) ve (Famiglietti ve ark.2018). Desorber, güneş enerjisiyle çalışan bir emme ısı pompasının karmaşıklığını ve maliyetini önemli ölçüde azalttı. Bununla birlikte, iki fazlı, kaynama, yerçekimi ile çalışan ve tabakalı karşı akış olan yenilikçi bir akış düzeni tanıttı. Potansiyelini ortaya çıkarmak için yeteneklerinin anlaşılması gereklidir. Mevcut çalışmada, karmaşık akışın basitleştirilmiş bir varsayımı önerilmektedir ve çalışma sıvısı olarak  $NH_3/LiNO_3$  kullanılarak hava soğutmalı bir soğutucu olarak işlev gören tek etkili bir emme döngüsünün sonlu eleman ve termodinamik simülasyonlarında uygulanmaktadır. Döngünün performansı, Akdeniz ikliminde temsili bir yaşam dairesinin soğutma talebini karşılamak için araştırılmıştır. Simülasyonların sonuçları deneysel verilerle karşılaştırılmıştır.

Anahtar Kelimeler: Absorpsiyon, Güneş Enerjisi, Güneşle Soğurma

For the memory of Dr. Cemil Yamalı

## ACKNOWLEDGMENTS

I would like to thank to Ricardo Alberto López Silva and Antonio Famiglietti in constructing the experimental setup, writing the papers, fruitful conversations and being very good company during the warm daytimes of Madrid. As well as the technical crew of the department has assisted at hard times. Without the support and guidance of my co-advisor Antonio Lecuona Neumann the research would have never been completed. And of course, thank you to my ex-advisor Dr. Cemil Yamalı for widening my vision with his mind blowing aspect of philosophy of thermodynamics and humane personality, finally my advisor Prof. Dr. İlker Tari for accepting being the volunteer for me completing my work. Gracias a todos.

This work is supported by The Scientific and Technological Research Council of Turkey (TÜBİTAK) with the program number 2214/A. The funding of the research project “Tecnologías energéticas térmico-solares y de aprovechamiento de calores residuales a baja y media temperatura integradas en la red eléctrica”, ENE2013-45015-R from the Spanish Ministerio de Economía y Competitividad is greatly appreciated.

## TABLE OF CONTENTS

ABSTRACT . . . . .	v
ÖZ . . . . .	vi
ACKNOWLEDGMENTS . . . . .	ix
TABLE OF CONTENTS . . . . .	x
LIST OF TABLES . . . . .	xiii
LIST OF FIGURES . . . . .	xiv
LIST OF ABBREVIATIONS . . . . .	xviii
CHAPTERS	
1 INTRODUCTION . . . . .	1
1.1 Motivation and Problem Definition . . . . .	1
1.2 Passive House . . . . .	3
1.3 LEED . . . . .	4
1.4 BREEAM . . . . .	5
1.5 Refrigeration . . . . .	5
1.6 Absorption . . . . .	8
1.7 Absorption Cycle Solutions . . . . .	14
1.8 Absorption Cycles . . . . .	23
1.9 Desorber . . . . .	23

1.10	Absorber . . . . .	25
1.11	Pump . . . . .	27
1.12	Heat Exchanger . . . . .	28
1.13	Absorption cycle configurations . . . . .	30
1.14	Absorption solar cooling . . . . .	36
1.15	Proposed Methods and Models . . . . .	39
1.16	Contributions and Novelties . . . . .	40
2	SIMULATIONS . . . . .	41
2.1	Fluid mechanics in the tube . . . . .	41
2.2	Finite difference analysis of absorber tube . . . . .	46
2.3	Simulation of the cycle . . . . .	52
2.3.1	Mass Balance of the Absorption cycle . . . . .	54
2.3.2	Energy Balance of the Absorption Cycle . . . . .	55
2.4	Simulation of PTC Area . . . . .	58
3	EXPERIMENTS . . . . .	63
3.1	Experimental Uncertainty Analysis . . . . .	69
3.2	Evaluation of experimental data . . . . .	71
4	RESULTS AND DISCUSSION . . . . .	79
4.1	Simulations of Finite Difference Method . . . . .	79
4.1.1	Effect of tube tilting and liquid mass flow rate . . . . .	80
4.1.2	Effect of operative temperatures . . . . .	82
4.1.3	Effect of solar radiation and collector aperture . . . . .	85
4.2	Thermodynamics simulations of the cycle . . . . .	87

4.3	Thermodynamic simulation of a representative building . . . . .	92
4.4	Experimental results of the proposed generator/seperator . . . . .	96
5	CONCLUSION . . . . .	101
	REFERENCES . . . . .	105
APPENDICES		
A	TECHNICAL DRAWINGS . . . . .	115



## LIST OF TABLES

### TABLES

Table 1.1	Standards of energy efficient buildings . . . . .	2
Table 1.2	Passive House Standards . . . . .	4
Table 1.3	Commonly used soluiton pairs . . . . .	15
Table 2.1	Friction factor formulations . . . . .	45
Table 2.2	First law of thermodynamics for the components . . . . .	56
Table 2.3	First law of thermodynamics for the components (Continued) . . . . .	57
Table 2.4	Minimum and maximum cooling loads . . . . .	60
Table 2.5	Minimum and maximum temperature . . . . .	60
Table 3.1	The collected data . . . . .	66
Table 3.2	Uncertainty table of Pressure . . . . .	69
Table 3.3	Uncertainty . . . . .	71
Table 4.1	Reference case inputs and intermediate results . . . . .	80
Table 4.2	Standard climate values of the representative days . . . . .	87
Table 4.3	Average COP, cooling power and total cooling energy . . . . .	89
Table 4.4	Summary of the comparison . . . . .	96

## LIST OF FIGURES

### FIGURES

Figure 1.1	Vapor compression cycle . . . . .	6
Figure 1.2	Air cycle . . . . .	7
Figure 1.3	Thermoelectric Cooling . . . . .	8
Figure 1.4	Single effect absorption cycle . . . . .	9
Figure 1.5	Single effect absorption cycle with heat exchanger . . . . .	10
Figure 1.6	Combining heat pump and power cycle . . . . .	11
Figure 1.7	Heat pump and temperature amplifier . . . . .	12
Figure 1.8	Heat transfer directions at type I absorption cycle . . . . .	14
Figure 1.9	Variation of specific volume with respect to mass fraction of $HN_3$ . . . . .	20
Figure 1.10	Variation of enthalpy with respect to mass fraction of $NH_3$ . . . . .	22
Figure 1.11	Desorber . . . . .	24
Figure 1.12	Differential unit of desorber . . . . .	25
Figure 1.13	Absorber . . . . .	26
Figure 1.14	Half effect cycle . . . . .	32
Figure 1.15	Double effect series flow cycle . . . . .	33
Figure 1.16	Double effect reverse flow cycle . . . . .	34
Figure 1.17	Triple effect series flow cycle . . . . .	35

Figure 1.18	Triple effect parallel flow cycle . . . . .	36
Figure 1.19	Single effect absorption-compression cascade refrigeration system	37
Figure 1.20	Connection of solar collectors to absorption cycle . . . . .	38
Figure 1.21	Single effect absorption cycle with parabolic trough collector . .	39
Figure 2.1	Free body diagram of the open channel flow . . . . .	42
Figure 2.2	Fluid flow inside the tube . . . . .	42
Figure 2.3	Crossection of the tube . . . . .	43
Figure 2.4	Variation of $\phi$ . . . . .	45
Figure 2.5	Finite difference diagram of the open channel flow . . . . .	47
Figure 2.6	Finite difference diagram of the cross section . . . . .	48
Figure 2.7	Critical temperatures of solution . . . . .	53
Figure 2.8	Energy balance of the tube . . . . .	54
Figure 2.9	Cooling load of the cycle . . . . .	60
Figure 2.10	Ambient temperature . . . . .	61
Figure 3.1	Experimental Setup . . . . .	64
Figure 3.2	Temperature along the tube . . . . .	67
Figure 3.3	Pressure along the tube . . . . .	67
Figure 3.4	Mass flow rate . . . . .	68
Figure 3.5	Tank Level, Valve Opening, Heater Level . . . . .	68
Figure 3.6	Effectiveness of PTC . . . . .	72
Figure 3.7	Collector effectiveness versus the length of the subcooled zone .	73

Figure 3.8	The effect of the length of the subcooled zone on the refrigerant separation . . . . .	74
Figure 3.9	Pressure difference versus refrigerant mass flow rate . . . . .	75
Figure 3.10	Saturation temperature versus refrigerant mass flow rate . . . . .	76
Figure 3.11	Pressure difference versus saturation temperature . . . . .	76
Figure 3.12	Inlet mass flow rate versus pressure difference . . . . .	77
Figure 3.13	Received energy versus pressure difference . . . . .	77
Figure 4.1	Effect of liquid mass flow rate on vapor ammonia generation mass flow rate and efficiencies . . . . .	81
Figure 4.2	Pressure and Inlet liquid temperature . . . . .	83
Figure 4.3	Change of mass fraction with condenser temperature . . . . .	83
Figure 4.4	Change of mass flow rate of ammonia vapor with temperature . . . . .	84
Figure 4.5	Change of vapor efficiencies with temperature . . . . .	84
Figure 4.6	Joint effect of solar radiation and collector aperture on ammonia vapor generation percentage . . . . .	86
Figure 4.7	Joint effect of solar radiation and collector aperture on ammonia efficiencies . . . . .	86
Figure 4.8	Daily solar power of the representative days . . . . .	87
Figure 4.9	Time evolution of refrigeration along the representative days of each month . . . . .	88
Figure 4.10	Time evolution of cooling power along the representative days of each month . . . . .	89
Figure 4.11	Time evolution of subcooled zone length along the representative days of each month . . . . .	91

Figure 4.12	Required PTC area . . . . .	92
Figure 4.13	Variation of COP during daytime . . . . .	93
Figure 4.14	Variation of Effectiveness during daytime . . . . .	94
Figure 4.15	Desorption rate comparison with experiment . . . . .	99
Figure 4.16	Variation of subcooled zone with irradiance . . . . .	99
Figure 4.17	Variation of Effectiveness with irradiance . . . . .	100
Figure A.1	Parabolic Trough Collector . . . . .	116
Figure A.2	Condenser . . . . .	117
Figure A.3	Evaporator . . . . .	118
Figure A.4	Flowmeter . . . . .	119
Figure A.5	Heat Exchanger . . . . .	120
Figure A.6	Pressure Sensor . . . . .	121
Figure A.7	Pump . . . . .	122
Figure A.8	Performance Curve of the Pump . . . . .	123
Figure A.9	Technical Drawing of the Pump . . . . .	124
Figure A.10	Accuracy of the Pump . . . . .	125
Figure A.11	Measure of the Tank level . . . . .	126
Figure A.12	Accuracy of the Tank Level . . . . .	127

## LIST OF ABBREVIATIONS

### ABBREVIATIONS

$\epsilon$	Effectiveness
$\eta$	Efficiency
$\nu$	Chemical potential
$\Psi$	Specific Helmholtz free energy
	Double flow angle
$\rho$	Density
$\tau$	Shear stress
$\theta$	Inclination angle
$A$	Area
$c_p$	Specific heat
$COP$	Coeffient of performance
$D$	Diameter
$f$	Friction factor
$g$	Specific Gibbs free energy
$g$	Accelaration of gravity
$G$	Solar radiation
$h$	Specific enthaply
$H$	Enthalpy
$I$	Irradiation
$k$	Friction factor
$l$	Length
$m$	Mass

$N$	Mol
$Nu$	Nusselt Number
$p$	Pressure
$Pr$	Prandlt Number
$Q$	Heat Energy
$q$	Specific heat
$Re$	Reynolds Number
$s$	Specific enthropy
$S$	Peripheral length
$T$	Temperature
$u$	Specific internal energy
$U$	Overall heat transfer coefficient
$v$	Specific volume
$V$	Volume
$w$	Specific work
$x$	Quality
$y$	Mass ratio of a solution





## **CHAPTER 1**

### **INTRODUCTION**

#### **1.1 Motivation and Problem Definition**

The financial instabilities and collapses lead the industries to seek for distinctive solutions. An apparent attempt of the research of alternatives is observed after the oil crises in 1970's. The sudden increase of the oil price triggered people to look for alternatives of oil to satisfy the energy demands of the industry. This was not only for securing the current situation at that time but also for preventing the possible future casualties from oil crises.

The solution has two branches. First one is reducing the consumption of energy and the second is replacing oil with some other kinds of energy resources. Hence, countries are in a pursuit of consuming less and being less dependent on oil. The annual energy consumption of buildings is 40% of the total world energy consumption. An extensive portion of this consumption is due to the heating and cooling demand [1] [2].

As a result of the fact, in the 1970's the researchers began investigating to reduce the heating and cooling demand of houses as well as replacing oil with alternative sources [3]. Reducing the heating and cooling demand requires better insulation and smart architectural designs whereas replacing oil with alternatives could be either not burning it for heating purposes and also not using the electricity generated in fuel oil power plants.

Researchers and engineers aimed to work on such ecological building designs. However, economically, the primary attempts resulted in failure. The cost of the reduction

of heat demand increased hyperbolically. The costs were not compensated by fuel saving even though supported with renewable energy sources [3]. Not only the cost but also the ventilation arose as a problem. Due to the airtight windows and the building envelopes the air exchange has diminished so did the indoor air quality. The carbon dioxide amount and humidity increased and mould formations were observed. It became necessary to install mechanical air ventilation systems which brought extra cost. These attempts were reported from Europe [3] and China [4] so now it is not surprising that those researchers have come up with smart solutions to these problems.

Since then the costs have been decreasing and energy efficient houses that are supported by renewable energy sources are becoming feasible. Also USA joined the field and took a considerable part of the research with hosting 47 out of 91 worldwide projects in 2014 [5]. Participation of many countries, in other words, the presence of people from different climates resulted in creation of standardization of such houses with different norms. Some of the standards [6] are tabulated in Table 1.1 .

Table 1.1: Standards of energy efficient buildings

Standard	Country
Passive House	Germany
LEED	USA
BREEAM	UK

These standards have been created to ensure that the consumption of the buildings can be tracked and rated. Even though the standrads vary in detail, they all serve for the same purpose. They are forcing engineers to utilize renewable energy sources such as solar energy. On the other hand, they do not define how to use it but they observe the results. For an example of refrigeration one may choose generating electricity to run refrigerators or another may use thermodynamic cycles to refrigerate. The choice is up to the designers. At the end it is important to know what their standards are in order to decide which technology is to be choosen. A breif explanation of the standards are mentioned in the following sections.

## 1.2 Passive House

Passive House concept was first developed in Germany Darmstadt in 1991 with an idea of consuming very few or zero energy if possible. There were three main design considerations: the local climate conditions, passive design methods to reduce the heating and cooling loads and finally the efficient mechanical and renewable energy systems [7].

First of all, researchers aimed to reduce the energy consumption of a house using passive strategies like insulation, high-quality windows, airtightness, ventilation heat recovery, and the avoidance of thermal bridges. Besides, they are supported with renewable energy technologies [8]. That brand new innovation was able to use less than 10% of the heating energy of a recently-built German house. An overall evaluation of the proceeding research in many years showed that passive houses use 80%-90% less heating energy in return, 5%-10% increase in the cost. The key role in that success is the significantly simplified mechanical systems due to the introduction of high efficient building envelope. The envelope is engineered to minimize all heat flows at and within the building. While doing so, it may benefit solar energy if available. In that case the house is given another name, passive solar house [5].

It is calculated that if photovoltaic panels were used it is possible to compensate the high initial cost of the passive house in nine years [6]. However, the system should be supported with an earth-air heat exchanger and domestic solar water heater. It can also be supported by wind power [7] as well as biomass, geothermal and many others that are available.

The Passive house standards [9] are summarized in the Table 1.2. The standards introduce limitations to heating and cooling loads and air leakage. Also sets higher limits for the demand of renewable energy sources and lower limit for generation. According to the renewable energy demand and generation. The standards define the building under three categories; Classic, Plus and Premium. Note that the table is not strict in each criterion and sometimes open ended due to the fact that the values tend to vary according to local climate and desired thermal comfort. For a detailed investigation the official documentation of Passive House Standards must be consulted

[9].

Table 1.2: Passive House Standards

Criteria	Limit		
Heating Demand	$\leq 15kWh/(m^2a)$		
Heating Load	$\leq 10W/m^2$		
Cooling + dehumidification demand	$\leq 15 + \text{dehumidification contribution, } kWh/(m^2a)$		
Cooling load	$\leq 10W/m^2$		
Press. test result $n_{50}$	$\leq 0.6l/h$		
	Classic	Plus	Premium
Renewable primary energy demand	$\leq 60kWh/(m^2a)$	$\leq 45kWh/(m^2a)$	$\leq 30kWh/(m^2a)$
Renewable energy generation		$\geq 60kWh/(m^2a)$	$\geq 120kWh/(m^2a)$

Many researchers are trying to achieve these standards in their designs with their numerical calculations with commercial software, self-developed programs and even with Artificial intelligence [10]. On the other hand, many experiments and applications are ongoing. The founder of Passive House Institute, Dr. Feist, reported more than 100 dwelling units in five European countries [3]. Recently there are 4880 passive houses constructed worldwide [11] and it is increasing.

### 1.3 LEED

Leadership in Energy and Environmental Design (LEED) is a green building rating system that aims to implement innovative design to buildings [12, 13]. It was founded by US Green Building Council (USGBC) for the US Department of Energy in 1998 [14]. The building with LEED rating are expected to improve their sustainability, reduce the energy consumption, moderate the water usage, sustain good indoor conditions, protect the construction site and use sustainable materials [13]. The rating criteria vary on the type of the building and even neighbourhoods and cities can be rated by LEED [15].

## **1.4 BREEAM**

Building Research Establishment Environmental Assessment Method (BREEAM) is first established in 1990 and continued to improve its criterion [16]. Recently it is recognized as an international scheme [17]. BREEAM provides independent third party certification of the assessment of the sustainability performance of individual buildings, communities and infrastructure projects [18]. It has standards in five applications: communities, infrastructure, new construction, In-use and refurbishment and fit-out. There are many more certification standards worldwide with different rating systems. The reason is that the evaluation depends on the geography, the climate, the economy and the culture. Many countries develop their own rating systems and some of them go further to be globally recognized rating systems. However, all of them aim to reduce the consumption of energy and fit into the nature while sustaining human comfort.

The monitoring and controlling the energy consumption of buildings are verified by those standards. In order to fit into the standards new methods must be developed. The fact that the majority of the energy is consumed by refrigeration units, it is a good place to start. The refrigeration supposed to be maintained passively as much as possible. However this is not the case all the time especially when lower temperatures are needed as required in food preservation and human comfort. The thesis is planned to clarify the methods that are used for refrigeration (or cooling) and draw a detailed theoretical picture of absorption as a refrigeration tool. After giving the fundamental theory of the method, the study of the absorption cycle using finite difference and thermodynamics simulations is explained. The simulations are performed to understand the behaviour of cycle that are comparatively harder to investigate experimentally. Lately, the simulations are compared with the experimental data.

## **1.5 Refrigeration**

Vapor compression cycle is known to be the most common refrigeration cycle. The working principle is, at a first sight, the reverse of a heat engine, or more in detail, an inverse Rankine cycle. The cycle is depicted in Figure 1.1. It requires work to pump

heat from a low temperature area to a high temperature area. The refrigerant gas is compressed in the compression unit to a high pressure and driven to a condensation chamber where it is able to reject its heat to the environment by the use of a heat exchanger. As a result, the high pressure condensed liquid is formed and is passed through an expansion valve. The expanded liquid is accumulated in the evaporation chamber where it immediately changes its phase to gas and extracts heat from the surrounding. As a result, the heat is collected from the environment of the evaporation chamber and cooling effect is created. The recently formed gas proceeds to the compressor to complete the cycle.

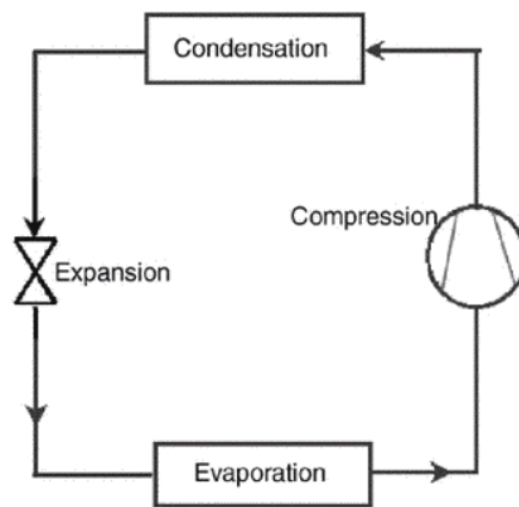


Figure 1.1: Vapor compression cycle

On the other hand, it is not the only way to construct a refrigeration cycle. Air cycle refrigeration works in a reverse Brayton or Joule cycle with no phase change. Figure 1.2 demonstrates the cycle that the air is compressed to a high pressure and heat is rejected at that pressure. It is expanded through an expander and is reaching a lower temperature. Finally, in the cooling chamber heat is collected from the environment to create the refrigeration effect. The air can be used as an open system to cool down a space and as closed systems with the help of heat exchangers. The main application of such a refrigeration cycle is aircrafts [19].

Total loss refrigerants are used for refrigeration purposes. Volatile fluids in the form of liquid, that  $CO_2$  and  $N_2$  are most known ones, are released in the atmosphere to

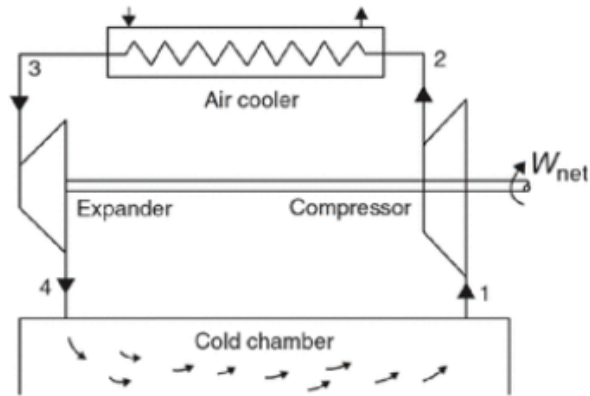


Figure 1.2: Air cycle

change phase from liquid to gas. During phase change they extract heat from their surroundings [19]. Since both of the gases naturally exist in the atmosphere it is considered a non-hazardous process. Even water ice can be considered as a total loss refrigerant.

Thermoelectric cooling, in other words, Peltier effect, is used for very limited purposes. The working principle is that the electrical current running through two dissimilar metals causes a temperature drop and rise at different junction points as shown in Figure 1.3.

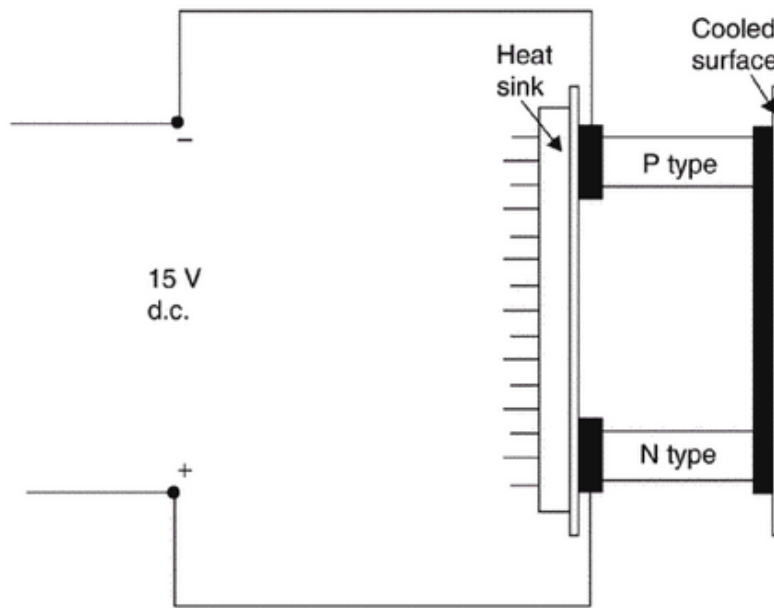


Figure 1.3: Thermoelectric Cooling

The recent improvements of semiconductors made this method used more efficiently yet needs more improvement [19].

Finally, some certain magnetic materials are observed to change their temperature upon exposure to alteration in the magnetic field. This is the so-called magnetocaloric effect. Magnetic refrigeration has been applicable to work on very low ambient temperatures. This is a field open to research nowadays.

## 1.6 Absorption

There are other methods that use heat as an input instead of work such as the Stirling cycle, desiccant cooling, adsorption cycle and absorption cycle. Among those, the most promising methods are adsorption and absorption cycles. Adsorption is the process of a solid which undergoes a chemical or physical interaction with a liquid or gas refrigerant and its surface is covered with the refrigerant. On the other hand, absorption is the physical phenomenon that a liquid captures another liquid or gas into its own volume. Adsorption is a surface phenomenon whereas absorption is volumetric



yet both processes are thermal. They require heat to separate the components; they release heat while combining. That property is used to pump the heat in thermodynamic cycles. The practice between adsorption and absorption is that the first one requires even lower grade energy and has longer cycle time which makes it harder to implement in industrial applications. On the other hand, absorption has relatively higher performance and power output.

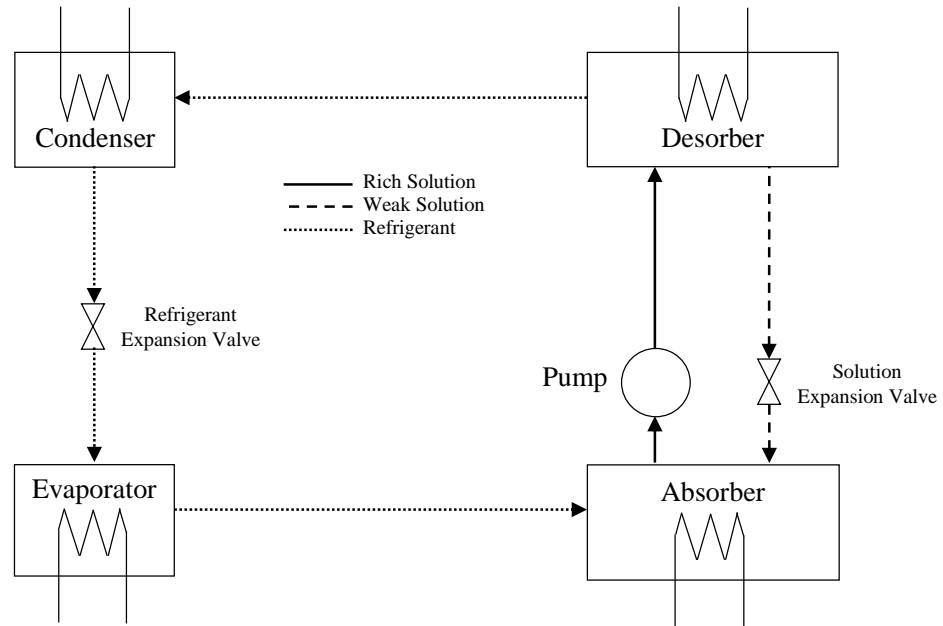


Figure 1.4: Single effect absorption cycle

The cycle of absorption shown in Figure 1.4 requires a cooler and a heater to interact and separate the refrigerant from the solution. The chamber where they interact is called absorber and the one where they separate is called desorber (generator). The components form a solution in the chambers. In order to circulate the solution, this is required to construct a cycle, two reservoirs are connected with pipelines. A pump is connected to one of the pipelines to run the solution and the other one has an expansion valve in order to maintain the desorber at higher pressure than the absorber. The high pressure in the desorber is used to push the separated gas through another pipeline. The gas is an overheated refrigerant and it can be used in an inverse Rankine refrigeration cycle. The gas is diverted through a refrigeration-like loop, which consists of a condenser, expansion valve and evaporator. The cooling effect is obtained

in the evaporator chamber and the gas separates from the saturated liquid. The vapor returns to the absorber to be pumped again to the desorber after being absorbed by the solution. A schematic drawing of the cycle is shown in Figure 1.4. The solution that runs through the pump has more refrigerant and is called a rich solution, whereas the pipeline which has the solution expansion valve contains less refrigerant and is called a weak solution. The difference of the mass between the two yields the amount of gas that circulates through the condenser, refrigerant expansion valve and evaporator.

It is a common practice to use a heat exchanger between the rich solution and the weak solution. It increases the efficiency of the cycle a considerable amount. The reboost cycle with solution heat exchanger is represented in the Figure 1.5.

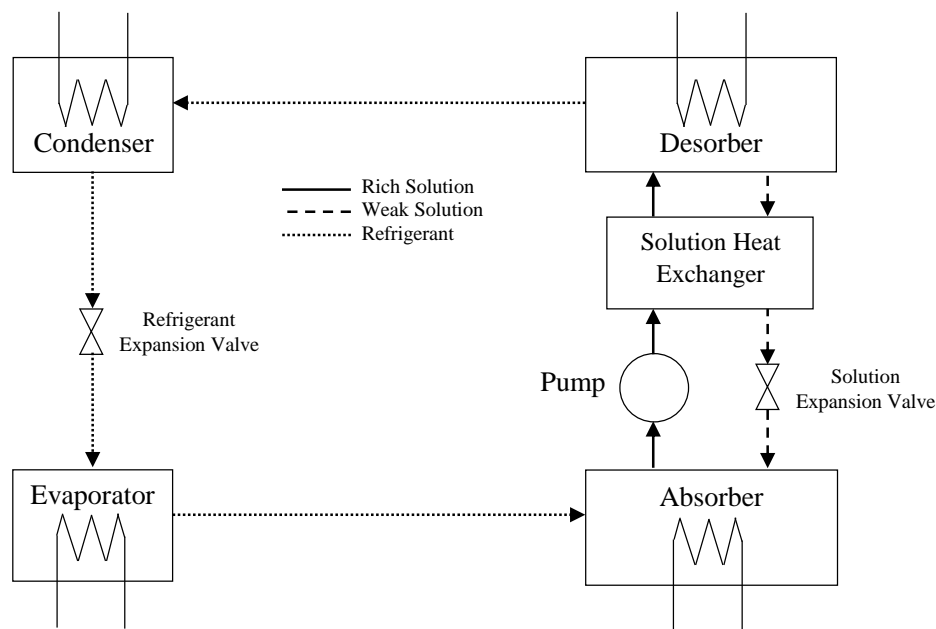


Figure 1.5: Single effect absorption cycle with heat exchanger

The heat input to the cycle is from the desorber and evaporator where the absorber and condenser are to reject heat to the surrounding. The cycle looks like a classical inverse Rankine refrigeration cycle where the mechanical compression unit, which is called compressor, is replaced by a chemical compression unit. In Figure 1.5, the units all together on the right hand side mimics a compressor in a refrigerator cycle. On the other hand, the cycle looks like a combination of two cycles: refrigeration and

a power cycle. Figure 1.6 demonstrates a refrigeration cycle on the left and a power cycle on the right. The idea, basically, is to convert the input heat energy to kinetic energy using the power cycle and just after that, using the kinetic energy to pump the heat from low temperature area to a high temperature area. This can be done using a turbine and a compressor. However, The work created by the power cycle can be passed directly to the refrigeration cycle without generating kinetic energy as depicted in Figure 1.6. It is assumed that the amount of work produced is equal to the amount of work required by the other cycle. As a result, the turbine and the compressor units in the Figure 1.6 drop out and the remaining two half cycles come together to form a new complete cycle. The boiler corresponds to the desorber and the condenser in the power cycle represents the absorber in the absorption cycle.

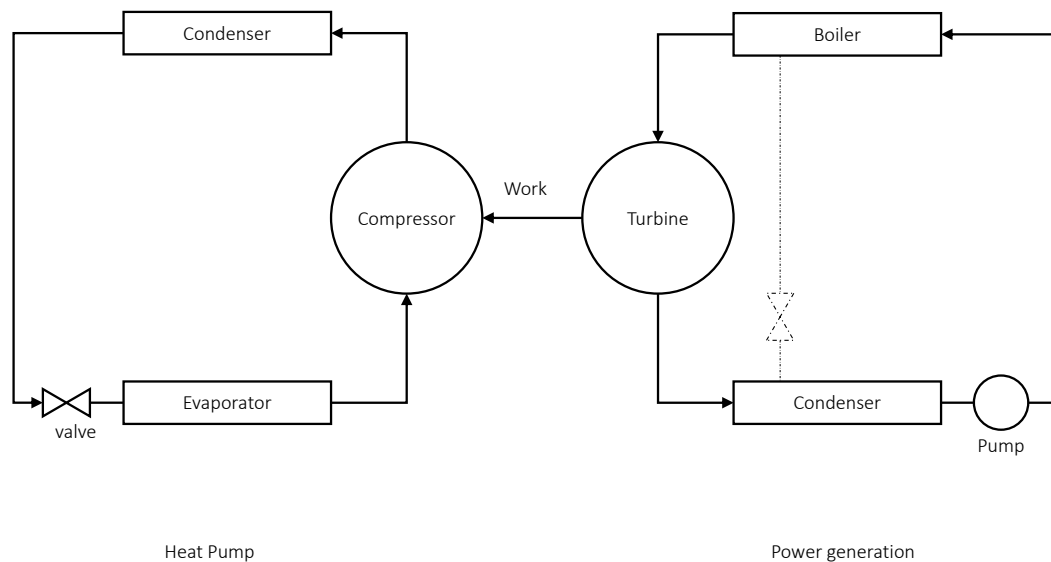


Figure 1.6: Combining heat pump and power cycle

The heat exchange with the environment occurs at three different ambient temperatures. The desorber is at a high temperature, the evaporator is at a low temperature, and finally the condenser and absorber are at medium temperature environments. There are two types of absorption cycles. The classification is done according to the directions of the heat. In both cases the direction of high and low temperature heat is in the inverse direction of medium temperature heat. Conservation of energy holds

for both of the conditions.

$$Q_H + Q_L - Q_M = 0 \quad (1.1)$$

and

$$-Q_H - Q_L + Q_M = 0 \quad (1.2)$$

The only difference is the direction of the heat. Positive sign can be considered as into the system and negative is out of the system. For the case that the direction of the high and low temperature heat are to the system is called type I (heat pump). If the medium temperature heat is into the system it is called type II (temperature amplifier). Type I cycle with single medium temperature and type II with double medium temperatures are demonstrated in Figure 1.7.

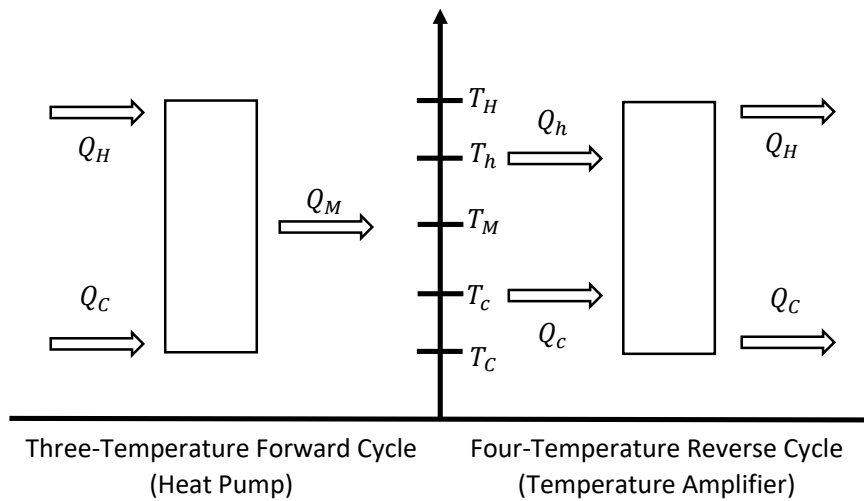


Figure 1.7: Heat pump and temperature amplifier

The performance of a Carnot cycle for heat pumping is calculated as the ratio of the benefit obtained and the net work required. Using a similar analogy, the performance

of type I and type II cycles can be obtained. The performance of Type I for heating application and refrigeration application are

$$COP_H = Q_M/Q_H \quad (1.3)$$

$$COP_R = Q_L/Q_H \quad (1.4)$$

and type II is

$$COP_{TA} = Q_H/Q_M \quad (1.5)$$

where COP stands for Coefficient Of Performance, H heating, R refrigeration and TA is for temperature amplifier. Applying the first and second laws of thermodynamics one may obtain the COP values in terms of temperatures [20].

$$COP_H = T_M(T_H - T_L)/T_H(T_M - T_L) \quad (1.6)$$

$$COP_R = T_L(T_H - T_M)/T_H(T_M - T_L) \quad (1.7)$$

$$COP_{TA} = T_H(T_M - T_L)/T_M(T_H - T_L) \quad (1.8)$$

The cycle has two different components for transferring medium temperature heat. In some cases those components may have different temperatures. Such a case is called a four temperature cycle. The COP of such a case can be calculated by the entropic mean heat rejection temperature [21].

$$T_M = \frac{Q_h + Q_c}{(Q_h/T_h) + (Q_c/T_c)} \quad (1.9)$$

where  $Q_h$  and  $Q_c$  are warmer and colder mid temperature heat;  $T_h$  and  $T_c$  are the warmer and colder mid temperatures. The Figure 1.8 demonstrates the type I absorption cycle where high and low temperature heat is into the system with single medium temperature.

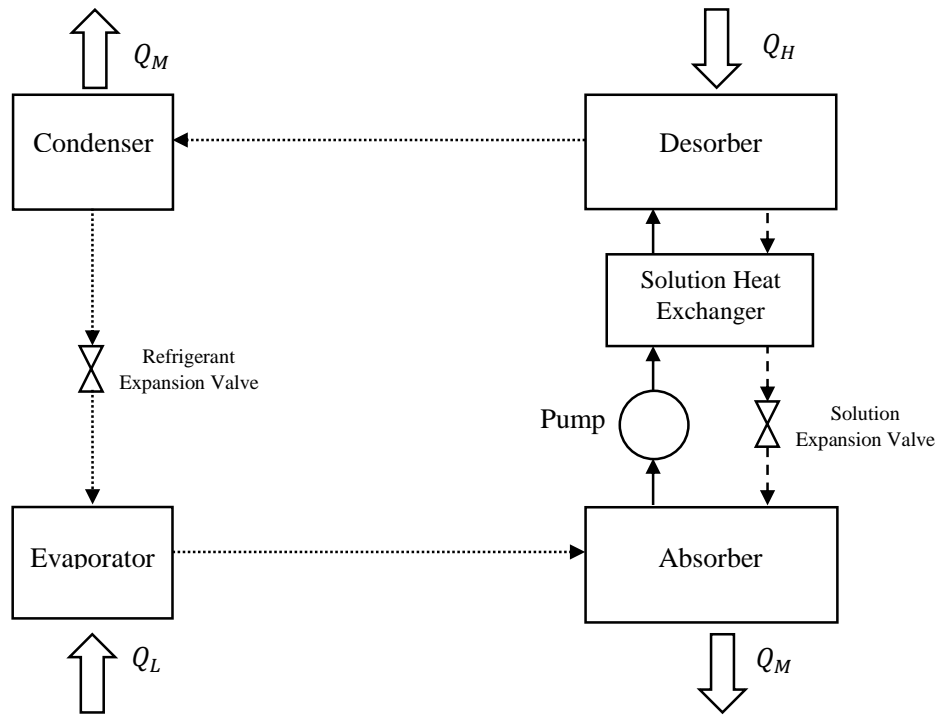


Figure 1.8: Heat transfer directions at type I absorption cycle

## 1.7 Absorption Cycle Solutions

Even though the performance and the efficiency of the reversible cycles depend on the temperatures only, real machines strongly depend on the properties of working fluids. There are several types of solutions as working fluids that are implemented in the absorption cycles. The performance of the cycle is highly dependent on the thermodynamic properties of the solution pair [22], yet none of them has the best performance, rather they must be chosen according to the needs of the design. Among many others, one may consider, for example, choosing a pair to work with higher temperatures or another pair for being more environmentally friendly. There is no fluid pair superior to the others and dominating, rather each pair introduced in the literature has some weak points while meeting the deficit of others. The common point is that the solution pairs should be chemically stable in the range of working conditions. For instance, they shouldn't solidify or form crystals. Such a case may obstacle the pipeline, stop the cycle and may break the machine. Also, it is better if they are non-toxic, non-explosive, non-corrosive and finally cheap enough. Some of

them are able to work on low pressures. That would decrease the cost of the system by avoiding thick-walled equipment, high cost of pumping and big expensive vacuum equipment [23]. For better performances, the difference in the boiling temperature of the solution and the refrigerant fluid (relative volatility) must be as large as possible. In other words, it is crucial to obtain as pure refrigerant as possible at the evaporator chamber. Otherwise, cost and heat requirements would increase. Also, the heat of vaporization is supposed to be high as possible because it is important to carry more heat per unit mass flow rate. Apart from those, the properties of heat transfer phenomenon such as viscosity, surface tension, diffusivity and heat transfer coefficients are supposed to be in consideration [24]. Macriss, R.A. (1998) reviewed over 500 articles related to the properties of absorbents. He has reported 38 different refrigerants, as well as 131 single, 42 binary, and 14 ternary absorbent compounds. He has categorized the compounds such as inorganic and organic. Jian Sun has categorized [25] the compound in a more detailed way as  $NH_3$  series,  $H_2O$  series, alcohol series, halogenated hydrocarbon series and other refrigerants. It is possible to add auxiliary inert gases like helium into the solution. Such a modification decreases the partial pressure of the refrigerant according to Dalton's law to create a better cooling effect in the evaporator [26]. Some of the commonly used compounds Jian Sun et. al. (2012) are tabulated in the Table 1.3 [25].

Table 1.3: Commonly used solution pairs

Solvent-refrigerant	Cooling point	Remarks
$H_2O - NH_3$	$-77^\circ C$	Stable for a wide range of operating temperature and pressure. High latent heat. Thermophysical properties are well studied.
$LiNO_3 - NH_3$	$-77^\circ C$	Crystallization problems do not occur. No need to use a rectifier. Low absorption temperatures are sufficient.
$LiBr - H_2O$	$0^\circ C$	High latent heat. High temperature difference of boiling points. Thermophysical properties are well studied.

One of the widely used solutions is  $H_2O - NH_3$ . The  $H_2O$  is the solvent and  $NH_3$  is the refrigerant. Theoretically, an absorption machine with that solution can cool down to  $-77^\circ\text{C}$  as it is the evaporation temperature of the refrigerant. The solution has a wide temperature range to work with a penalty of higher pressure values. On the other hand, the absorption machine suffers from not generating pure refrigerant in the desorber process. Due to the volatility of water, the ammonia usually contains some amount of water vapor. Water vapor decreases the performance of the machine when condenses and accumulates in the evaporator [27]. In order to diminish the disadvantage, a rectifier unit is placed in the cycle. Rectifiers are used to create a refrigerant with a better quality yet the extra unit to the system comes up with more expense, complexity and weight. On the other hand, ammonia needs to be handled with care. According to ASHRAE [28] it is not permitted to use indoor applications. Ammonia solutions exist in the environment naturally, nevertheless pure ammonia is a risk to health.

Using  $H_2O$  as refrigerant is environmentally friendly, non hazardous, and cheap yet obtaining a solution with  $LiBr$  as absorbent is corrosiveness to steel, has lower availability, and is relatively expensive [29]. The latent heat of  $H_2O$  is higher compared to its alternatives like  $NH_3$ . The pressure variation in the cycle can be considered to be lower. As the solidification temperature of water is  $0^\circ\text{C}$ , theoretically this solution cannot cool down below this temperature. But the major problem comes with the crystallization phenomena. It is basically the formation of solid  $LiBr$  particles in the solution under the working conditions of the absorption machine. One of the ways to avoid the issue is to arrange the solution mass ratio (the ratio of the mass of refrigerant to the mass of the total solution), mass flow rate, pressure and temperature of the machine at appropriate values with the return of narrower working conditions [30]. Researchers are seeking different methods to overcome the issue by combining the solution with some anti-crystallization additives.

The solution pair  $NH_3$  as refrigerant and  $LiNO_3$  as an absorbent performs relatively better in lower temperature inputs [29]. The minimum temperature exceeds to the evaporation point of  $NH_3$  which is suitable for many engineering applications. It does not require any rectification process due to  $LiNO_3$ 's high evaporation temperature neither suffers from crystallization. Yet, as mentioned earlier,  $NH_3$  is supposed to be



handled with care and should not be placed indoor.

The thermodynamic properties of a fluid pair is determined by their individual properties and using the first and second law analysis. The change of internal energy of a system is defined as

$$du = q - w \quad (1.10)$$

If it is assumed to be mechanically reversible and it is only due to the variation of the volume, the work is defined as

$$dw = pdv \quad (1.11)$$

The sign convention is that the heat into the system is chosen to be positive and the work done by the system is accepted to be positive. Considering a reversible heat transfer process, the definition of change of entropy can be written as

$$ds = dq/T \quad (1.12)$$

and finally combining the equations results a fundamental state variables relation

$$du = Tds - pdv$$

Similarly, enthalpy, Gibbs free energy and Helmholtz free energy can be written as [31]

$$dh = Tds - vdp \quad (1.13)$$

$$dg = vdp - sdT \quad (1.14)$$

$$d\Psi = -pdv - sdT \quad (1.15)$$

The equations 1.13 - 1.15 assume a quasi-equilibrium state and give simple relations for the unknown property with the data of alternating properties for closed systems. Those equations apply to multi-phase systems and mixtures beside single phase pure

fluids as long as it is assumed to be in equilibrium and the properties are accepted to be averaged properties for the whole system under consideration.

The functional representation of the variables above would result in the Maxwell's relations [32]

$$g = g(T, p) \quad (1.16)$$

taking the differential

$$dg = (g/T)p dT + (g/p)T dp \quad (1.17)$$

combination of the recent equation and the previously defined gibbs free energy results in the formulation of specific volume and entropy

$$v = (g/p)T \quad (1.18)$$

$$s = -(g/T)p \quad (1.19)$$

Differentiating both equations results in the Maxwell's relations

$$(v/T)p = (s/p)T \quad (1.20)$$

Similar derivation can be done to the other formulations and in total twelve relations can be derived for pure substances. On the other hand, mixtures have another variable that represents the changes in the composition of the system. The change might be chemical as well as physical. The derivation from now on will proceed by assuming the composition variation may occur, in other words, mass transfer within the system and to the surrounding is possible. Let's define the composition variable as mass fraction of a binary mixture.

$$y_1 = m_1/(m_1 + m_2) \quad (1.21)$$

$$y_2 = m_2/(m_1 + m_2) \quad (1.22)$$

$$y_1 + y_2 = 1 \quad (1.23)$$

where  $y_1$  and  $y_2$  are the mass fractions of a binary mixture. Gibbs free energy is a function of mass fraction as well,

$$g = g(T, p, y) \quad (1.24)$$

where  $y$  is mass fraction of either component of the mixture. The differential of Gibbs free energy can be written by taking the derivative of the equation above

$$dg = (g/T)_{p,y}dT + (g/p)_{T,y}dp + (g/y)_{T,p}dy \quad (1.25)$$

The first two derivatives on the right hand side of the equation are the same as defined earlier yet under constant mass fraction condition. One can insert the previously derived relations into this one and get

$$dg = -sdT + vdp + (g/y)_{T,p}dy \quad (1.26)$$

The third derivative is related to the chemical potential,  $\mu$ , of the components in a mixture.

$$\mu_1 = (G/N_1)_{T,p,N_2} \quad (1.27)$$

$$\mu_2 = (G/N_2)_{T,p,N_1} \quad (1.28)$$

The chemical potential of the component of a binary mixture can be written as [33]

$$\mu_1 = g + (1 - y_1)(g/y_1)_{T,p} \quad (1.29)$$

$$\mu_2 = g - y_1(g/y_1)_{T,p} \quad (1.30)$$

and the relation between the chemical potential and the mixture properties is derived as

$$dg = -sdT + vdp + (\mu_1 - \mu_2)dy_1 \quad (1.31)$$

The subtraction of the chemical potentials in the last term of the equation represents the energy variation associated with the changes in the composition. The chemical potential itself is a measure of the contribution to the Gibbs free energy associated with that component. Similarly, internal energy, enthalpy and Helmholtz free energy, can be written as a function of the chemical potential. It is an important variable in mixture thermodynamics and should be considered as the same way thermal potential (temperature) and mechanical potential (pressure). It does not only refer to chemical reactions but also physical interactions like mixing and separation as is the case in absorption and desorption respectively. Note that the chemical potential of a pure

substance is exactly the Gibbs free energy as can be proved by inserting  $y_1 = 1$  in the above relations.

Ideal mixtures demonstrate a behaviour such that upon mixing, the volume of the mixture is equal to the summation of the volumes of the components independently. This is the case when the molecular interaction among different components are negligible as in the case of air at low pressures. However, most of the liquids do not present such a behavior. The resulting volume of the mixture is more complicated to calculate. Figure 1.9 shows the specific volume change of the binary solution of  $NH_3 - LiNO_3$  with respect to the amount of  $NH_3$  on a mass basis at temperature of  $20^\circ C$ . The solid line is the measured data of Infante Ferreira [34] and the dashed line is a straight line starting from pure  $LiNO_3$  to pure  $NH_3$  that represents the alteration of the specific volume if the solution were an ideal mixture. The concave up curve reveals that the mixture shrinks down to a lower volume upon mixing. The dotted line represents the tangent line at  $y = 0.5$ .

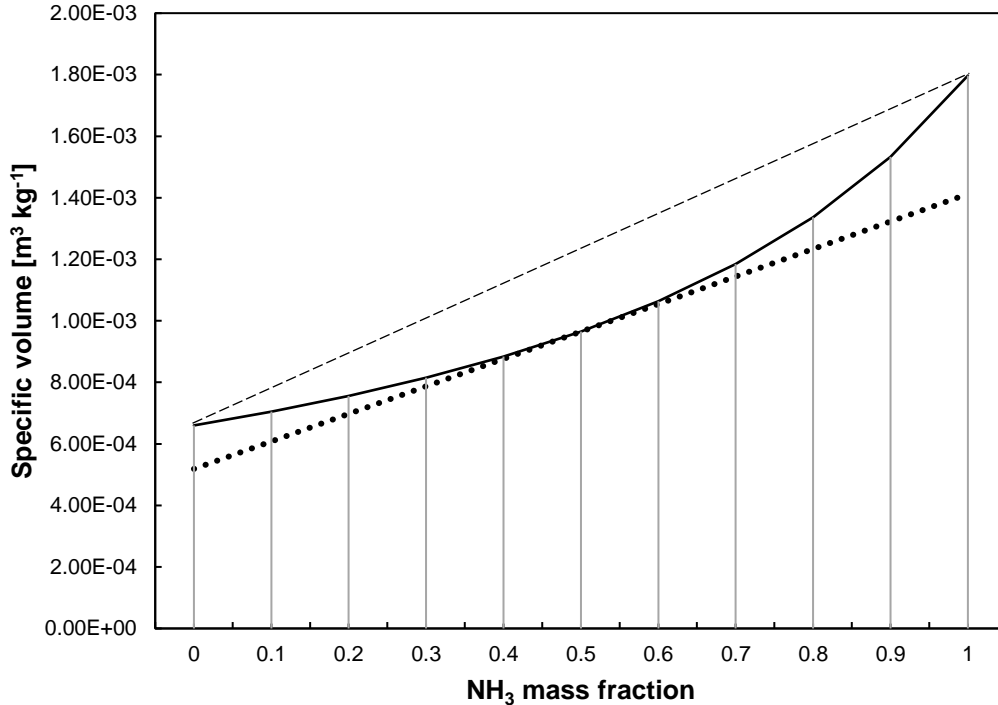


Figure 1.9: Variation of specific volume with respect to mass fraction of  $NH_3$

The partial molal volume of the mixture can be formulated as

$$v = (V/N_i)_{T,p,N_j} \quad (1.32)$$

$$v_1 = v + (1 - y_1)(v/y_1)_{T,p} \quad (1.33)$$

$$v_2 = v - y_1(v/y_1)_{T,p} \quad (1.34)$$

Let's determine the values on the plot. As an example, the mixture specific volume at  $y = 0.5$  and  $T = 20$  is  $9.65 \times 10^{-4} m^3/kg$ . Note that the volumes of the pure components are at the points of  $y = 0.0$  and  $y = 1.0$  of the solid curve and are  $6.60 \times 10^{-4} m^3/kg$  and  $1.80 \times 10^{-3} m^3/kg$  respectively. The values at the edges of the tangent line (dotted line) are the partial mass volumes and are  $5.19 \times 10^{-4} m^3/kg$  and  $1.41 \times 10^{-3} m^3/kg$ . Now, let's evaluate the formulas as

$$v/y_1 = (v(0.5001) - v(0.4999))/(0.5001 - 0.4999)$$

$$v/y_1 = 8.94 \times 10^{-4}$$

$$v(0.5) = 9.65 \times 10^{-4}$$

$$v_1 = 9.65 \times 10^{-4} + (1 - 0.5)(8.94 \times 10^{-4}) = 1.41 \times 10^{-3}$$

$$v_2 = 9.65 \times 10^{-4} - 0.5(8.94 \times 10^{-4}) = 5.19 \times 10^{-4}$$

where the results match. A similar evaluation can be done for the internal energy and enthalpy. When two or more miscible species are mixed the mixture enthalpy would not be equal to the mass average of the enthalpy of the independent components unless the mixture is ideal. The enthalpy versus mass fraction of  $NH_3$  at  $20^\circ C$  is plotted in Figure 1.10.

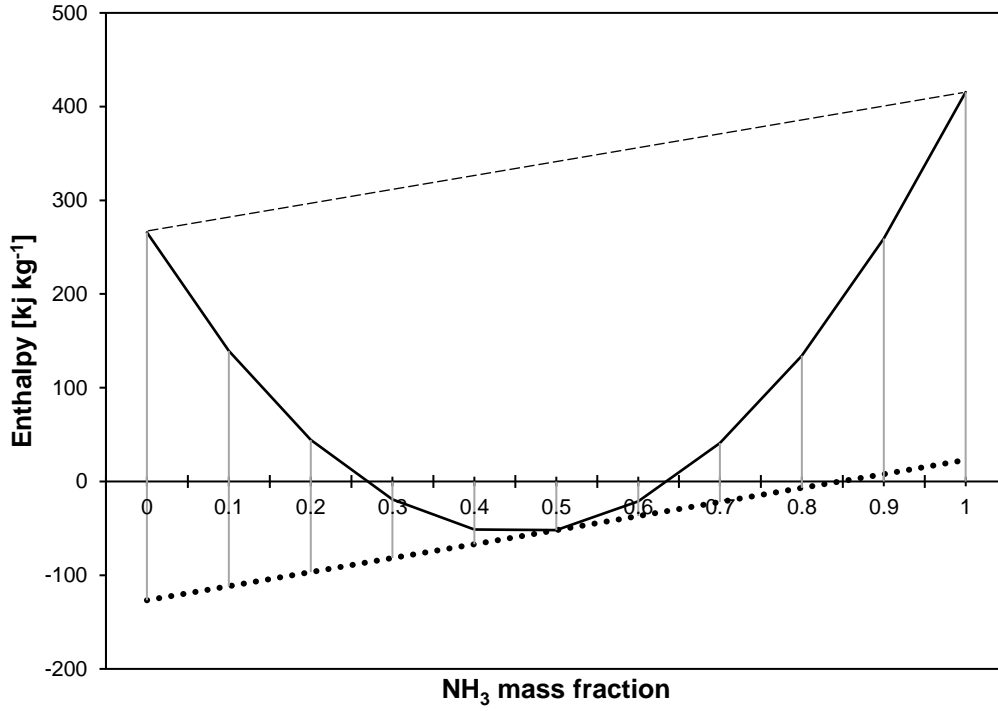


Figure 1.10: Variation of enthalpy with respect to mass fraction of  $NH_3$

The enthalpy variation in terms of partial molal enthalpy is

$$h = (H/N_i)_{T,p,N_j} \quad (1.35)$$

the partial enthalpies of the species in the mixture are

$$h_1 = h + (1 - y_1)(h/y_1)_{T,p} \quad (1.36)$$

$$h_2 = h - y_1(h/y_1)_{T,p} \quad (1.37)$$

The tangent line in the plot is evaluated at  $y = 0.5$ . At that point the enthalpy of the mixture is  $-51.89 \text{ kJ/kg}$  where the partial mass enthalpies of the species (dotted line) are  $-126.73 \text{ kJ/kg}$  and  $22.95 \text{ kJ/kg}$ . The enthalpies of the pure species can be read from the dashed line and are  $265.77 \text{ kJ/kg}$  and  $415.45 \text{ kJ/kg}$ . The mixing enthalpy can be calculated as

$$h_{mix} = (-51.89) - (265.77 + 415.45)/2$$

$$h_{mix} = -392.5 \text{ kJ/kg}$$

The negative mixing enthalpy reveals that the mixing process of  $NH_3$  and  $LiNO_3$ , so called absorption, is exothermic. Note also that the mixing enthalpy can be calculated as

$$h = y_1 h_1 + (1 - y_1) h_2 \quad (1.38)$$

This is why the tangent curve is a line. Same analysis can be done for the specific heat as well. The definition of the specific heat is

$$c_p = (h/T)_{p,y} \quad (1.39)$$

and

$$c_p = y_1 (h_1/T)_{p,y_1} + (1 - y_1) (h_2/T)_{p,y_1} \quad (1.40)$$

$$c_p = y_1 c_{p,1} + (1 - y_1) c_{p,2} \quad (1.41)$$

## 1.8 Absorption Cycles

Absorption cycles have five components at their minimum configuration. Those are desorber, absorber, pump, heat exchangers and valves. The heat exchangers are the solution heat exchanger, condensor and evaporator; where as there are two valves. One is for weak solution and another is for refrigerant. Depending on how complex the cycle is configured the number of any component may increase. Detailed explanations of those components and different cycle configurations are mentioned on the next sections.

## 1.9 Desorber

Another aspect of absorption machines is the phase equilibrium. The equilibrium between phases takes place when thermal, mechanical and chemical equilibrium of each component are satisfied. In other words, the phases would have the same temperature, same pressure and no net mass flow among phases should be observed. On the other hand, in absorption/desorption processes, the composition of the phases are usually different. In the case of  $NH_3 - LiNO_3$  the liquid is the solution where the vapor is

only  $NH_3$ . The vaporization of  $NH_3$  can occur under different conditions such as constant temperature or constant pressure. During the vaporization, the ratio of  $NH_3$  in the solution decreases where the vapor has always a ratio of unity. This implies complication due to the fact that the properties of the solution strongly depend on the concentration of the species. Considering the desorber unit in the cycle as one input with rich solution, and two exits are for weak solution and  $NH_3$  vapor separately. So, there is a liquid entering and leaving with a difference of vapor that is ducted out as demonstrated in Figure 1.11.

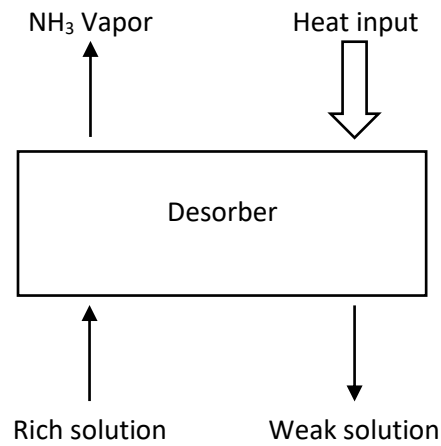


Figure 1.11: Desorber

The differential drawing of the control volume is shown in the Figure 1.12.

The mass and the energy balance of  $NH_3$  is

$$dm/m = dx/(y - y_v) \quad (1.42)$$

$$dQ = mdh + (h_v - h)dm \quad (1.43)$$



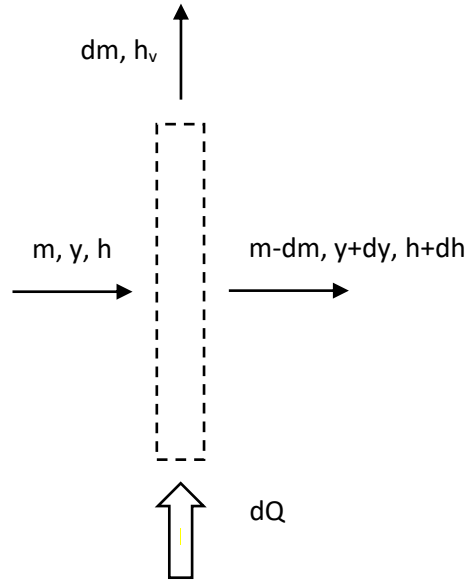


Figure 1.12: Differential unit of desorber

combining these two equations results in

$$q = h_v - h - (y_v - y)(h/y)p \quad (1.44)$$

where the derivation is done for constant pressure case.

### 1.10 Absorber

The overall mass balance of the absorber is

$$\dot{m}_1 = \dot{m}_2 + \dot{m}_3 \quad (1.45)$$

and mass balance of either of the components is

$$y_1 \dot{m}_1 = y_2 \dot{m}_2 + y_3 \dot{m}_3 \quad (1.46)$$

dividing the last equation by the vapor mass flow rate results in circulation ratio  $f$ ,

$$f y_1 - (f - 1) y_3 = y_2 \quad (1.47)$$

where  $f$  is the ratio of the mass flow rates

$$f = \dot{m}_1 / \dot{m}_2 \quad (1.48)$$

and the heat equation takes the form of

$$q = h_2 - h_3 + f(h_3 - h_1) \quad (1.49)$$

The final representation of the conservation of heat is crucial in order to understand how the heat is shared in the system. The term  $h_2 - h_3$  represents the heat contributed to the temperature increase of the liquid whereas  $f(h_3 - h_1)$  is the contribution to the phase change.

The absorption process, on the other hand, is similar to a condensation process where a phase change occurs but with a significant difference that the condensed component is not pure anymore. A control volume presentation of absorber is at Figure 1.13.

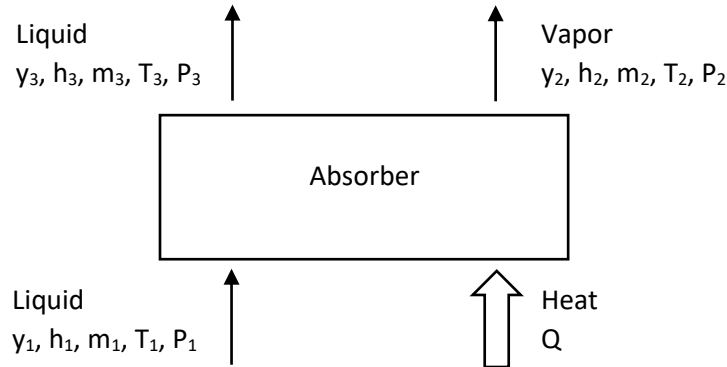


Figure 1.13: Absorber

The mass and energy conservation equation are identical in desorber and absorber and hence one may write the energy conservation equation of an absorber as following

$$q = h_2 - h_1 + f(h_1 - h_3) \quad (1.50)$$

where  $q$  represents the heat (per unit mass of vapor absorbed) released from the system.  $h_2 - h_1$  term is related to the phase change and the second term evaluates the cooling of the liquid. In the calculations of absorber and the desorber, the inlet and the exit liquid states are assumed to be saturated and the vapor is assumed to have the same pressure with the liquids. Note that the vapor phase can be superheated or saturated as well depending on the working conditions. In some cases like  $H_2O - NH_3$  mixtures, it may not be pure.

The condenser and evaporator are regular heat exchangers. They don't exchange mass flows. The condenser is to reject some heat from the vapor (type I) and bring the flow to the condensed state. The evaporator is to change the phase from condensed liquid to saturated vapor with the transferred heat from the environment. The states of the vapor at the boundaries of these two units may vary depending on the working conditions and the design of the machine.

### 1.11 Pump

In order to circulate the liquid solution between absorber and desorber a pump is needed. At the same time the pump creates two zones of different pressure. The ideal pumping process of the liquid introduces two assumptions. First one is that the liquid is incompressible and the other one is that the process is isentropic. When these two conditions meet the temperature variation is also negligible. So it is also accepted to be isothermal. Finally, in real non-ideal circumstances, the work done by the pump can be evaluated by the formula below

$$w = \dot{m}v(p_h - p_l)/\eta \quad (1.51)$$

where  $w$  is the work done,  $(p_h - p_l)$  is the pressure different after and before the pump,  $v$  is the specific volume of the liquid,  $m$  is the mass flow rate and  $\eta$  is the isentropic efficiency of the pump.

## 1.12 Heat Exchanger

The solution heat exchanger and the other heat exchangers, like condenser, work in a similar manner different than absorber and desorber which are allowing mass flows to mix. When mass transfer is not the case, the control volume is easier to evaluate. Without going into the details of a heat exchanger one can model it using the UA model. The overall heat transfer coefficient of the heat exchanger is shown as  $U$  and the heat exchanger area as  $A$ . The multiplication of  $U$  and  $A$  is used with the log mean temperature difference as follows

$$Q = UA\Delta T_{lm} \quad (1.52)$$

$$\Delta T_{lm} = \frac{(T_{h1} - T_{c1}) - (T_{h2} - T_{c2})}{\ln((T_{h1} - T_{c1})/(T_{h2} - T_{c2}))} \quad (1.53)$$

The  $UA$  type comes with two problems. First one is that the  $U$  is not independent of temperature. It varies with the temperature. But taking this dependency into account is a tough problem to deal with. Even though the reality is more complex, it is a common practice to accept the error introduced by the assumption of  $U$  being independent from temperature for the sake of converging a solution in the calculations. On the other hand, the problem with the UA-type formulation is that the logarithmic term is not always possible to calculate as the argument has tendency of being negative or null. In the case of iterative solution some singularities may occur and the program may not converge. One may prefer using a close approximation curve to the actual logarithmic curve.

One approximation that is derived during the thesis work is as the following.

Define  $\Delta T_1 = T_{h1} - T_{c1}$  and  $\Delta T_2 = T_{h2} - T_{c2}$

$$\ln(\Delta T_1/\Delta T_2) = \ln((1+x)/(1-x)) \quad (1.54)$$

where  $x = (\Delta T_1 - \Delta T_2)/(\Delta T_1 + \Delta T_2)$  and  $x \in [0, 1)$ ,  $x \ll 1$

$$f(x) = \ln((1+x)/(1-x)) \quad (1.55)$$

$$f(x) = \ln(1+x) - \ln(1-x) \quad (1.56)$$

$$f'(x) = 1/(1+x) - 1/(1-x) \quad (1.57)$$

where the two terms on the right hand side can be written as infinite sums as

$$1/(1 \pm x) = 1 \pm \sum_{i=1}^{\infty} (-x)^i \quad (1.58)$$

The evaluation of the infinite sum results as following

$$1/(1 \pm x) = 2 \quad (1.59)$$

hence the derivative becomes

$$f'(x) = 2 \quad (1.60)$$

Integrate both sides of the equation

$$f(x) = 2x + C \quad (1.61)$$

where  $C = 0$  for  $f(0)$

$$f(x) = 2x \quad (1.62)$$

$$\ln((1+x)/(1-x)) = 2x \quad (1.63)$$

finally, the linear assumption of the logarithmic term is

$$\ln(\Delta T_1/\Delta T_2) = 2(\Delta T_1 - \Delta T_2)/(\Delta T_1 + \Delta T_2) \quad (1.64)$$

As long as the condition defined for  $x$  is satisfied, the linear assumption fits very well to the logarithmic curve. However, the conditions match for evaporator only in an absorption cycle but not for the other heat exchangers. For the rest of the heat exchangers a polynomial curve fit can be used. Even though it is not as simple as the previously introduced approximation yet still it is more handy than the logarithmic equation to converge.

$$\ln(\Delta T_1/\Delta T_2) = (\Delta T_1 \Delta T_2 (\Delta T_1 + \Delta T_2)/2)^{1/3} \quad (1.65)$$

Beside among the dozens of binary solutions there are multi component solutions which make the class of the mixtures even larger and open to research. In the current

research  $LiNO_3 - NH_3$  is studied. The most important part is the safety of the compound.  $NH_3$  is known as to be used in explosives and forming part of bath salts, and  $NH_3$  is considered to be risky to human health. However, there is an ongoing debate about its harmful effects on the environment.

### 1.13 Absorption cycle configurations

Crystallization is a common problem in some of the solid solvent-refrigerant pairs. The working conditions of the cycle could be close to the crystallization line of the solution. When the refrigerant/solution rate is low and/or the working temperature is low enough, the solution may start to crystallize. As a result the amount of the solvent diminishes and the machine efficiency decreases. In addition, it may block the pipeline and cause physical damage as well. The crystallization is observed between the solution expansion valve and the absorber, yet it might be seen elsewhere [35]. Once the salt forms in the pipeline it is time consuming to eliminate it. With the solution of  $LiNO_3 - NH_3$  the crystallization does not come as a big problem in the running conditions of an absorption machine. On the other side, it is not needed to use a rectifier. A rectifier is a component that is commonly used in machines with  $H_2O - NH_3$  pairs. It is due to the non-negligible vapour pressure of water compared to the vapour pressure of ammonia in the desorber process. In order to obtain a good quality of refrigerant (free of water), a rectifier is a must to implement to the cycle. If not implemented, water penetrates to evaporator and prevents evaporator to minimize its temperature, hence the performance and efficiency are affected negatively [36]. Beside not suffering from salt formation and not requiring a rectifier,  $LiNO_3 - NH_3$  pair can work with lower grade energy. That makes it suitable for working with waste heat and solar energy. In the current work, solar energy implementation of the absorption machine is studied. The defined absorption cycle is a single effect type I absorption cycle. There are other types with more complicated layouts, and of course, with varying pros and cons. L.A.Domínguez-Inzunza (2014) has developed mathematical models of different types of absorption machines that work with  $LiNO_3 - NH_3$  pair [37]:

#### 1. Single-effect

2. Half-effect
3. Double-effect series
4. Double-effect reverse
5. Triple-effect

He has calculated that the lowest cooling temperature can be achieved by half-effect absorption cycle but has a low coefficient of performance. The single-effect absorption cycle has the simplest design and COP is as high as double of the half-effect, yet in return requires higher desorber temperatures. Double-effect absorption cycles reach higher COP but need even higher desorber temperatures such as  $140^{\circ}\text{C}$  to reach an evaporator temperature around  $-5^{\circ}\text{C}$ . The highest COP is obtained from triple-effect absorption cycles, yet very high desorber temperatures are required. On the other hand, their design is even more complicated and bulky. Berhane (2010) have studied Single-effect, Half-effect, Double-effect series, Double-effect reverse, Double-effect parallel, Triple-effect series and Triple-effect parallel cycles with  $\text{LiBr} - \text{H}_2\text{O}$  [38]. They have calculated the maximum COP's and found out that it increases respectively. The half-effect absorption cycles are like single effect cycles but with an additional circuit of solution. So, they have two so called thermal pumps connected in series if considered as a refrigeration cycle. The heat input is from both of the generators. The rest of the cycle is similar to a single effect as they both have one condenser and one evaporator. A schematic drawing of the half-effect cycle is demonstrated in Figure 1.14. The figure is placed on a temperature versus pressure coordinate system to visualize how the pressure and temperature alter in the cycle.

The coordinate system is placed on the visuals of the rest of the cycles as well. See the double effect series cycles in the Figure 1.15. It has an extra condenser, generator and solution heat exchanger compared to a single effect cycle.

This type is called series due to the fact that the generators are connected in a serial manner. The hot solution at point 14 is leaving the high pressure generator and enters into the medium pressure condenser-generator. The heat is supplied to the high pressure generator only.

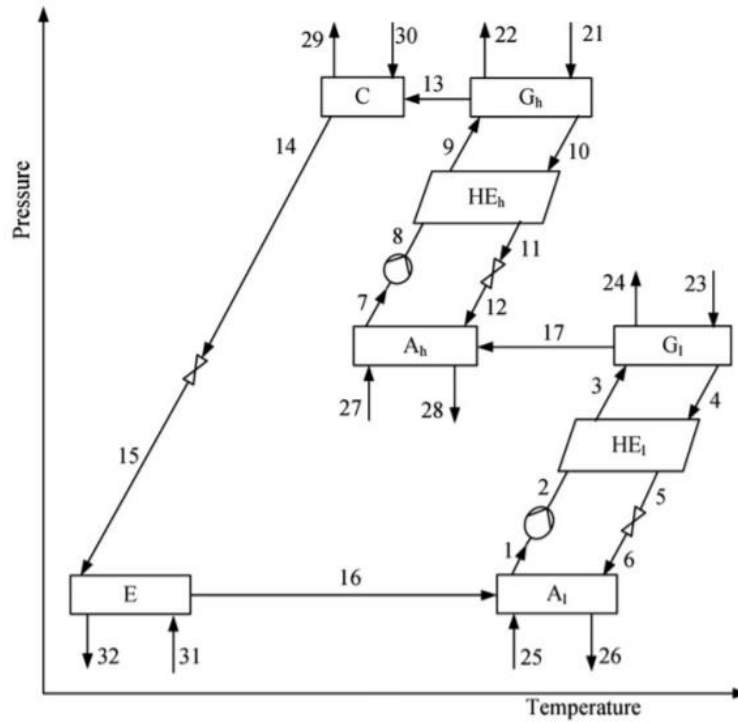


Figure 1.14: Half effect cycle

The double-effect inverse cycle has an extra pump than double-effect serial and has one solution expansion valve less as seen in Figure 1.16.

Unlike to serial, in the reverse cycle the rich solution is pumped to the condenser-generator rather than the generator. The weak solution returns directly to the absorber after passing through two heat exchangers. The rest is the same as the serial cycle. Note that double effect cycles are supposed to have higher temperature in the generator in order to perform better than single and half effect cycles.

The triple effect series cycle has a similar configuration to the double effect series cycle but with an additional generator, condenser-generator and heat exchanger. A schematic drawing is shown in the Figure 1.17.

The heat is supplied to the generator only, and the heat recovered from the condenser-generator is also used to generate more refrigerant. Triple effect in parallel is constructed in the same manner as double effect parallel but with extra components of two condenser-generators, heat exchangers and solution expansion valves.



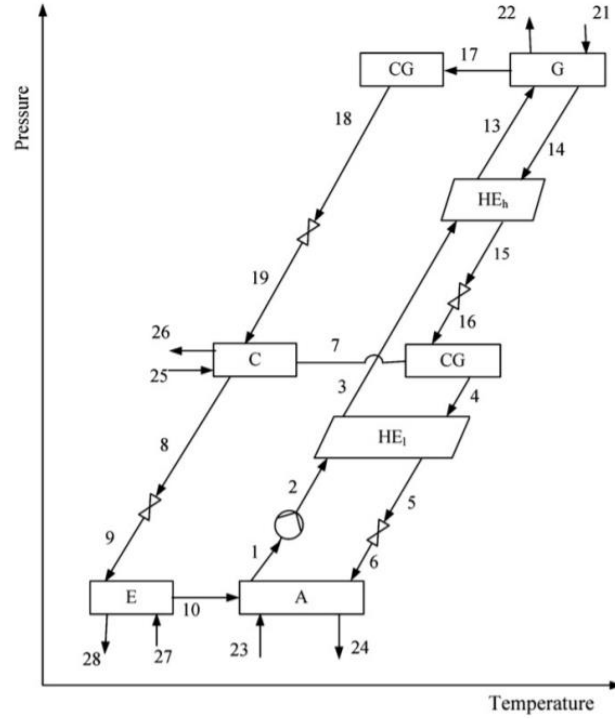


Figure 1.15: Double effect series flow cycle

The same methodology can be followed to construct multiple effect cycles, yet they are not very common due to their complexity.

L.A. Domínguez-Inzunza has simulated those cycles with  $NH_3 - LiNO_3$  and compared their working temperatures and COP values [37]. They have reported that the lowest evaporator temperatures with lowest generation temperature around  $50^\circ C$  can be obtained from the half-effect cycle but its COP is very low (0.3) compared to the other configurations. The single effect is the simplest one and requires the minimum number of units to construct. Its COP is usually twice (0.66) as half-effect cycle on the other side it works at higher generator temperatures. The highest COP is observed for double (1.12) and then triple (1.22) effect cycles respectively. In return they require higher minimum working temperatures as  $140^\circ C$  for double and  $150^\circ C$  for triple effect cycles. A similar work is performed by Berhane H. Gebreslassie [38] and R. Maryami[39] for  $H_2O - LiBr$  solution. Their results are not very different and follow the same patterns for COP values of the cycles. Jianzhao Wang et.al. [40] have pointed out that there is a gap between working temperatures of half-effect

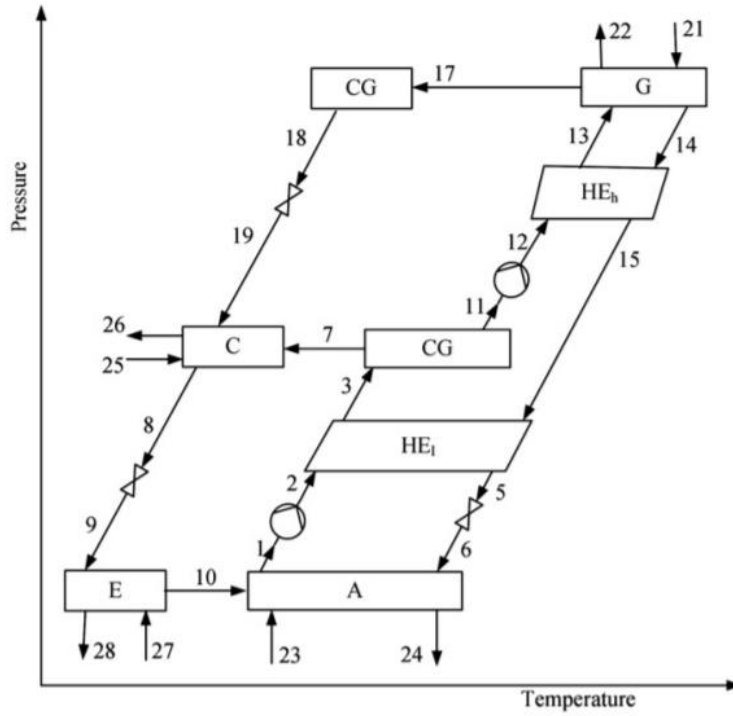


Figure 1.16: Double effect reverse flow cycle

and single effect cycles and could be fulfilled by a specially designed cycle so called 1.5 effect cycle. They have reported two new configurations of 1.5 effect cycle beside four already existing in the literature [41]. Their study based on the solution of  $H_2O - LiBr$ . Similarly, D.L. Hong et. al. suggested a different design for the gap between single effect cycle and double effect cycle [42]. They have suggested Evaporator-Absorber-Exchange (EAX) absorption refrigeration cycle. M. Medrano et. al. suggest double-lift cycle which are able to work low and medium temperatures (from  $70^\circ\text{C}$  to  $100^\circ\text{C}$ ) and their study is based on organic solution which are trifluoroethanol (TFE)-tetraethylenglycol diethyl ether (TEGDME or E181) and methanol-TEGDME and compared their performances with  $H_2O - NH_3$  solution. They have reported a minimum  $65^\circ\text{C}$  generator temperature and a maximum of 0.45 COP values for the combination of organic solutions and double-lift cycle configuration. On the other hand, Xiaona Yan et.al. have suggested a single effect/double lift configuration that is able to work larger temperature zones than single effect and double lift cycles [43]. Many researchers have suggested implementing an ejector to a single effect cycle [44, 45, 46, 47]. They have reported improvements of COP in single effect cycle

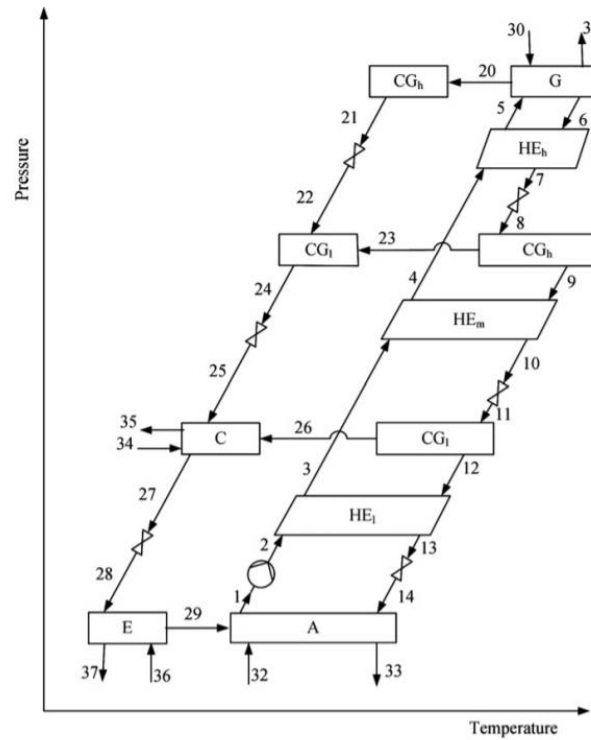


Figure 1.17: Triple effect series flow cycle

for higher generator temperatures. D. Colorado et.al. [48] and some other researchers [49, 50, 51, 52] mention about mixed configuration of a conventional vapor compression cycle and single effect absorption cycle. The idea is that the evaporator in the single effect cycle is connected to the condenser of vapor compression cycle as shown in Figure 1.19

This system is called a single effect absorption-compression cascade refrigeration system. They have recorded a decrease in the electricity consumption of the vapor compression refrigeration cycle. D. Colorado has introduced double effect absorption-compression cycle for the first time [48]. Yingjie Xu et. al. took it a bit further and achieved  $-170^{\circ}\text{C}$  with their cascade system using a solution of DMF-R32/R134a but on the other hand suffered from low COP's in the range of 0.101-0.172 [53]. Two other common configurations are regenerative absorption cycle [54] and variable effect absorption cycle [55, 56]. The types and working conditions of cycles are as large as number of solutions. Combination of those two parameters creates a huge cluster.

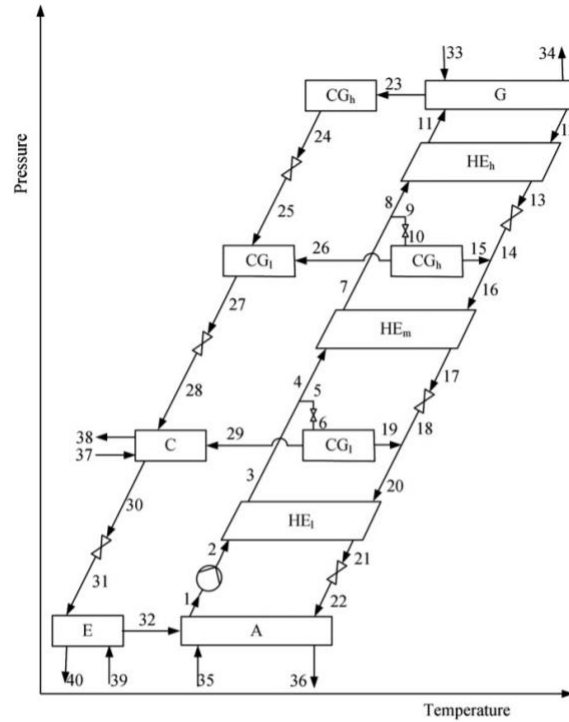


Figure 1.18: Triple effect parallel flow cycle

### 1.14 Absorption solar cooling

Absorption machines are able to operate with low grade energy. That can be the waste heat of a plant, solar energy [57, 58], geothermal energy [59]. A power plant that burns fossil fuels or runs with nuclear energy rejects huge amount of waste heat to the surrounding which is usually abandoned. Low grade energy is wasted in almost all the fields where a diesel engine runs like long distance ships and trucks as well. J. Koehler (1997) has designed, built and tested a single effect  $H_2O - NH_3$  absorption machine inside a truck to assist its refrigeration [60]. They are convinced that a long distance driving on flat roads gives promising results. Francisco Táboas (2014) compared several solution pairs in order to find out the one which best fits the fishing ship's cooling demand [61]. The machine used the waste heat of the exhaust gases. Moreover, solar irradiation is also abandoned in the nature as a low-grade heat source. Absorption machines are able to capture the energy from the sun and use it for refrigeration purposes. This method is called solar cooling using absorption. Not surprisingly, more cooling power is required when there is more irradiation. This

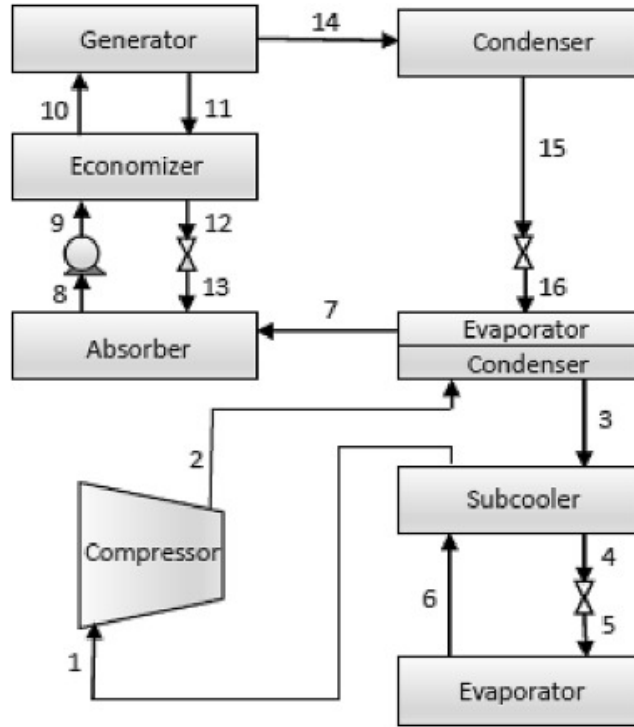


Figure 1.19: Single effect absorption-compression cascade refrigeration system

fact makes solar cooling an attractive idea. There can be several methods rather than absorption, however it is the one with a promising future of applications.

The schematic drawing of the single-effect absorption machine demonstrates the component of desorber which is basically a heat exchanger to grasp the energy in the form of heat. The desorber heat exchanger can be connected to concentrated solar panels among several types[62]; parabolic trough collector (PTC), linear Fresnel, solar tower and parabolic dish. On the other hand, non-concentrated solar panels such as evacuated tubes can be implemented for low temperature applications[63]. Using the solar panels, the heat transfer fluid (HTF) is heated. With the help of a pump the high temperature HTF is fed to the desorber heat exchanger. In some of the applications it is seen that there can also be heat storage tanks implemented. For the sake of simplicity the storage tank is not demonstrated in Figure 1.20.

In the current work, the novel improvement, in such a way that the desorber has been modified so that it works as a solar heat collection unit, is studied. It allows the radiation absorber tube to be used directly as a desorber. The heat transfer fluid,

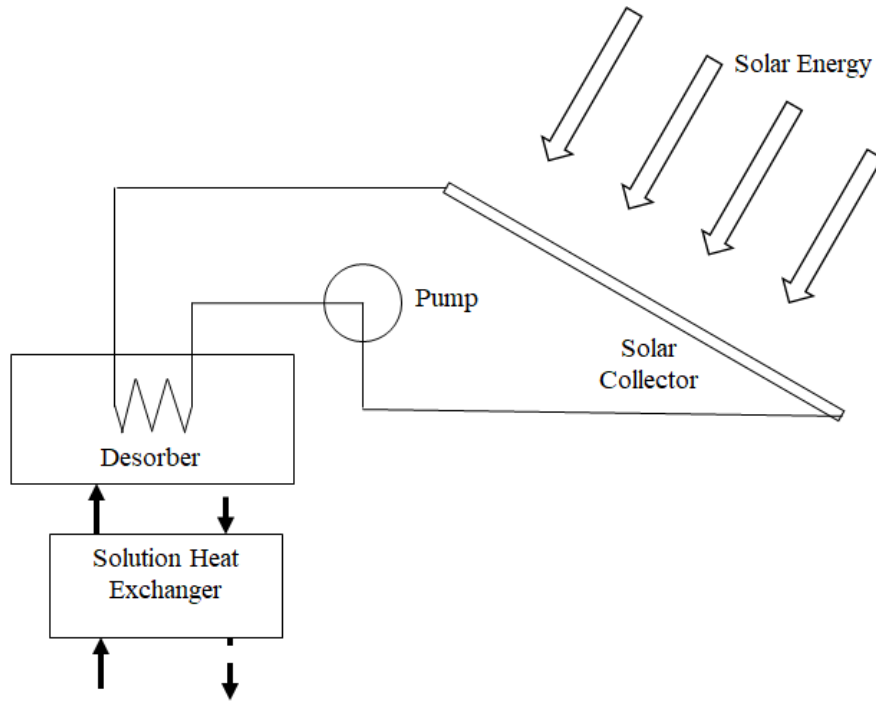


Figure 1.20: Connection of solar collectors to absorption cycle

some piping , pump and a heat exchanger has been eliminated. The configuration is represented in Figure 1.21.

The desorber is connected to the pipes 3, 4 and 7. The thin rectangular shape represents a radiation absorber tube of a parabolic trough collector. The modification simplifies the system, reduces the cost, weight and increases efficiency due to the elimination of an extra heat exchanger. However, the physics in the desorber tube is complicated. A rich solution enters the tube from the higher end to stream downwards due to gravity. The heat input along the tube extracts some of the refrigerant to leave to pipe 7 where the remaining solution exits to pipeline 4. It has a two phase, stratified, gravity driven, counter flow of a variable mass fraction of a less studied solution.

The upcoming chapters are studying the proposed novel system in numerical simulations and experiments.



## **1.16 Contributions and Novelties**

Even though it is a known method, it is novel to replace some certain components of the cycle with the solar panels. In other words, seeking a solution to reduce the weight and increase the efficiency of the cycle in order to assist a passive house to minimize their external energy purchase. The thesis is contributing a novel way of constructing the cycle, analyzing, comparing and contrasting with the conventional designs.



## CHAPTER 2

### SIMULATIONS

The suggested improvements of the absorption cycle need to be examined. First of all, simulations are performed. The simulation of the system is handled in several different aspects. After a brief introductory calculations of fluid mechanics of the absorber tube, the finite difference analysis is performed. Later, the thermodynamics equations of the whole cycle are solved simultaneously to examine characteristic behavior of the cycle. In the final simulation, the cycle is adapted to simulate a real-world example.

#### 2.1 Fluid mechanics in the tube

A flow where the flow has a free surface is called a water channel [66]. The fluid flow in the absorber tube is a open channel flow. The driving force is gravity due to the inclination  $\theta$  and it is assumed that the flow is not accelerating, and has a constant cross-section along the tube. The force balance is demonstrated in the Figure 2.1.

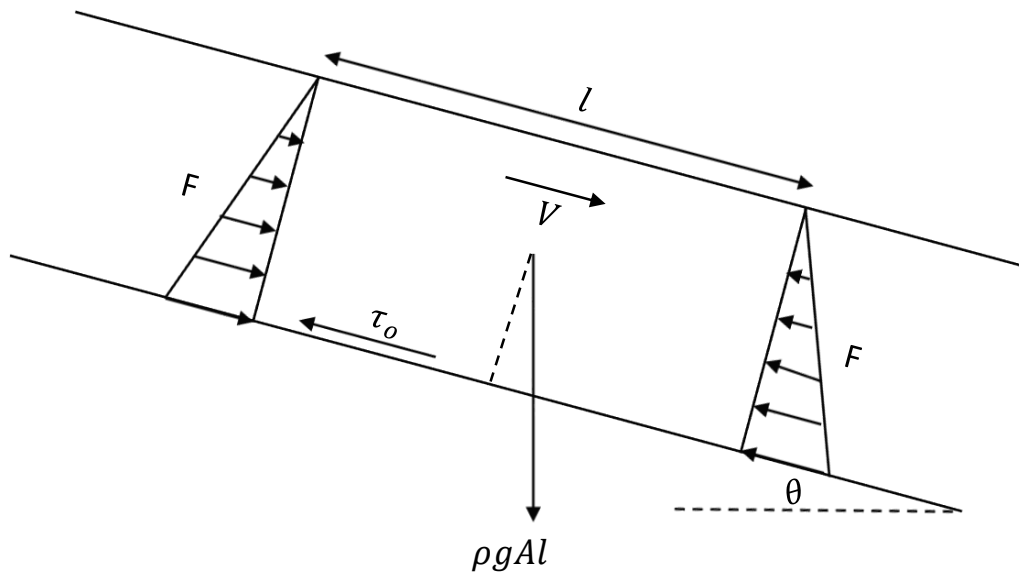


Figure 2.1: Free body diagram of the open channel flow

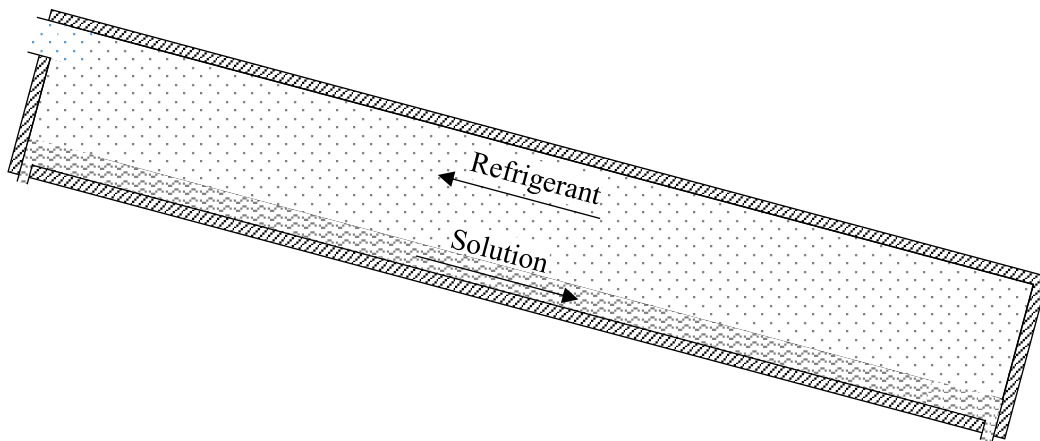


Figure 2.2: Fluid flow inside the tube

The forces of  $F$  are due to hydrostatic pressure of the fluid. With the assumption that the height of the fluid is not changing, the magnitude of the forces due to the hydrostatic pressure on the lateral sides are equal in magnitude. The other two forces are the shear force acting on the fluid due to the friction and the gravitational force.

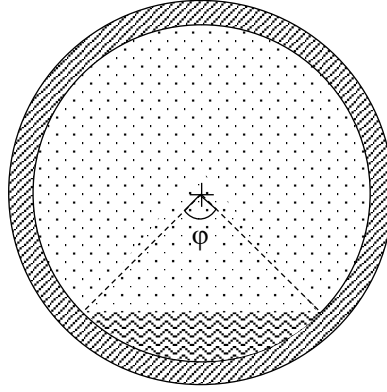


Figure 2.3: Crossection of the tube

Force balance yields:

$$\rho g A l \sin \theta = \tau P_{lw} l \quad (2.1)$$

where  $P_{lw}$  is the wetted perimeter and  $l$  is the length of the tube. Rearranging results in

$$\frac{\tau P_{lw}}{A} = \rho g \sin \theta \quad (2.2)$$

Note that the friction force can be represented by

$$\tau_o = \frac{f \rho V^2}{2} \quad (2.3)$$

where  $f$  is defined as (Blasius 1913)

$$f = \frac{0.079}{Re^{1/4}} \quad (2.4)$$

for  $3000 < Re < 100000$

where  $Re = \frac{D_h V}{\nu}$  and  $D_h = \frac{4A}{S}$ ,  $S = \phi R$ ,  $A = \frac{R^2}{2}(\phi - \sin \phi)$  Using the definition of mass flow rate one can solve the force balance equation.

$$\dot{m} = V A \rho \quad (2.5)$$

However, the friction factor is an unknown to be determined. For a laminar flow Poiseuille in 1839 derived a simple formula  $f = 64/Re$ . It is valid for  $Re < 5000$ .

Prandtl suggested to use the so-called Prandtl - Von Karman formula (1904)

$$\frac{1}{\sqrt{f}} = -2 \log \frac{2.51}{Re \sqrt{f}} \quad (2.6)$$

Both formulations do not take into account the roughness of the pipe wall due to the laminar conditions for the first one and smooth enough surface condition for the latter. Blasius (1912) also came up with a simple solution,

$$f = \frac{0.3164}{Re^{1/4}} \quad (2.7)$$

This formulation is also valid for smooth walls. On the other hand, with increasing turbulence of the flow, the boundary layer gets smaller and the roughness of the tube gets more importance. Nikuradse has proposed a formulation which takes the roughness into account

$$\frac{1}{\sqrt{f}} = -2 \log \frac{k/R_h}{14.8} \quad (2.8)$$

where  $k/R_h$  is the relative roughness of the tube wall. Colebrook has combined the results of Prandtl and Nikuradse and suggested

$$\frac{1}{\sqrt{f}} = -2 \log \frac{k/R_h}{14.8} + \frac{2.51}{Re \sqrt{f}} \quad (2.9)$$

Due to the implicit nature of the formulation, it is hard to solve. Some researchers tried to fit an alternative formulation to this one. Indeed, the approximation of Barr [67] seemed to get attention [68, 69, 70]. Machiels et.al. (2009) mentioned about the ease of use of Barr's formulations and prepared Table 2.1 which is tabulating friction factor formulations according to the flow type [71].

Barr's formulation that mimics Colebrook's equation with less than 1% error is as follows [71] (Machiels et al. 2009).

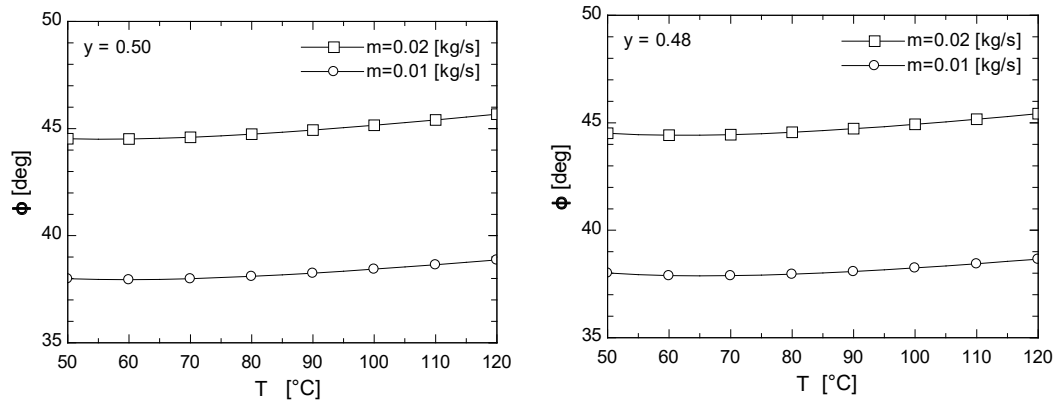
$$\frac{1}{\sqrt{f}} = -2 \log \left( \frac{k}{14.8 R_h} + \frac{4.518 \log(Re/7)}{Re \left( 1 + \frac{Re^{0.52} (k/R_h)^{0.7}}{76.53} \right)} \right) \quad (2.10)$$

Table 2.1: Friction factor formulations

Flow regime	Author	Formula	Validity range
Laminar	Poiseuille	$f = 64/Re$	$Re < 5000$
Smooth turbulent	Prandtl	$\frac{1}{\sqrt{f}} = -2 \log \frac{2.51}{Re\sqrt{f}}$	$k/R_h$ negligible
Transitional	Colebrook	$\frac{1}{\sqrt{f}} = -2 \log \frac{k/R_h}{14.8} + \frac{2.51}{Re\sqrt{f}}$	$\frac{k}{R_h} < \frac{2240}{Re}$
Rough Turbulent	Nikuradse	$\frac{1}{\sqrt{f}} = -2 \log \frac{k/R_h}{14.8}$	$\frac{k}{R_h} < \frac{2240}{Re}$
Macro roughness	Bathurst	$\frac{1}{\sqrt{f}} = -1.987 \log \frac{k/R_h}{5.15}$	$\frac{k}{R_h} > 0.25$

In the calculations Barrs's curve fit diverged from Colebrook's formula at a range of 6 – 7.5% for relative roughness range,  $k/R_h$ , of 0.07 – 0.1 and Reynold's Number of 5000 – 85000. Note that both Colebrook's and Barr's formula are valid in a range of relative roughness between 0 and 0.1 for transitional and turbulent flows.

The friction factor could be studied with widely used Manning's formulation however it is shown that his formulations are not valid for pipes with diameter smaller than 1 meter [72] but for channels like stream beds. Hence, Manning's formulation is not studied in this work. The solutions of  $\phi$  from Figure 2.3 with different mass flow rates and solution mass ratios are demonstrated in Figure 2.4.



(a) variation at mass fraction of 0.50

(b) variation at mass fraction of 0.48

Figure 2.4: Variation of  $\phi$

$y = 0.50$  is the condition of the inlet of the tube and at the exit it may decrease to 0.48. Also the temperature of the solution falls between  $50^{\circ}\text{C}$  and  $120^{\circ}\text{C}$ . The plots show that the angle varies between  $38^{\circ}$  and  $46^{\circ}$  for a fixed  $\theta = 40^{\circ}$ . However, if the amount of the refrigerant produced is calculated, some other effects like the phase change, boiling and variable temperature due to variable mass fraction along the tube should be considered and the calculations get complicated. For a better comprehension of the physics a finite difference method has been used.

## 2.2 Finite difference analysis of absorber tube

The calculation of the amount of the refrigerant produced is calculated using a finite difference method [65]. The PTC is tilted with respect to the horizontal plane enabling the inlet solution of  $\text{NH}_3 - \text{LiNO}_3$  to flow downward from the upper inlet to the bottom end of the tube. Since no pressure difference is supposed to exist at the extremities of the absorber tube, the liquid flow is driven by gravity, partially filling the tube. As the concentrated solar radiation heats the tube, ammonia evaporates from the solution through the liquid free surface, giving rise to an upward vapor flows, which evacuates from the upper end. A stratified two-phase countercurrent flow takes place inside the inclined receiver tube of the solar collector. In order to theoretically investigate the behavior of the proposed generator a steady state 1-D model of the receiver tube is developed [65].

Considering the approximate character of the modelling performed here, some simplifying assumptions can be accepted. Solar driven absorption cycle works in cooling configuration preferably with an air re-cooled cycle in order to avoid a cooling tower for the absorber and condenser heat rejection. Since the radiation absorber tube is directly coupled to the condenser, the working pressure depends on the condenser temperature  $T_c$ , being  $p = p_{s,\text{NH}_3}(T_c)$ , the saturation pressure of the pure refrigerant is a function of  $T_c$ . As a first approximation, condenser and absorber temperatures are assumed to be equal,  $T_{ab} = T_c$ . Ammonia mass fraction in the liquid solution at the inlet of the tube  $x_{in} = x_{ab}$  depends both on  $T_c$  and  $T_{ev}$ . In fact, the solution comes from the absorber, which is supposed to be at the same pressure as the evaporator, which is under saturation condition,  $p_{ev} = p_{s,\text{NH}_3}(T_{ev}) = p_{s,l}(T_{ab}, x_{ab})$ . The liq-

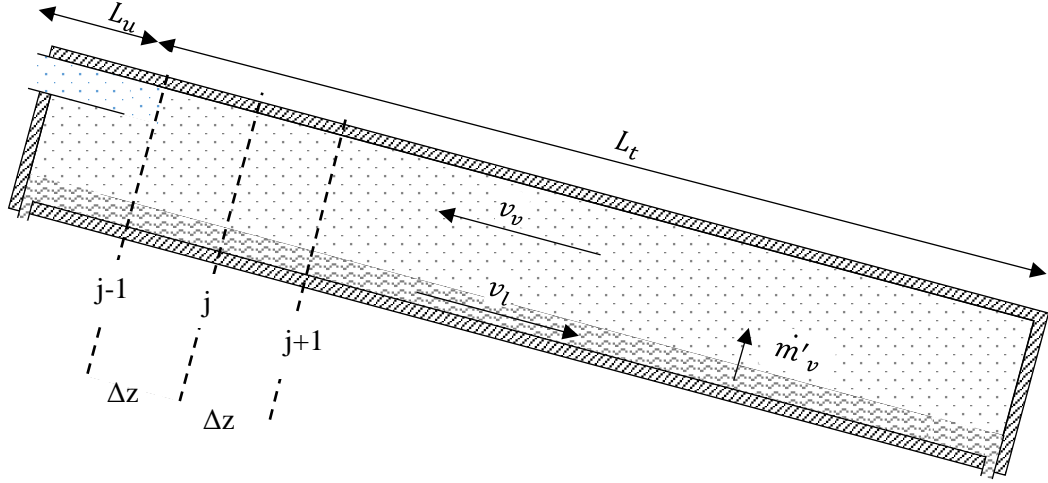


Figure 2.5: Finite difference diagram of the open channel flow

uid solution is supposed to enter the generator tube under saturation condition since the case of subcooled liquid at the inlet is not considered here for simplicity. Liquid temperature is then defined from the saturation curve  $T_{l,in} = T_s(p, x_{in})$ .

The liquid surface can be considered free of viscous stress and the pressure loss of the vapour flow is negligible in front of the liquid gravity effect [64]. Heat and momentum transfer from vapour to liquid can be ignored in front of the wall interaction. As a result, the liquid flow can be solved independently from the vapour phase. In addition, neglecting acceleration effects and assuming constant pressure, the liquid momentum equation gives the sliding velocity as in Eq. 2.11 (2.1). There, the liquid-wall friction coefficient is modelled with the White-Colebrook correlation [73]. For turbulent flow, there is no appreciable change in  $f$  with cross-section shape, as the shear stress is concentrated on the wall and eventually on the interphase [74]. Liquid occupies a circular segment of angle  $\phi$ , so that, according to Figure 2.6, cross-section quantities are as in Eq. (2.2). Introducing a void fraction parameter, liquid and vapor mass conservation result as in Eq. (2.3).

$$v_l = \sqrt{2g \sin \theta \frac{D_{hlw}}{f_{lw}}} \quad (2.11)$$

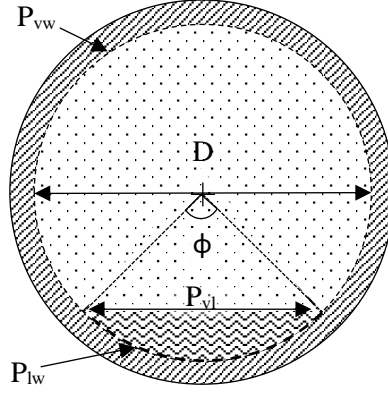


Figure 2.6: Finite difference diagram of the cross section

$$1/\sqrt{f} = -2 \log \left( \frac{\epsilon_w}{3.7 D_{hlw}} + \frac{2.51}{Re \sqrt{f}} \right) \quad (2.12)$$

where  $Re > 4000$ ,  $\epsilon_w < 0.05$

$$\frac{A_l}{A} = \frac{1}{2\pi} (\phi - \sin \phi) \quad (2.13)$$

$$P_{lw} = \frac{\phi D}{2} = \pi D - P_{vw} \quad P_{lv} = D \sin(\phi/2) \quad D_{hlw} = \frac{4A_l}{P_{lw}} \quad D_{hvw} = \frac{4A_v}{P_{vw}}$$

$$\alpha = \frac{A_v}{A} \quad \dot{m}_l = (1 - \alpha) A \rho_l v_l \quad \dot{m}_v = A \alpha \rho_v v_v$$

In general terms, the net incoming heat flux,  $q_w$ , is transferred both to liquid and vapor phases but in the present case the heat transfer coefficient between the wall and the vapor flow is one to two order of magnitude smaller than the liquid phase. This allows us to neglect wall-to-vapor heat transfer as the vapor leaves the liquid at its local temperature. The high conductivity of the tube wall makes it acceptable to consider a uniform wall temperature  $T_w$  at each transversal section, although a better modeling is possible [64]. Thermal losses to the ambient are modeled defining a local collector efficiency  $\eta_c$ , Eq. (2.4), adapted from the formulation given by



manufacturers according to international standards [75].

$$\eta_c = \eta_o - c_1 \frac{(T_w - T_{am})}{I} + c_2 \frac{(T_w - T_{am})^2}{I} - c_3 u \frac{(T_w - T_{am})}{I} \quad (2.14)$$

Being the liquid saturated at the inlet, boiling process takes place as soon as heat flux is applied as the wall temperature exceeds the liquid saturation temperature. In the boiling regime, heat transfer coefficient increases with respect to single-phase regime, due to bubble formation and detachment. Because of that, appropriate correlations are needed to estimate it. The Gungor-Winterton correlation used here is based on the superposition of two contributions, corresponding to convective and nucleate boiling heat transfer mechanisms in Eqs. 2.15 - 2.18 [76].

$$q_w = h_{nd}(T_w - T_s)S + h_{sp}(T_w - T_l)F \quad (2.15)$$

$$S = \frac{1}{1 + 1.15 \times 10^{-6} F^2 Re_l^{1.17}} \quad (2.16)$$

$$h_{sp} = Nu \frac{k}{D_{hlw}} \quad (2.17)$$

$$Nu = \frac{(f/8)(Re - 1000)Pr}{1 + 12.7(f/8)^{1/2}(Pr^{2/3} - 1)} \quad (2.18)$$

The nucleate boiling term depends on  $h_{nb}$ , which represents the heat transfer coefficient under pool boiling conditions. The suppression factor  $S$  takes into account the difference between pool and flow boiling. The enhancement factor  $F$  accounts for the increase over the pure convective heat transfer, caused by the increasing vapour quality in the flow downstream.  $F = 1$  at zero vapor quality (inside the liquid) as in the present case. In fact, vapor produced by the boiling process does not accumulate within the liquid flow but it evacuates through the liquid-vapor interface, incorporating to the separate vapor flow. Single-phase heat transfer coefficient  $h_{sp}$  is estimated using the Gnielinski correlation [73], as indicated in Eq. 2.18.

Boiling heat transfer coefficient  $h_{nb}$  has been modified from the original Gungor-Winterton correlation, which was developed for pure substances. Instead of using Cooper's correlation for  $h_{nb}$ , which requires an estimation of the critical pressure for the liquid substance, here the correlation [77] has been used instead, Eq. 2.19. In addition, dealing with the  $NH_3 - LiNO_3$ , the effect of the two components on the heat transfer must be considered. Existing correlation developed for pure substances can be modified using proper correction factors.  $h_{nb,mix} = h_{nb}F_{me}$  can be used in Eq.2.15 instead of  $h_{nb}$ . Ünal (1986) developed an empirical method for predicting the mixture effect on the heat transfer knowing only the equilibrium data [78], Eqs. 2.20 - 2.25.

$$h_{nb} = \frac{207k_l}{D_d} \left( \frac{q_w D_d}{k_l T_s} \right)^{0.745} \left( \frac{\rho_v}{\rho_l} \right)^{0.581} Pr_l^{0.533} \quad (2.19)$$

$$D_d = 0.0146\beta \left( \frac{2\sigma_l}{g(\rho_l - \rho_v)} \right)^{0.5} \quad (2.20)$$

$$\frac{h_{nb,mix}}{h_{nb}} = [(1 + (b_2 + b_3)(1 + b_4))(1 + b_5)]^{-1} \quad (2.21)$$

$$b_2 = (1 - x') \ln \left( \frac{1.01 - x'}{1.01 - y'} \right) + x' \ln \left( \frac{x'}{y'} \right) + |y' - x'|^{1.5} \quad (2.22)$$

$$b_3 = \begin{cases} 0 & \text{for } x' \geq 0.01 \\ (y' - x')^{0.1} - 1 & \text{for } x' < 0.01 \end{cases} \quad (2.23)$$

$$b_4 = 152(p/p_{c,NH_3})^{3.9} \quad (2.24)$$

$$b_5 = 0.92|y' - x'|^{0.001}(p/p_{c,NH_3})^{0.66} \quad (2.25)$$

Vapor ammonia generation along the tube length results from bubbles formation at wall-liquid surface and their migration into vapor flow through the liquid-vapor interface. Unlike pure substances, the phase change of mixture does not occur at constant

temperature. When the evaporation of the more volatile component takes place at constant pressure, its mass fraction in the liquid neighborhood decreases while the saturation temperature grows and after mixing the effect incorporates into the bulk of the liquid. A portion of the input heat flux contributes to phase change  $q_{ev}$  while the other  $q_l$  sustains the liquid heating, being  $q_w = q_{ev} + q_l$ . Evaporation linear rate  $\dot{m}'_v$  is related to evaporation heat flux  $q_{ev}$  as indicated in Eq. 2.29, explained in what follows. A simple partitioning model can be obtained assuming that vapor generation occurs under saturation condition as a superposition of heating at constant mass fraction and phase change at constant temperature. The increment of the bulk liquid temperature downstream  $dT_l$  must equate the increment of saturation temperature due mass fraction reduction  $dT_s(x, p)$  Eqn.2.26, within the same interval  $dz$ . Mass fraction variation  $dx_b$  can be formulated starting from the definition in Eqn.2.26, with the non-volatile mass flow ( $LiNO_3$ )  $\dot{m}_{NVO}$  considered constant,  $d\dot{m}_{NVO} = 0$ . With  $dp = 0$  an expression for evaporation heat flux  $q_{ev}$  results as in Eq.2.29

$$dT_s = \frac{q_l P_{wl}}{c_{pl} \dot{m}_l} dz = \frac{\partial T_s}{\partial x_b} dx_b + \frac{\partial T_s}{\partial p} dp \quad (2.26)$$

$$x_b = \frac{\dot{m}_{VO}}{\dot{m}_{VO} + \dot{m}_{NVO}}, \quad \dot{m}_l = \dot{m}_{VO} + \dot{m}_{NVO} \quad (2.27)$$

$$dx_b = \frac{(1 - x_b)}{\dot{m}_l} d\dot{m}_{VO} \quad (2.28)$$

$$q_{ev} = \frac{q_w}{1 - \frac{c_{pl}(1 - x_b)}{i_{lv}} \frac{\partial T_s}{\partial x}} \quad (2.29)$$

The approach used here to model the flows is an advanced Eulerian scheme, which progressively proceeds from the liquid entrance section toward the bottom exit. Once liquid flow is solved, vapor flow is modeled proceeding from the bottom closed end to the top entrance along the tube length. Mass flow is null at the bottom end and it progressively grows due to the contributions of ammonia evaporated from the liquid flow. It evaporates at saturation temperature corresponding to the local liquid temperature. Owing to the separated flow approach, the numerical load is strongly

reduced with respect to applying full two-phase flow governing equations. Pure ammonia thermodynamic and transport properties are taken from Kretzschmar (2016) [79].  $NH_3 - LiNO_3$  properties are taken from the works of Libotean and Garousi [80, 81, 82].

### 2.3 Simulation of the cycle

Beside the physics in the desorber tube, the effect of the robust cycle is studied with the iterative solution of the whole cycle. The cycle has two pressure levels: the condenser, solution heat exchanger and the tube of the parabolic trough contain a high pressure flow, whereas the rest contains a lower pressure flow. As a result, the whole desorber tube has a fairly constant pressure along its longitudinal axis equal to the condenser saturation pressure. The parabolic trough mirror is reflecting the solar radiation uniformly along the tube. However, some portion of it is transferred to the solution and some to the refrigerant. That portion varies with the position of the sun, although it is explain that the heat fraction going to the vapor flow can be neglected in the first approximation [64]. Therefore, the flowing regime is explained as stratified separated flow with an essentially flat interphase, eventually wavy if a large tilting angle is selected. Possible hydraulic jumps at the exit can be neglected.

The mass ratio,  $y$ , of the solution inside the tube is defined as the ratio of the mass flow rate of the dissolved refrigerant ( $r$ ) to that of the solution ( $s$ ), which have positive values.

$$y = \frac{\dot{m}_r}{\dot{m}_s} \quad (2.30)$$

$y$  is decreasing with the amount of separation of refrigerant from the solution when it is flowing downstream along the longitudinal axis. As a result, the mass ratio at the inlet of the tube is higher than the exit. The temperature of the solution is a function of mass ratio and pressure where the former one varies and the latter one is assumed to be constant along although a negligible pressure drop is necessary for the vapor

upward flow.

$$T_s = f(y, P) \quad \text{or} \quad T_s \rightarrow T_s(z) \quad (2.31)$$

The bulk flow velocity of refrigerant vapor at the lower end of the tube is zero and is increasing toward the upper part as a result of the increase of vapor mass from boiling. Even though the refrigerant is generated along the tube, some portion can be absorbed upon meeting a possible subcooled solution at the upper part. The subcooled liquid flow reaches its saturation condition in a lower part of the tube and leaves the tube boiling. Consequently, in the tube, three critical liquid temperatures can be identified; inlet, onset of saturation and exit temperatures where  $T_{in} \leq T_{sat} < T_{exit}$ . If the solution is already saturated while entering the tube, inlet and saturation temperature for the highest mass ratio are the same. If absorption occurs when the refrigerant meets the subcooled solution, the mass ratio at the inlet and at the onset of the saturation may differ. In Fig. 2.7 the flow is visualized and  $y^-$  represents the mass ratio at the exit,  $y > y^-$ . Wavy arrows represent the production of refrigerant.

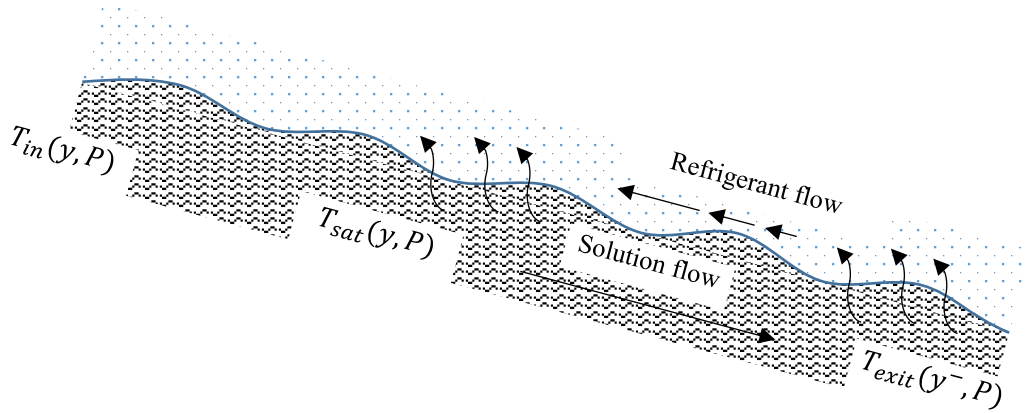


Figure 2.7: Critical temperatures of solution

The energy balance of the tube with either streams perfectly mixed can be formulated as

$$\dot{H}_s^{in} - \dot{H}_s^{exit} - \dot{H}_r^{exit} + \dot{Q}_{in} - \dot{Q}_{loss} = 0 \quad (2.32)$$

where,  $s$  and  $r$  stand for solution and refrigerant respectively. The energy of flow is

calculated by their mass flow rates and enthalpies,  $\dot{H} = \dot{m}h$  where  $h = h(T, y)$  and  $y$  is the refrigerant mass fraction of the solution.

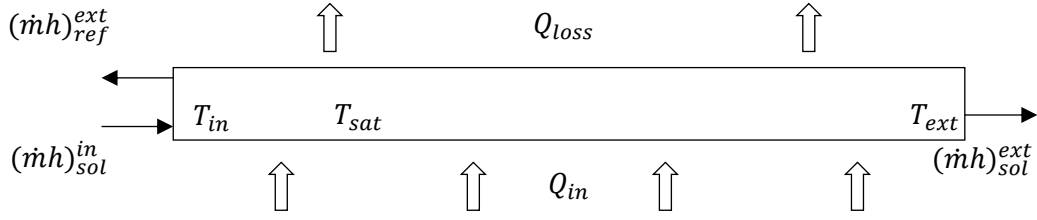


Figure 2.8: Energy balance of the tube

Detailed calculation of heat losses is troublesome for such systems due to the complex physics involved. Rather than that, empirical formulas for overall heat transfer coefficients is of common use representing commercial absorber tubes. The overall standardized characteristic equation of the tube estimates the heat losses as mentioned earlier in Eq. 2.14. For a higher accuracy, heat losses are here separated into two distinct zones: Subcooled and saturated. The heat loss formula for a tube of diameter  $D$  and length  $L$  is

$$\dot{Q}_{loss} = \pi DL [c_1(T_{ave} - T_a) + c_2(T_{ave} - T_a)^2 + c_3(T_{ave} - T_a)v_{wind}] \quad (2.33)$$

$$\begin{aligned} c_1 &= 0.358[Wm^{-2}K^{-1}] \\ c_2 &= 0.0019[Wm^{-2}K^{-2}] \\ c_3 &= 0.116[Jm^{-3}K^{-1}] \end{aligned} \quad (2.34)$$

$T_{ave}$  is the flow average temperature of the zone of interest.  $T_a$  is the ambient temperature,  $v_{wind}$  is the wind speed. Due to the two different temperature zones, heat losses are calculated separately for those zones of length  $L_{sub}$  and  $L_{sat}$ .

### 2.3.1 Mass Balance of the Absorption cycle

The refrigerant ( $r$ ) is generated from the rich solution and the remaining is called the weak solution. One has to consider that the amount of salt in the solution does not

change. The superscript “<sup>-</sup>” indicates that the property belongs to the weak solution.

$$\Sigma \dot{m} = 0 \quad (2.35)$$

$$\dot{m}_r = \dot{m}_s - \dot{m}_s^- \quad (2.36)$$

$$\dot{m}_r = x_3 \dot{m}_s + y(1 - x_3) \dot{m}_s - y^- \dot{m}_s^- \quad (2.37)$$

Eq. 2.37 is evaluated at the boundary of the desorber tube. The first term on the right hand side of the equation is the contribution of gas phase at the inlet, second term is the amount of refrigerant in the liquid phase at the inlet and the last one is the refrigerant mass in the weak solution leaving the tube. Note that the inlet condition of the tube can be single phase or two-phase. Which, in other words, means that the solution inlet condition can be subcooled (sub) or saturated liquid (sat) with an unknown quality.

### 2.3.2 Energy Balance of the Absorption Cycle

The first law of thermodynamics is applied to the individual components of a single effect absorption cycle for steady-state conditions.

$$\Delta H = Q - W \quad (2.38)$$

The detailed form of the first law is demonstrated in Tab. 1 as a set of governing equations, according to the numbering of Fig. 1.21 where  $Lmtd$  is the logarithmic mean temperature difference,  $\nu$  is the specific volume,  $UA$  is the thermal conductance and  $G_{bt}$  the tilted beam irradiance on the aperture width  $W_a$ .

Besides the mass and energy balance equations some complementary equations and assumptions are necessary in order to equate the number of equations to the number of variables. The higher pressure is set to the condensation saturation pressure in the condenser and the lower pressure is set to evaporation saturation pressure in the

Table 2.2: First law of thermodynamics for the components

Component	Equation
Absorber	$\dot{m}_{10}h_{10} + \dot{m}_6h_6 - \dot{Q}_{abs} - \dot{m}_1h_1 = 0$
	$\dot{Q}_{abs} = \dot{m}_{13}(h_{14} - h_{13})$
	$Lmtd_{abs} = \frac{[(T_6 - T_{14}) - (T_1 - T_{13})]}{\ln[(T_6 - T_{14})/(T_1 - T_{13})]}$
	$\dot{Q}_{abs} = Lmtd_{abs}UA_{abs}$
Pump	$h_2 = h_1 + \frac{W_p}{\dot{m}_1}$
	$w_p = \dot{m}_1v(p_h - p_l)/\eta$
Solution Heat Exchanger	$\dot{Q}_{hex} = \dot{m}_1(h_3 - h_2) = \dot{m}_4(h_4 - h_5)$
Solution expansion valve	$m_6h_6 = m_5h_5$
Desorber tube	$x\dot{m}_3h_{3,r} + (1 - x)\dot{m}_3h_{3,s} - \dot{m}_4h_4$
	$- \dot{m}_7h_7 + \dot{Q}_{in} - \dot{Q}_{loss} = 0$
	$\dot{Q}_{in} = G_{bt}W_aL_{sub}\eta_{op}$
	$\dot{Q}_{in} - \dot{Q}_{loss,sub} = m_1c_p(T_{sat} - T_3)$
	$\dot{Q}_{loss} = \dot{Q}_{loss,sub} + \dot{Q}_{loss,sat}$
	$\dot{Q}_{loss,sub} = \pi DL_{sub}(c_1(T_{ave,sub} - T_a)$
	$+ c_2(T_{ave,sub} - T_a)^2$
	$+ c_3(T_{ave,sub} - T_a)v_{wind})$
	$\dot{Q}_{loss,sat} = \pi DL_{sat}(c_1(T_{ave,sat} - T_a)$
	$+ c_2(T_{ave,sat} - T_a)^2$
	$+ c_3(T_{ave,sat} - T_a)v_{wind})$
	$T_{ave,sub} = (T_3 + T_{sat})/2$
	$T_{ave,sat} = (T_{sat} + T_4)/2$
	$L = L_{sub} + L_{sat}$



Table 2.3: First law of thermodynamics for the components (Continued)

Component	Equation
Condenser	$\dot{Q}_{con} = \dot{m}_7(h_7 - h_8) = \dot{m}_{15}(h_{16} - h_{15})$
	$Lmtd_{con} = \frac{[(T_8 - T_{15}) - (T_8 - T_{16})]}{\ln[(T_8 - T_{15})/(T_8 - T_{16})]}$
	$\dot{Q}_{con} = Lmtd_{con}UA_{con}$
Refrigeration expansion valve	$\dot{m}_9h_9 = \dot{m}_8h_8$
Evaporator	$\dot{Q}_{eva} = \dot{m}_9(h_{10} - h_9) = \dot{m}_{17}(h_{17} - h_{18})$
	$Lmtd_{eva} = \frac{[(T_{17} - T_{10}) - (T_{18} - T_{10})]}{\ln[(T_{17} - T_{10})/(T_{18} - T_{10})]}$
	$\dot{Q}_{eva} = Lmtd_{eva}UA_{eva}$

evaporator. Saturation is also assumed at the exit of the desorber. The refrigerant temperature leaving the desorber tube is assumed to be at the local saturation temperature at the solution exit. The flow regime may be two-phase depending on the condition at the exit of the expansion valves and at the inlet of the desorber tube (points 6, 9 and 3 respectively in Fig. 1.21). This condition enables the inlet of the desorber tube to incorporate vapor to the exit stream immediately. As a result, subcooled and saturated flows can be observed inside the whole tube at the same moment.

The simulation requires several input data in two categories. The first one relies on assumptions and the second one relies on measured data. The optical efficiency of the parabolic trough collector is taken to be a constant value, which is a typical value for reflectors with high optical quality [83]. Beside those, the length (3m) and aperture area (3.42m<sup>2</sup>) of the single PTC and the diameter of the desorber tube (0.03 m) are measured data from the real experimental setup. The direct solar irradiance on a 40° tilted, east-west tracking surface and the temperature values are measured for every 10 minutes on representative days in Madrid, Spain. The solution is composed of  $NH_3$  and  $LiNO_3$  with equal masses which results in a mass ratio of 0.5. Two test cases have been taken for the mass flow rate of rich solution, 0.01 and 0.02kg s<sup>-1</sup>.

The solution in the modelling is a mixture of  $NH_3$  and  $LiNO_3$ . The thermodynamic properties of the solution are evaluated from Ferreira [34] and the refrigerant ( $NH_3$ )

ones are from Tillner-Roth [84]. The set of governing equations is non-linear so that an iterative method must be used for the resolution. The mathematical tool that is used to solve those equations iteratively at once is called Engineering Equation Solver, EES [85].

## 2.4 Simulation of PTC Area

The practical use of the cycle is of importance to commercialize an absorption machine. Beside its COP and cooling power it is important to calculate the necessary amount of solar collector area in order to implement the system to real houses. Famiglietti et al. (2018) [65] simulated the flow inside the tube at steady-state conditions using a 1-D model. López et.al. [86] have simulated for transient flow. These simulations can be considered to be the investigation of only the desorber component of the whole cycle. In order to understand the complete contribution of the design to an absorption cycle, experiments and simulation of the whole system are needed. Due to high costs and time consuming nature of experiment it is reasonable to start the investigation with a simulation of the system beforehand using well established techniques, explore the design variables and propose improvements. In the current work, the aforementioned parabolic trough collector is inserted as a desorber in a hypothetical single-effect absorption cycle. In order to evaluate its capabilities for a representative application the whole cycle has been solved mathematically in order to investigate the potential of the design to meet the cooling demand of a representative studio flat. The cooling demand of a  $30m^2$  flat has been obtained from the calculations of Sahin et al. [87]. On the other hand, the simulations involve the meteorology data measured in Madrid, Spain. Five representative days have been selected for the months from May to September. The representative days are the closest clear days to the mid of the months in 2017. The calculations are performed with a nonlinear equation set solver called Engineering Equation Solver [85]. The required number of PTC has been calculated.

The simulation requires several input data in two categories. The first set is based on assumptions and the other is measured data. The assumed input parameters are constant  $UA$  values of the heat exchangers.  $UA$  values for the absorber, condenser,

evaporator and solution heat exchanger are  $1.8kW K^{-1}$ ,  $1.2kW K^{-1}$ ,  $2.25kW K^{-1}$  and  $0.132kW K^{-1}$  respectively [20]. The optical efficiency of the parabolic trough collector is taken to be a constant value as well. Beside those, the length ( $3m$ ) and aperture area ( $3.42m^2$ ) of the PTC, the diameter of the desorber tube ( $0.03m$ ) are measured data from the real setup. The direct solar radiation on a  $40^\circ$  inclined, east-west tracking surface is measured. The values are from representative and clear days of each month. The ambient temperature values are estimated using sinusoidal curve fit where maxima and minima are the average values of the months. The solution composes of  $NH_3$  and  $LiNO_3$  with equal masses which results in a mass ratio of 0.5. The mass flow rate has been fixed to  $0.005kg s^{-1}$  in the desorber tube. On the other hand, the solution mass flow rate through the pump varied linearly with the number of the PTCs. The evaporation temperature is assumed to be  $10^\circ C$ .

The solution in the modelling is a mixture of  $NH_3$  and  $LiNO_3$ . The thermodynamic properties of the solution are evaluated from Ferreira [34] and the refrigerants' ( $NH_3$ ) are from Tillner-Roth [84]. The set of the equations is non-linear and an iterative method supposed to be used. The mathematical tool that is used to solve those equations iteratively at once is called Engineering Equation Solver [85].

The energy demand of a studio flat has been calculated by Şahin et. al. [87]. The illumination, electrical equipment, and human heat loads are calculated to be  $750W$ ,  $500W$  and  $130W$  respectively. Their calculations reflect the hourly change in the heat loads of a simple mid floor flat. The flat is assumed to have two exterior walls facing south and west with thickness of  $0.2m$  where heat input is possible and two interior walls where heat transfer is ignored. There are two windows on the exterior walls with total area of  $8m^2$  and the total volume of the flat is taken as  $90m^3$  with  $30m^2$  base area. The comfort temperature is assumed to be  $24^\circ C$ . The minimum and maximum cooling loads are summarized in Table 2.4. The minimum and maximum temperatures are demonstrated in Table 2.5. The hourly variation of cooling load and ambient temperature is assumed to a sine curve. Both values are fit into sinusoidal curves to mimic the daily variations where the minimum and maximum amounts are assumed to occur at 4 am and 4 pm respectively. The sinusoidal curve fits are plotted in Figure 2.9 and Figure 2.10. The hours in the plots are watch times.

Table 2.4: Minimum and maximum cooling loads

	May	Jun	Jul	Aug	Sep
Minimum, kW	2.60	3.80	4.06	3.88	3.69
Maximum, kW	5.19	8.59	9.06	9.61	10.27

Table 2.5: Minimum and maximum temperature

	May	Jun	Jul	Aug	Sep
Minimum, °C	11.3	16.1	19.0	18.8	15.4
Maximum, °C	22.2	28.2	32.1	31.3	26.4

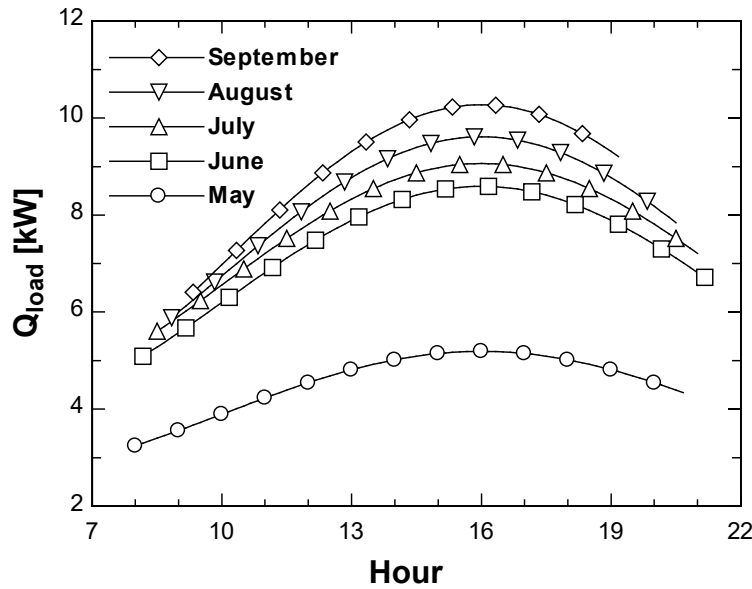


Figure 2.9: Cooling load of the cycle

All in all, the physics of the fluid inside the collector tube is examined and the information is used for the simulations. The finite difference simulation has been prepared to understand the effects of different variables in the tube and besides, thermodynamics simulations to calculate the required amount of solar collectors to maintain human comfort. This chapter has examined the necessary equation to solve and needed input parameters to complete the set of equations.

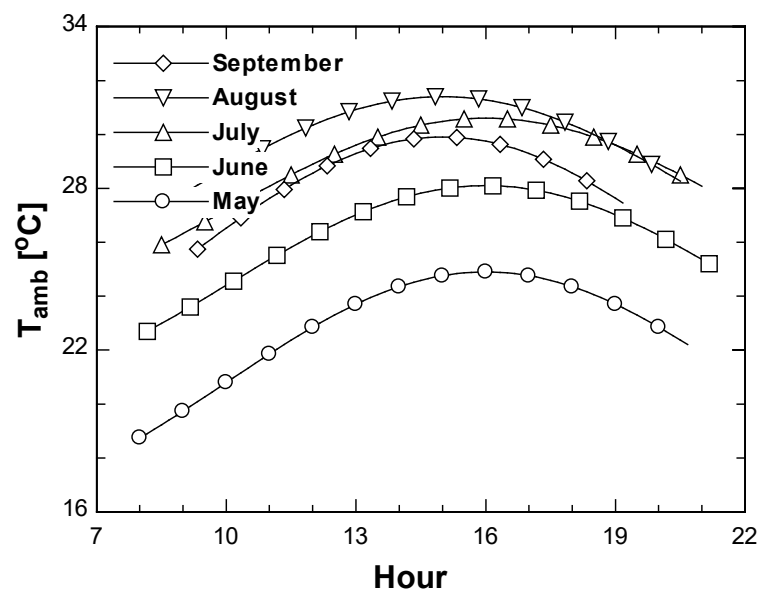


Figure 2.10: Ambient temperature



## CHAPTER 3

### EXPERIMENTS

The simulations of the proposed design has several assumptions. It is needed to support the study with observations of the physics so that one should be sure that the assumptions hold. Hence, an experimental setup has been constructed in order to verify the results. The experiment of the parabolic trough collector (PTC) as a desorber has been conducted. PTC has  $3.42m^2$  aperture area and has a length of  $3m$ . The technical drawing of the PTC has been attached to the Appendix A. It has a East-West tracking system with a crane to adjust the inclination angle. The absorber tube has an inner diameter of  $6cm$  with a glass envelope. The envelope is not in vacuum however it is well covered. The solar absorber tube has an inlet of rich solution of  $NH_3 - LiNO_3$  and two exists of weak solution and  $NH_3$  as a refrigerant. The setup has one mass flow meter for each inlet or exit.

The pump has been manufactured by Roto pumps for chemicals. It has a flow rate of about  $180l/h$ . The technical details and the performance curve of the pump has been attached to the Appendix A. The condenser, evaporator and heat exchanger's technical drawings and information are at the Appendix A.

The coriolis flow meters are manufactured by Micro Motion. The device is capable of measuring the mass flow rate, volumetric flow rate, density and temperature. The mass/volumetric flow rate, density and temperature can be measured up to  $\pm 0.05\%$  of the flow rate,  $\pm 0.0002g/cm^3$  and  $\pm 1\%$  of precision.

The exit of the solar receiver tube is mounted to a one litre container in order to be sure that vapor bubbles do not circulate in the pipeline. The level of the container has been also measured continuously with a precision of  $\pm 1mm$ .

The pressure sensors are before and after the volumetric pump. The precision of the sensors is  $\pm 0.1\%$ . The thermocouples are placed in various points of the setup. The calibration of the thermocouples have been made by using a reference thermometer. Two different water reservoirs have been prepared. One of them contains ice and water and the other one is left at ambient temperature. According to the variation from the reference thermometer calibration curves and equations have been generated. The curves have been observed as linear in the form of  $T_{corrected} = aT_{measured} + b$  where  $a$  and  $b$  are to be determined from the measured data.

A photo of the setup is at Figure 3.1 and the technical drawing is in Appendix A.

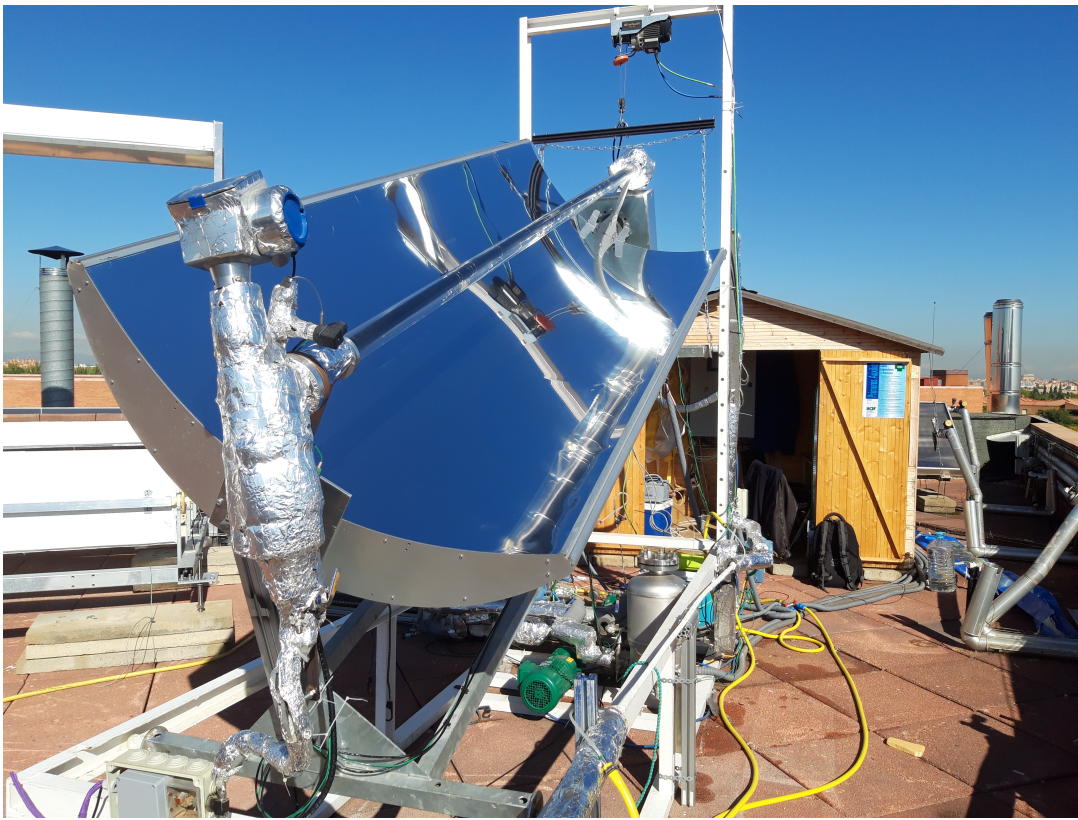


Figure 3.1: Experimental Setup

The flow transmitting units, including pipelines and reservoir but not the receiver tube, have been insulated by glasswool, plastic sponge and aluminum paper.

The system has been filled by  $NH_3 - LiNO_3$  with a mass ratio of 0.5. Hence the weights of the  $NH_3$  and  $LiNO_3$  are equal inside the cycle. In order to avoid any unwanted substance inside the pipeline, like air and water, before loading the solution



the system is kept under vacuum for 24 hours. Under vacuum condition  $NH_3 - LiNO_3$  mixture has been connected to the system and the vacuum sucked all the necessary amount of liquid solution inside the system.

The rich solution is pumped to a heat exchanger and proceed to the inlet of the PTC. The collector has two exits. One is for solution and the other one is for vapor. The solution loses some of its  $NH_3$  and it is called a weak solution. After leaving the PTC, it fills a container tank to avoid bubbles. The container has an exit at the bottom to carry the weak solution to the heat exchanger that has been mentioned recently. The aim of the heat exchanger is to preheat the rich solution. Later, the weak solution goes to the absorber where it meets with the  $NH_3$  vapor that has been generated in the receiver tube of the PTC. The absorber is basically a heat exchanger where two internal flows can mix but cooling fluid, in this case air, do not mix. The system has no condenser and evaporator as they are necessary to create a complete absorption cycle. However, the experimental setup is considered only for mimicking the PTC as a desorber. The crucial point is to find out if a necessary amount of refrigerant could be generated for the proposed design.

The experiment starts with the launch of the pump. When solution circulated in the pipeline, the collector angle is set to focus the radiation on the receiver tube. The angle varies by the sun in a stepwise motion. Every two minutes the angle has changed in order not to lose track of the sun and minimized the incidence angle. The inclination angle of the solar panel has been fixed to  $40^\circ$  which is a very close value to the latitude of the location,  $40.33$ .

The data is collected using a software which is developed specifically for the setup. The values of pressure, temperature and mass flow rates can be observed in real time and saved. Same screen is shared to a PC to ease the observation. All the data collected is summarized in Table 3.1. The data is captured every 6 seconds during the operation.

The steady-state condition is searched during the experiments. In order to accept a data point to be steady state, some conditions are determined. When the pressure, temperature of the solutions, mass flow rates of the solutions and solution reservoir level all together are not varying more than  $\pm 0.025 Pa$ ,  $\pm 0.125^\circ C$ ,  $\pm 0.0017 kg s^{-1}$

Table 3.1: The collected data

Data	Unit
Date-time	$DD/MM/YYYY - HH : MM : SS$
Density of rich solution	$kgm^{-3}$
Density of weak solution	$kgm^{-3}$
Mass flow rate of rich solution	$kg s^{-1}$
Mass flow rate of weak solution	$kg s^{-1}$
Mass flow rate of refrigerant	$kg s^{-1}$
Pressure from 8 points	$kPa$
Atmospheric pressure	$kPa$
Diffusive irradiation	$Wm^{-2}$
Global irradiation	$Wm^{-2}$
Temperature from 22 Points	$^{\circ}C$
Ambient temperature	$^{\circ}C$
Ambient wind speed	$ms^{-1}$

and  $\pm 0.08\%$  respectively the cycle is assumed to be steady state. The raw data is analyzed in MS Excel and Visual Basic (VBA) code is developed to determine the steady-state points and visualized. A representative graph of the steady state points is demonstrated in the Figures 3.2 - 3.5. The vertical lines are to highlight the end of the 2-minutes-steady-state points.

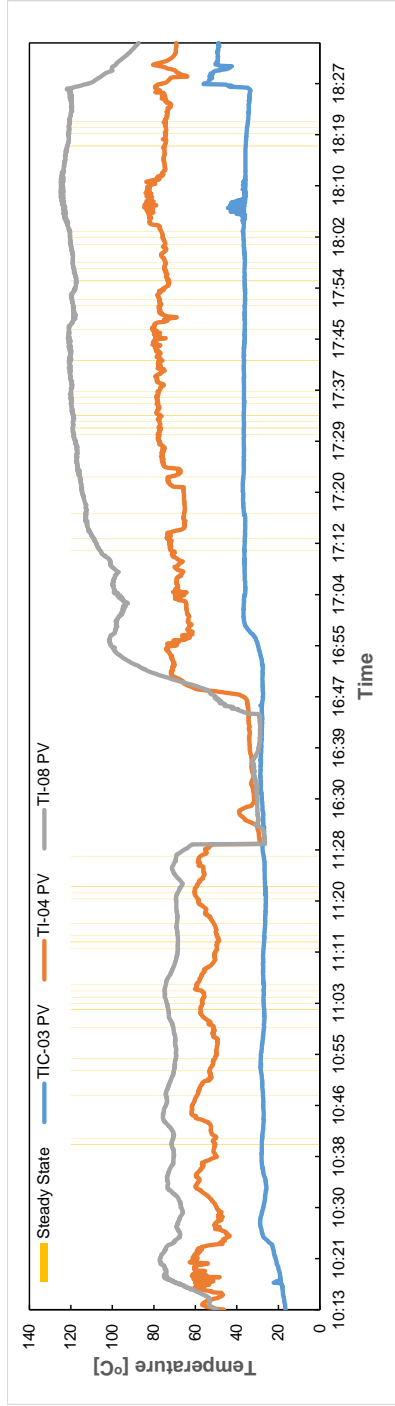


Figure 3.2: Temperature along the tube

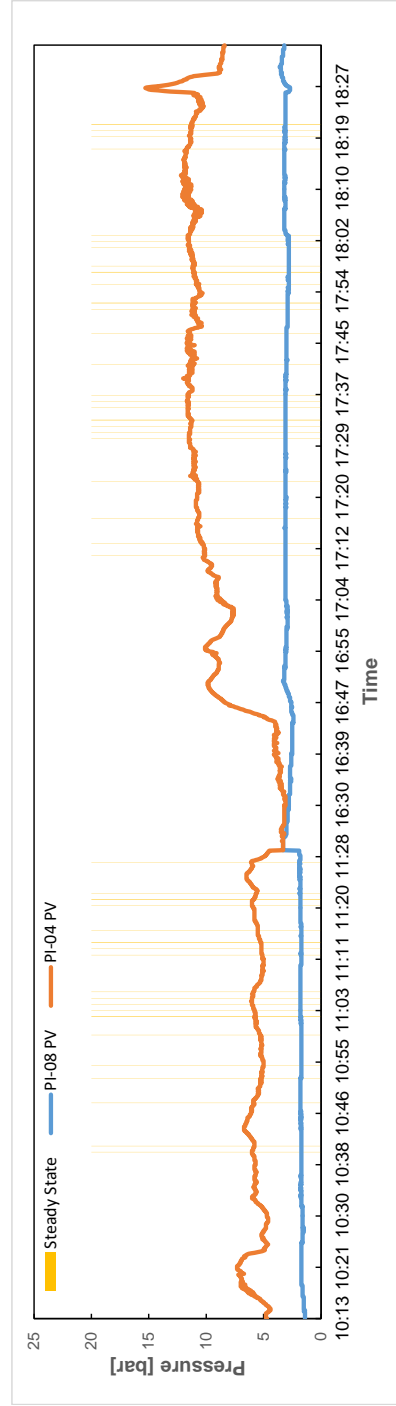


Figure 3.3: Pressure along the tube

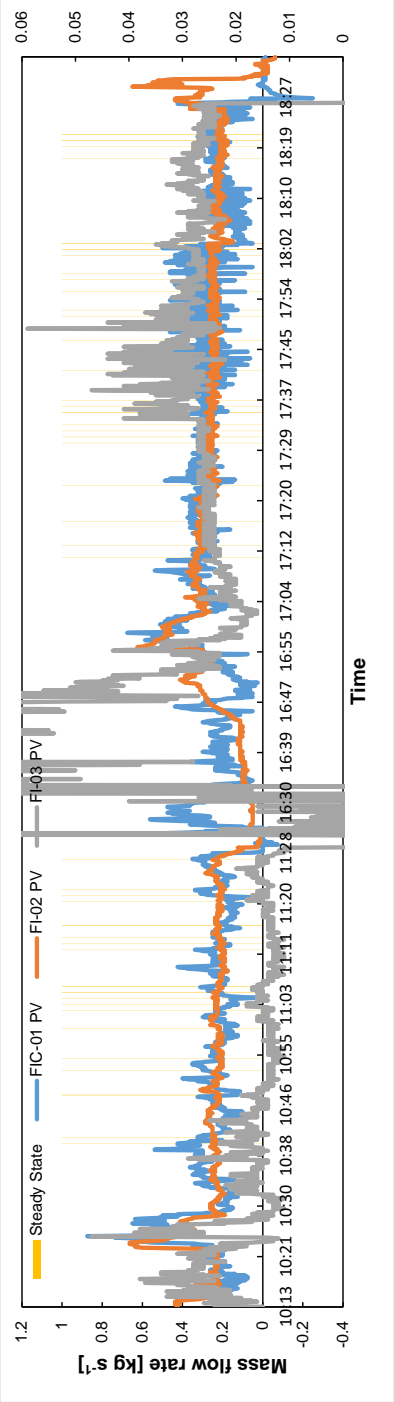


Figure 3.4: Mass flow rate

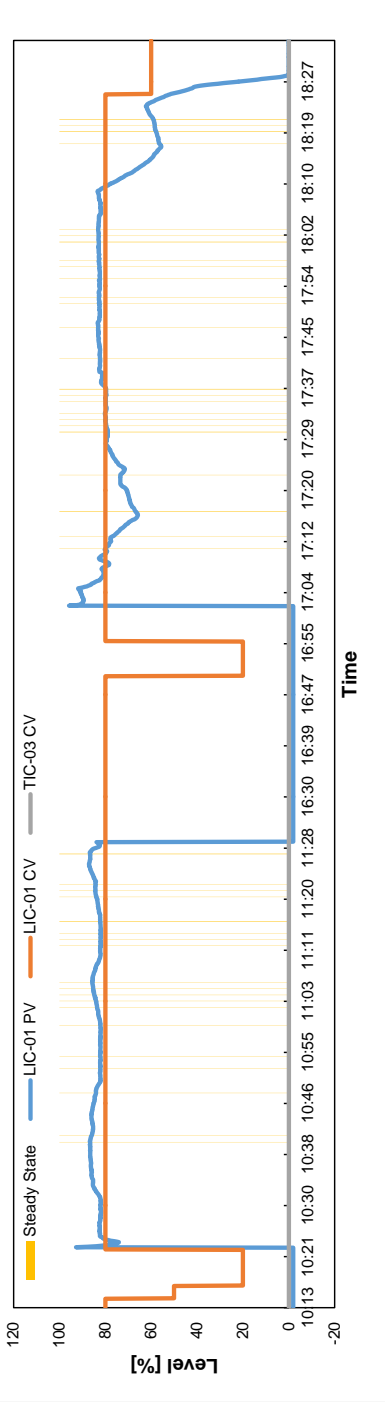


Figure 3.5: Tank Level, Valve Opening, Heater Level

### 3.1 Experimental Uncertainty Analysis

The average of a measured value is calculated over a time  $\tau$  with the Eq. 3.1 where  $R$  is a representative measured data.

$$R_{average} = \frac{\int_0^{\tau} R(t) dt}{\int_0^{\tau} dt} \quad (3.1)$$

Due to the fact that the time intervals are equal, the formula reproduces to the arithmetic mean value of the measured data. The mean value of the successive 12 data points are used during the calculations. However, the precision of the measurement equipment and experimental errors supposed to be calculated and examined as uncertainty of the data. A sample calculation of the measured pressure is demonstrated below. The same analysis is repeated for temperature, mass flow rate and tank level measurements.

Table 3.2: Uncertainty table of Pressure

N	Pressure [bar]	Precision
1	6.06	0.01
2	6.00	0.01
3	6.00	0.01
4	5.93	0.01
5	5.91	0.01
6	5.92	0.01
7	5.97	0.01
8	5.93	0.01
9	5.92	0.01
10	5.85	0.01
11	5.83	0.01
12	5.84	0.01
Mean	5.930833	-
Variance, $\sigma^2$	0.005474	-
Standard Deviation, $\sigma$	0.073988	-

The manufacturer's uncertainty is given by percentage. The value is constant for 3 significant digits at the working conditions of the machine and it is  $0.01Pa$ . The mean value which is  $5.93bar$  would be used in the calculation. The variance is calculated as

$$\sigma^2 = \frac{1}{N} \sum_{i=1}^N (x_i - \bar{x})^2 \quad (3.2)$$

The standard deviation is the square root of the variance which is demonstrated as  $\sigma$ . In the current condition  $\sigma = 0.073988$ . It is converted to measurement uncertainty that has a 95% confidence level [88]

$$p_{measurement} = \pm 1.96\sigma = \pm 1.96(0.073988bar) = \pm 0.145016bar \quad (3.3)$$

The combination of measurement and manufacturers error given by the Eq. 3.4.

$$p_N = \sqrt{\sum_{i=1}^{i=k} p_i^2} = \sqrt{(p_{measurement})^2 + (p_{manufacturer})^2} \quad (3.4)$$

$$p_N = \sqrt{0.147976^2 + 0.01^2} = 0.148314pa$$

As a result, the pressure is measured as  $p = 5.93 \pm 0.15$  pa.

The same calculations have been repeated for temperature, mass flow rate and tank level for the same moment of data points. Table 3.3 shows the measured data and the manufacturer's precision as well as the mean values, standard deviation and uncertainties which are evaluated with the same manner as pressure.

Table 3.3: Uncertainty

N	Temp.	Precision	Flow rate	Precision	Tank level	Precision
1	50.4	0.100	0.250	0.001	86.8	0.100
2	50.7	0.100	0.250	0.001	86.7	0.100
3	51.0	0.100	0.225	0.001	86.6	0.100
4	51.1	0.100	0.250	0.001	86.6	0.100
5	51.4	0.100	0.250	0.001	86.6	0.100
6	51.6	0.100	0.250	0.001	86.4	0.100
7	51.6	0.100	0.225	0.001	86.4	0.100
8	51.4	0.100	0.250	0.001	86.4	0.100
9	51.1	0.100	0.237	0.001	86.4	0.100
10	50.8	0.100	0.250	0.001	86.3	0.100
11	50.5	0.100	0.237	0.001	86.1	0.100
12	50.1	0.100	0.237	0.001	86.1	0.100
Mean	50.97500		0.242583		86.45000	
S. Deviation	0.465698		0.009560		0.210158	
Variance	0.216875		0.000091		0.044166	
M. Uncertainty	0.912768		0.018738		0.411910	
Uncertainty	0.918230		0.018764		0.423874	

For the sample data given in Table 3.3, the temperature is  $50.9 \pm 0.92$  °C, the flow rate is  $0.24 \pm 0.02$  kg/s and the tank level is  $86.5 \pm 0.42$  %.

### 3.2 Evaluation of experimental data

The measurements were done in Madrid in November 2018. The data points to be analyzed are averages of 2 minutes' steady state operations. The collector effectiveness is defined as the ratio of the energy introduced into the solution and refrigerant to the energy received from the solar radiation.

$$\epsilon = \frac{Q_d}{AG_{t,b}} \quad (3.5)$$

In Equation 3.5,  $Q_d$  is the energy transferred to the fluid inside the receiver tube and

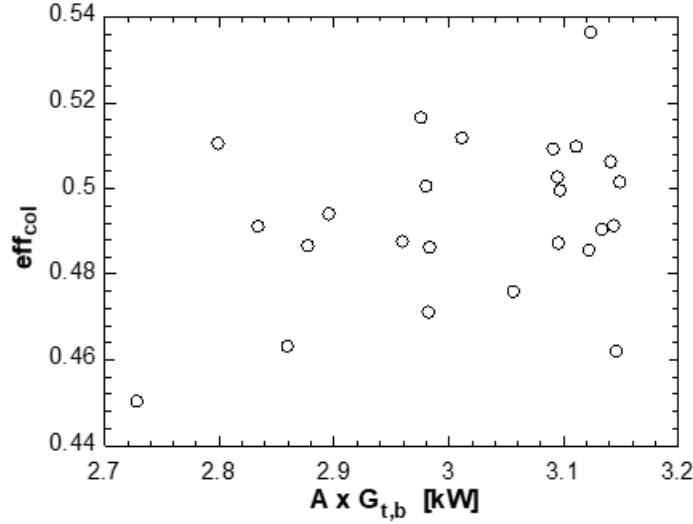


Figure 3.6: Effectiveness of PTC

$A$  is the collector aperture area,  $G_{t,b}$  direct beam irradiance to the E-W single axis tracking fixed tilted surface. The experiment measurements revealed that the PTC worked at an effectiveness between 0.44 and 0.54 (Figure 3.6).

The absorption cooling performance of the cycle depends on the effectiveness of solar collector, however, on the other hand, the length of the subcooled zone in the receiver tube plays an important and adverse role. The subcooled zone is not capable of generating refrigerant. On the contrary, it may absorb the refrigerant. Its temperature may increase due to absorption and heat and mass transfer from the vapor. Note that the vapor continues gaining heat from the receiver tube, although at a lower rate. The temperature of the subcooled zone is increasing which also affects the saturation pressure resulting in unpredictable length for unsteady flows. On the other hand, the experiment results didn't yield a clear correlation between the PTC effectiveness and the length of the subcooled zone. The relation is demonstrated in Fig. 3.7.

The subcooled length is not measured directly however; it is calculated using the flow states. The receiver tube is assumed to have two zones of subcooled and saturated. The thermal losses are calculated separately for each zone using the characteristic equation of the tube as tabulated in Table 2.2. In addition, the heat loss of the subcooled zone can be calculated using the energy balance. The total length of the two



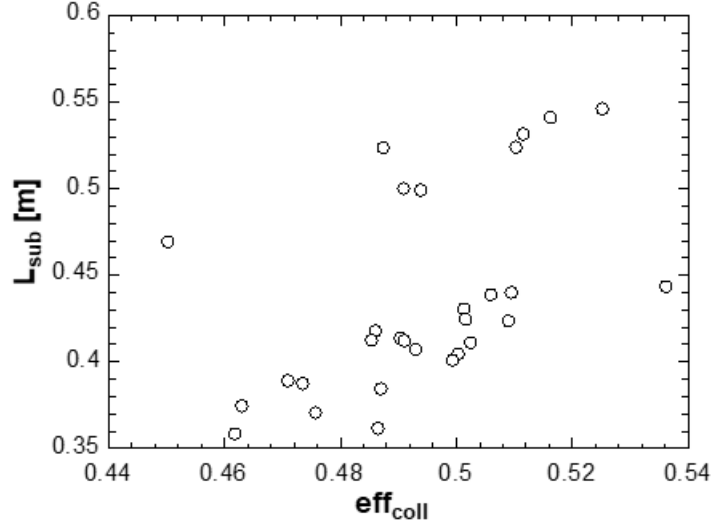


Figure 3.7: Collector effectiveness versus the length of the subcooled zone

zones is equal to the length of the receiver tube.

$$\dot{G}_{bT} W_a L_{sub} \eta_{opt} = \dot{m}_3 (h_{sat} - h_3) + \dot{Q}_{loss,sub} \quad (3.6)$$

$$L_{sub} + L_{sat} = 3m \quad (3.7)$$

$G_{bT}$  is solar irradiance on the tilted surface,  $W_a$  is the width of the PTC,  $\eta_{opt}$  is the optical efficiency of the PTC,  $\dot{m}_3$  is the solution mass flow rate at the inlet of the receiver tube,  $h_{sat}$  and  $h_3$  are the enthalpies at the onset of saturation (end of subcooled zone) and at the inlet (beginning of subcooled zone). The total length of the receiver tube is  $3.00m$ . The remaining variables,  $\dot{Q}_{loss,sub}$ ,  $L_{sub}$  and  $L_{sat}$  which are the thermal losses and the lengths of the subcooled and saturated zones respectively are to be solved. The assumptions in the calculations are that the system is in steady-state and the PTC has a constant optical efficiency.

The length of the subcooled zone is crucial due to the fact that the refrigerant generation does not occur at that zone. One needs to diminish, or vanish if possible, this length in order to achieve higher cooling power. A demonstration of the phenomena is presented in Fig. 3.8. The experimental setup recorded the separation amount and

its percentage. The percentage is compared with the calculated length of the subcooled zone. The data collected accumulated in two ranges of refrigerant separation: first is around 2.5% and the other is around 1.1%. Each range exhibits almost a linear behavior yet, there supposed to be a complete set of data in order to puzzle it out. On the other hand, it is clear that the relation is inversely proportional.

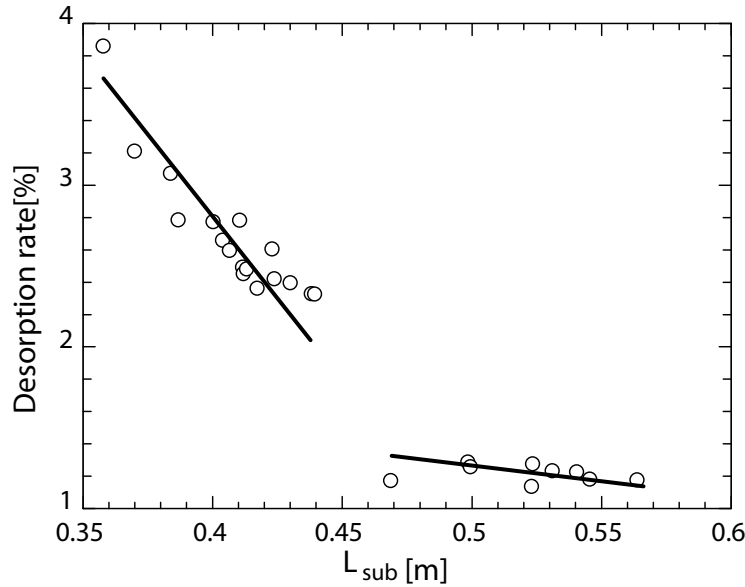


Figure 3.8: The effect of the length of the subcooled zone on the refrigerant separation

The refrigerant flow rate is proportional to the pressure difference in the cycle. The higher pressure in the setup is the saturation pressure of the receiver tube and the lower one is the saturation pressure in the absorber. The pressure difference creates the necessary force to move the refrigerant through the receiver tube. The desorption rate is defined as the ratio of the mass flow rate of the refrigerant to the mass flow rate at the inlet of the receiver tube. Fig. 3.9 illustrates the relation between the pressure difference with the mass flow rate of the refrigerant as linear. A similar pattern is observed in Fig. 3.10 where the refrigerant mass flow rate is plotted against the saturation temperature at the exit of the receiver tube. It is worth mentioning that the pattern is similar due to the linear relation measured between pressure difference and the exit saturation temperature in Fig. 3.11.

In order to achieve higher cooling power, first, the length of the subcooled zone is supposed to be minimized and then, the pressure difference should be increased. The pressure difference is affected by the mass flow rate at the inlet of the receiver tube.

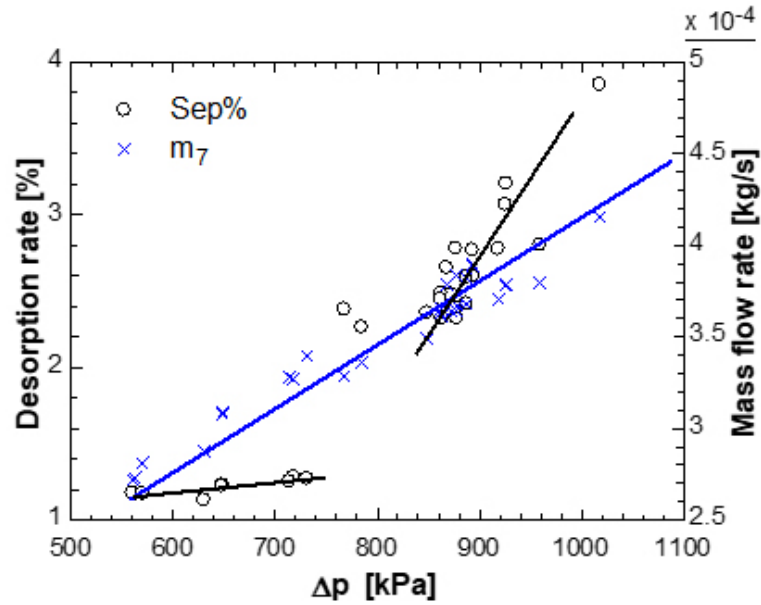


Figure 3.9: Pressure difference versus refrigerant mass flow rate

The measurements showed that they exhibit inversely proportional behavior in Fig. 3.12.

Above all, the incoming radiation plays an important role in the increase of the pressure difference as demonstrated in Fig. 3.13.

The experiments are conducted in Madrid in 2018. The experimental setup is arranged to understand several key points of the proposed designed. First one is the effectiveness of the proposed collector and which factors affect the effectiveness. Second, the length of subcooled zone. Before the experiment the length of the subcooled zone is assumed to have an important effect on the performance of the cycle. The length determined and demonstrated how it effects the desorption rate of the cycle. Mean while, the data collected is used to proove the simulation results from the previous chapter. Next chapter composes of the results of the simulations and the output of the experiments as well as their comparison.

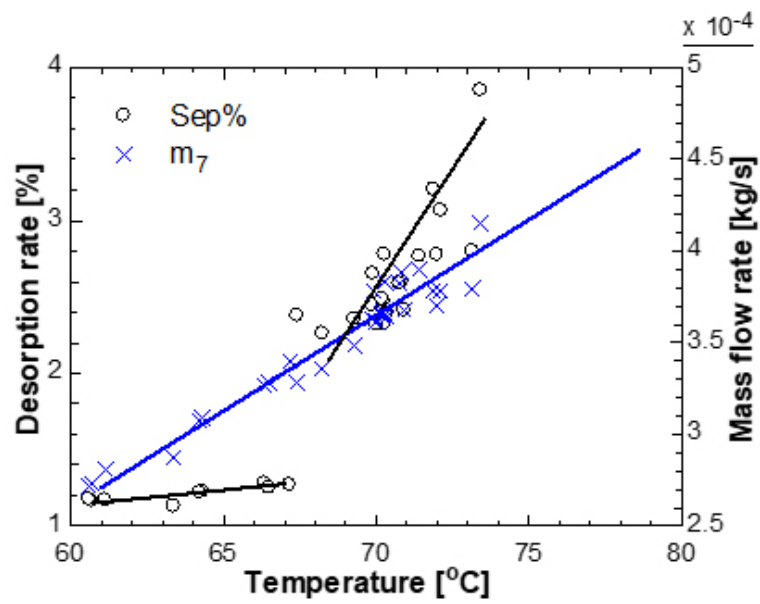


Figure 3.10: Saturation temperature versus refrigerant mass flow rate

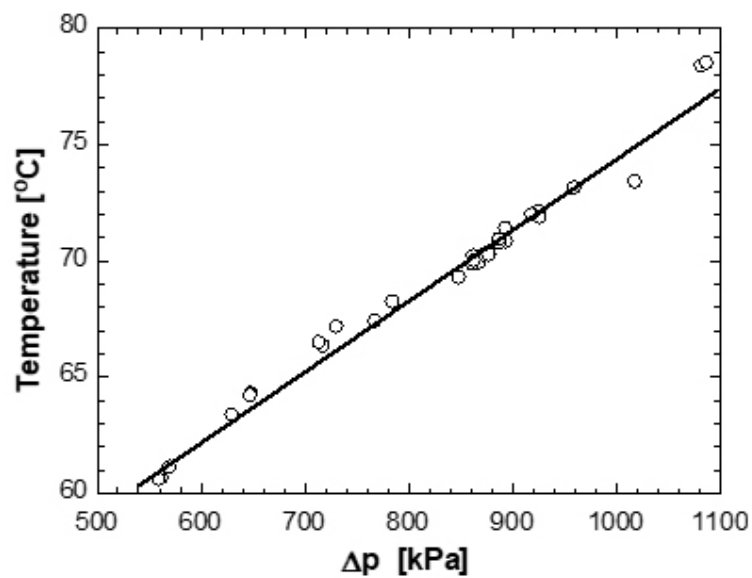


Figure 3.11: Pressure difference versus saturation temperature

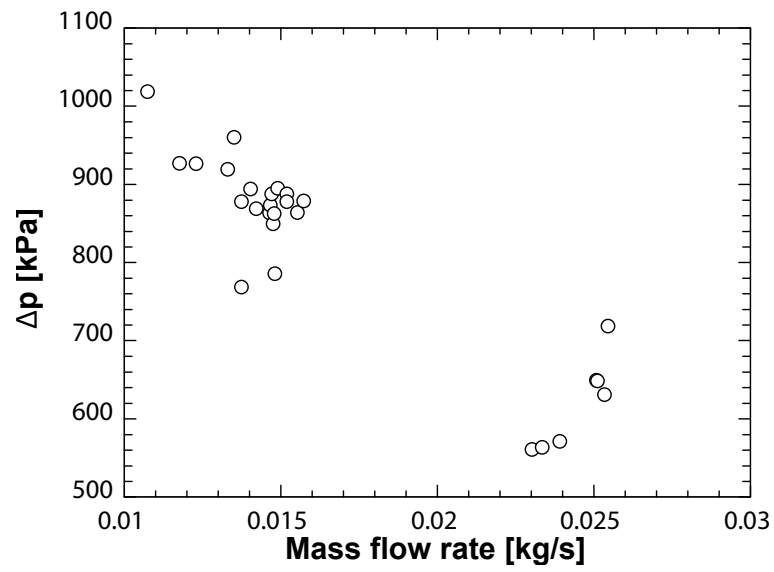


Figure 3.12: Inlet mass flow rate versus pressure difference

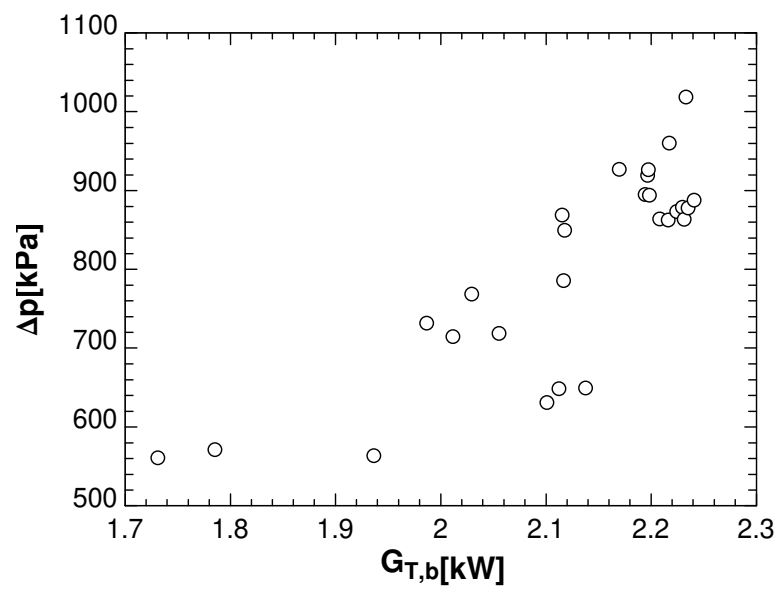


Figure 3.13: Received energy versus pressure difference



## CHAPTER 4

### RESULTS AND DISCUSSION

This chapter involves the results of the finite difference simulation and the thermodynamics simulation of the proposed design. The results are compared with the data collected from the experiments.

#### 4.1 Simulations of Finite Difference Method

A reference case is simulated using the input values in Table 1. Then tilting and inlet mass flow, operative temperatures, power input are changed in turn to investigate their effect on the overall behaviour of the generator. Its performance can be characterized through the definition of a few parameters Eq. 4.1 - 4.4. Relative vapor generation  $m_v R$  gives the yield of ammonia over the circulating solution mass flow. Collector efficiency  $\eta_c$  defined in Eq. 4.3 accounts for the effective power absorbed by the receiver tube, net of thermal losses to the ambient. Evaporation efficiency  $\eta_{ev}$  corresponds to the percentage of the net input power which contributes to phase change.  $\eta_{tot}$  estimates the evaporation efficiency with respect to solar power captured by the collector.

$$m_v R = \frac{\dot{m}_{v,out}}{\dot{m}_{v,in}} \quad (4.1)$$

$$\eta_{ev} = \sum_{j=1}^n \frac{\dot{m}_{vj} i_{lv}}{Q_{wj}} \quad (4.2)$$

$$\eta_c = \sum_{j=1}^n \frac{Q_{wj}}{Q_{sj}} \quad (4.3)$$

Table 4.1: Reference case inputs and intermediate results

Variable	Value	Variable	Value	Variable	Value
$\dot{m}_{l,in}$	$0.05 kg s^{-1}$	$\theta$	$25^\circ$	$\epsilon_t$	$4.5 \times 10^{-5}$
$T_c$	$308 K$	$I$	$800 W m^{-2}$	$p$	$13.5 \times 10^5 Pa$
$T_{ev}$	$278 K$	$c_1$	$0.3581 W m^{-2} K^{-1}$	$T_{l,n}$	$341 K$
$T_{amb}$	$298 K$	$c_2$	$0.0019 W m^{-2} K^{-2}$	$x_{in}$	$0.53$
$D$	$0.03 m$	$c_3$	$0.116 J m^{-3} K^{-1}$	$v_l$	$1.26 m s^{-1}$
$L_t$	$6.00 m$	$u$	$1 m s^{-1}$	$\alpha$	$0.94$
$L_a$	$2.30 m$	$\eta_o$	$0.71$	$Re$	$5.54 \times 10^3$

$$\eta_{tot} = \eta_{ev}\eta_c \quad (4.4)$$

#### 4.1.1 Effect of tube tilting and liquid mass flow rate

Tilt angle  $\theta$  is varied from  $5^\circ$  to  $45^\circ$ . Inlet liquid mass flow  $\dot{m}_{l,in}$  is varied as input from  $0.01 s^{-1}$  to  $0.50 kg s^{-1}$ . Their combined effect is considered. As expected, tilt angle affects liquid velocity but no appreciable effect has been noted on ammonia production  $\dot{m}_{v,out}$  and evaporation efficiency  $\eta_{ev}$ .



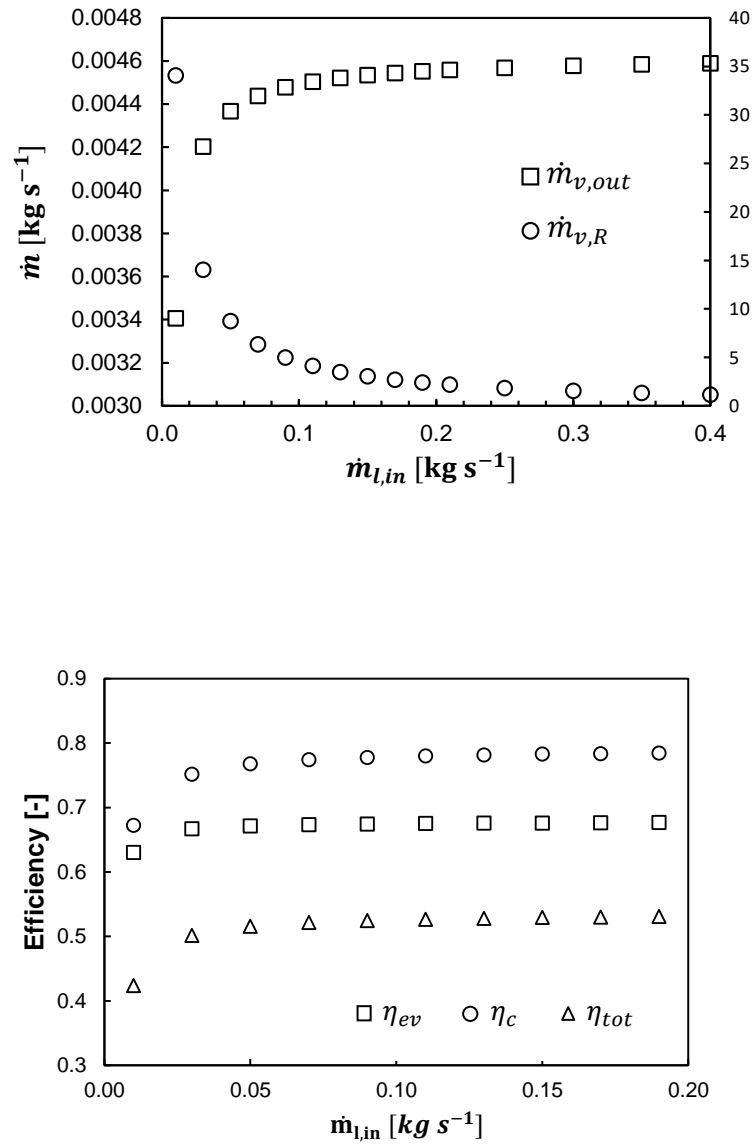


Figure 4.1: Effect of liquid mass flow rate on vapor ammonia generation mass flow rate and efficiencies

Higher liquid velocity and liquid Reynolds number correspond to higher wall-to-liquid heat transfer, which leads to slightly lower average  $T_w$  and reduced thermal losses, but their influence on global performances is not relevant in practical terms. This allows a great flexibility when applying the concept to different latitudes and

ceiling slant angles. On the other hand, mass flow influence is remarkable, as void fraction  $\alpha$  is affected. Fig. 4.1 shows the end effects. Temperature difference  $\Delta T_{l,t} = T_{l,out} - T_{l,in}$  decreases for high  $\dot{m}_{l,in}$ , since the amount of heated liquid grows and the related mass fraction reduction along the tube length  $\Delta x_t = x_{in} - x_{out}$  decreases coherently. Ammonia mass flow  $\dot{m}_{v,out}$  grows anyhow, even for reduced  $\Delta x_t$ , being in the first approximation  $\dot{m}_{v,out} = \Delta x_t \dot{m}_{l,in}$ . This trend is remarkable at low  $\dot{m}_{l,in}$  but it becomes almost flat for  $\dot{m}_{l,in} > 0.2 \text{ kg s}^{-1}$ , suggesting to not overcome such limit during the particular facility design and operation. Collector efficiency improves at growing  $\dot{m}_{l,in}$  due to a lower average  $T_w$ , which results from a lower average liquid temperature as well as from an increased wall-to-liquid heat transfer.

#### 4.1.2 Effect of operative temperatures

Condenser temperature  $T_c$  and evaporator temperature  $T_{ev}$  effect is scrutinized varying them in the ranges 298 °K to 318 °K and 268 °K to 283 °K, respectively. Other input parameters do not differ from the reference case. Both  $T_{l,in}$  and  $x_{in}$  versus  $T_c$  are reported for different  $T_{ev}$ : (a) 268 °K ;(b) 273 °K;(c) 279 °K;(d) 283 °K. Pressure increases with  $T_c$ ,  $T_{l,in}$  follows the same trend driven by the saturation constraints. For a given  $T_c$  liquid temperature is higher for low  $T_{ev}$  since inlet mass fraction is also reduced (Fig. 4.2 and Fig. 4.3).

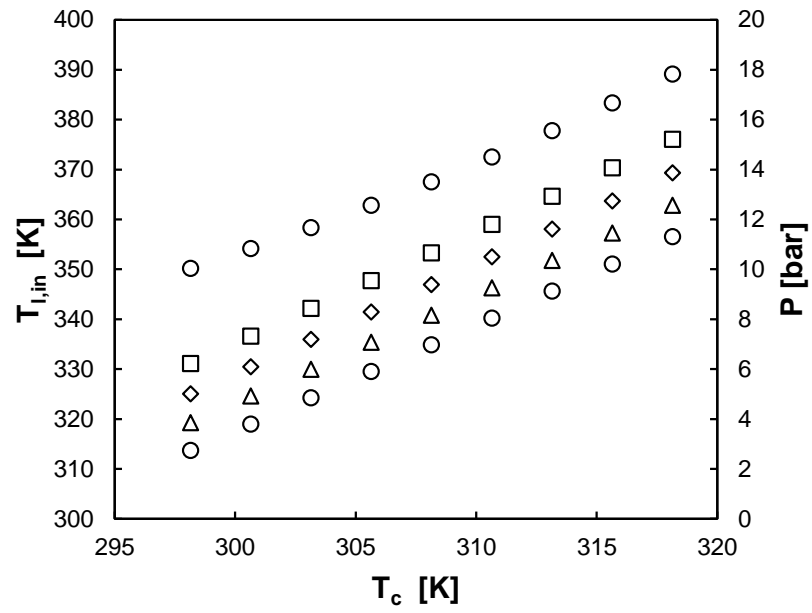


Figure 4.2: Pressure and Inlet liquid temperature

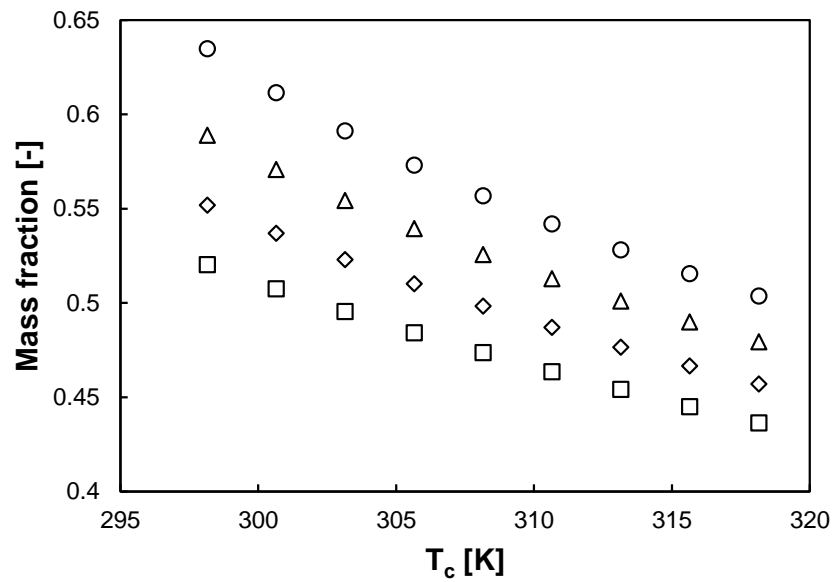


Figure 4.3: Change of mass fraction with condenser temperature

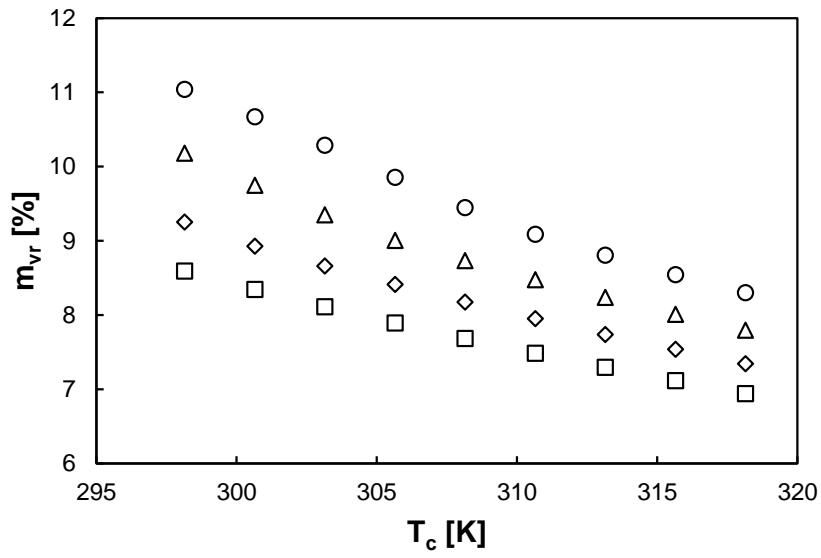


Figure 4.4: Change of mass flow rate of ammonia vapor with temperature

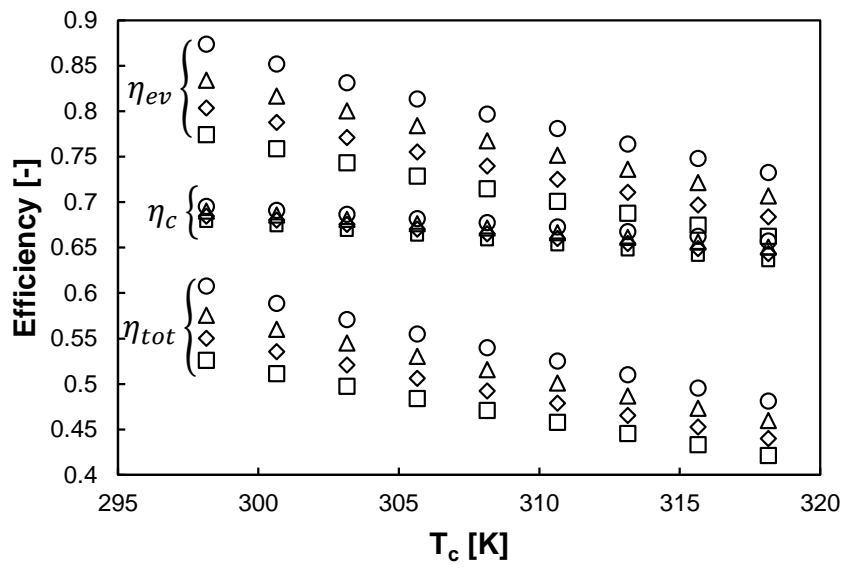


Figure 4.5: Change of vapor efficiencies with temperature

Operative temperature has a considerable effect on the vapor ammonia generation as reported in Fig.4.4 and Fig. 4.5. The relative value of  $m_{vR}$  varies from 7% up to

11% only changing  $T_{ev}$  and  $T_c$  within the considered ranges. On one hand, optimal generator performances correspond to low  $T_c$ , hence lower pressure and inlet liquid temperature. On the other hand, higher  $T_{ev}$  and higher inlet mass fraction  $x_{in}$  are also favourable. This behaviour is confirmed by an efficiency analysis. Evaporation efficiency  $\eta_{ev}$  is coherent with the hypothesis of saturation thus strictly depends on the saturation temperature slope with respect to mass fraction  $\partial T_s / \partial x$ . Operating at higher mass fraction  $x$  reduces  $\partial T_s / \partial x$  allowing the phase change process to take place with relatively smaller temperature changes.  $\eta_c$  decreases for higher wall temperature and hence for higher inlet liquid temperature, following a similar trend.

#### 4.1.3 Effect of solar radiation and collector aperture

Solar radiation  $I$  is varied from 400 to 1000  $Wm^{-2}$  over three different collector aperture  $L_a$  :1.3 m, 2.3 m and 3.3 m, corresponding to collectors (a),(b),and (c), respectively.  $m_{vR}$  relative ammonia mass flow grows linearly with the product  $L_a I$ , going from the minimum of 2% for the smallest value at up to 16% for the largest collector (c) at maximum radiation level. On the other hand, efficiency figures of merit change in a very moderate amount, as Figure 4.7 shows.

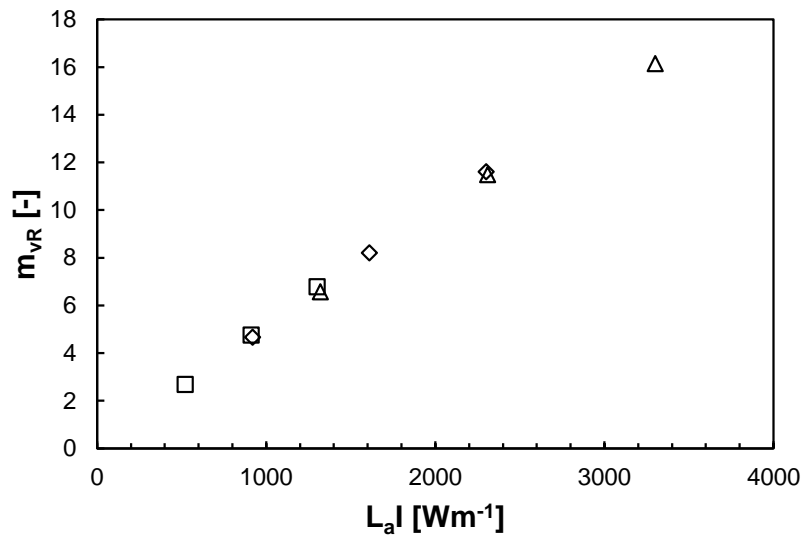


Figure 4.6: Joint effect of solar radiation and collector aperture on ammonia vapor generation percentage

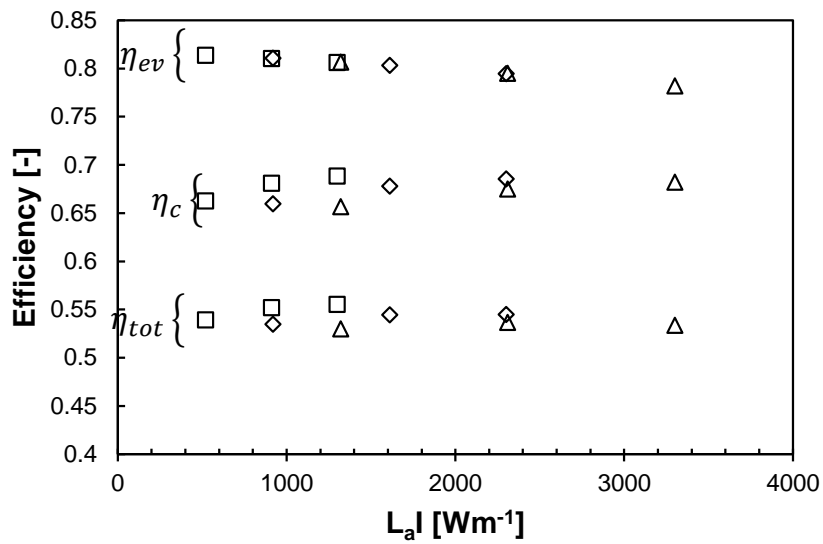


Figure 4.7: Joint effect of solar radiation and collector aperture on ammonia efficiencies

## 4.2 Thermodynamics simulations of the cycle

The simulation runs are oriented to calculate the quasi-steady time evolution of the machine cooling  $COP$ , the cooling power  $Q_e$  and the length of the subcooled zone in the desorber tube  $L_{sub}$ . The cycle is cooling down a water stream of 4 °C inlet constant temperature with a flow rate of  $0.6\text{kg s}^{-1}$ . The representative days are clear days with an average of  $1\text{m/s}$  wind speed. The standard climate values [89] are summarized in Tab. 2. Sunrise and sunset times are the local times. The irradiance is measured for a E-W tracking with 40 ° constant inclined surface. The irradiation values are plotted in Fig. 7 which the x-axis demonstrates the hour of the day.

Table 4.2: Standard climate values of the representative days

	Sunrise	Sunset	Temp. [°C]		Irrad. [ $\text{kW m}^{-2}$ ]			Insol. [ $\text{kJ m}^{-2}$ ]
			Min	Max	Min	Max	Ave	
January	8:50	17:50	5	10	0.10	0.87	0.69	6.09
April	8:20	20:30	11	18	0.10	1.00	0.84	10.09
July	7:40	21:30	22	32	0.10	0.89	0.74	10.13
October	9:10	19:10	14	20	0.10	0.97	0.81	7.90

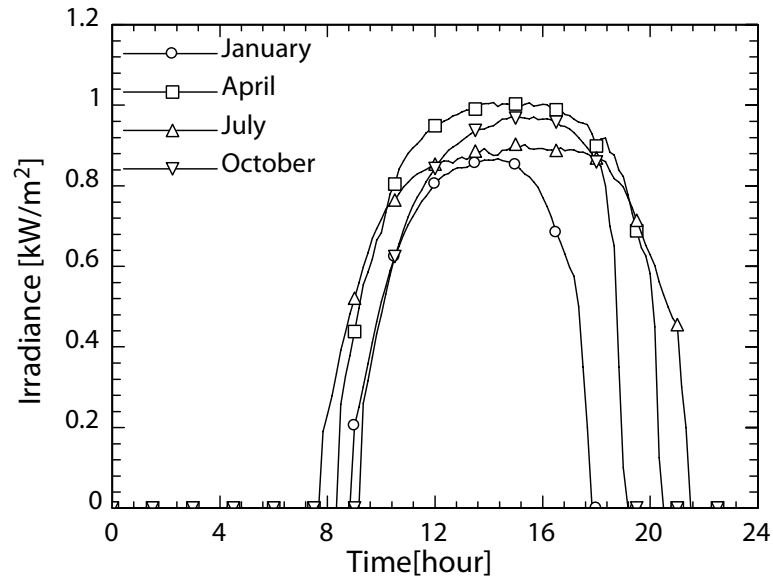


Figure 4.8: Daily solar power of the representative days

There are four different days representing four different months with two different mass flow rates conditions through the pump of the cycle. Fig. 4.9 and Fig. 4.10 show the COP and cooling power  $Q_e$  of the cycle for each 10 minutes of the day. The time axes of the plots span between sunrise and sunset which are represented by 0 and 1 respectively. Similarly, 0.5 stands for the solar noon. The plots show that the highest efficiencies are observed in January whereas the highest cooling power is in April. The average COPs and cooling power as well as total cooling energy are summarized in Tab. 3. The average values are calculated from sunrise to sunset.

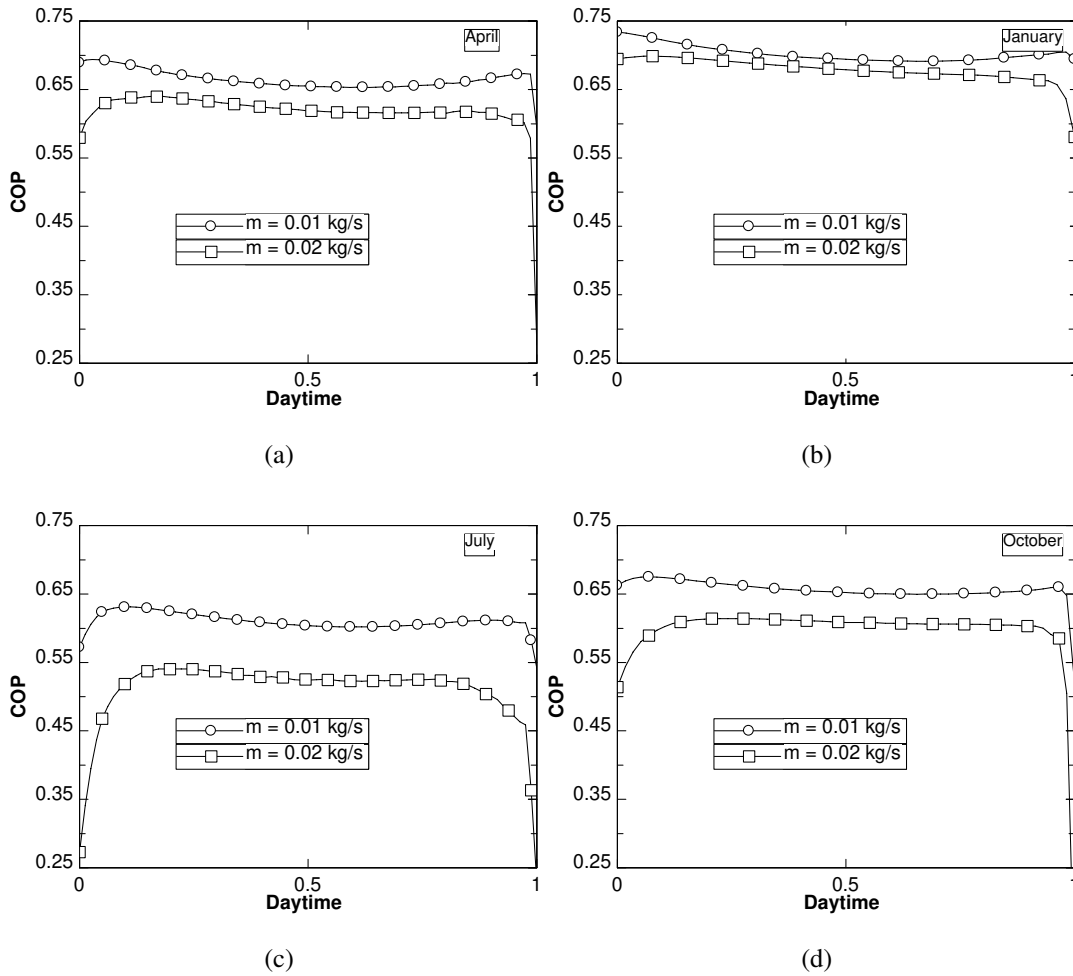


Figure 4.9: Time evolution of refrigeration along the representative days of each month

The solar integrated cycle reveals that it yields a higher COP and cooling power with the lower mass flow rate of the two ones considered. On the other hand, in terms of



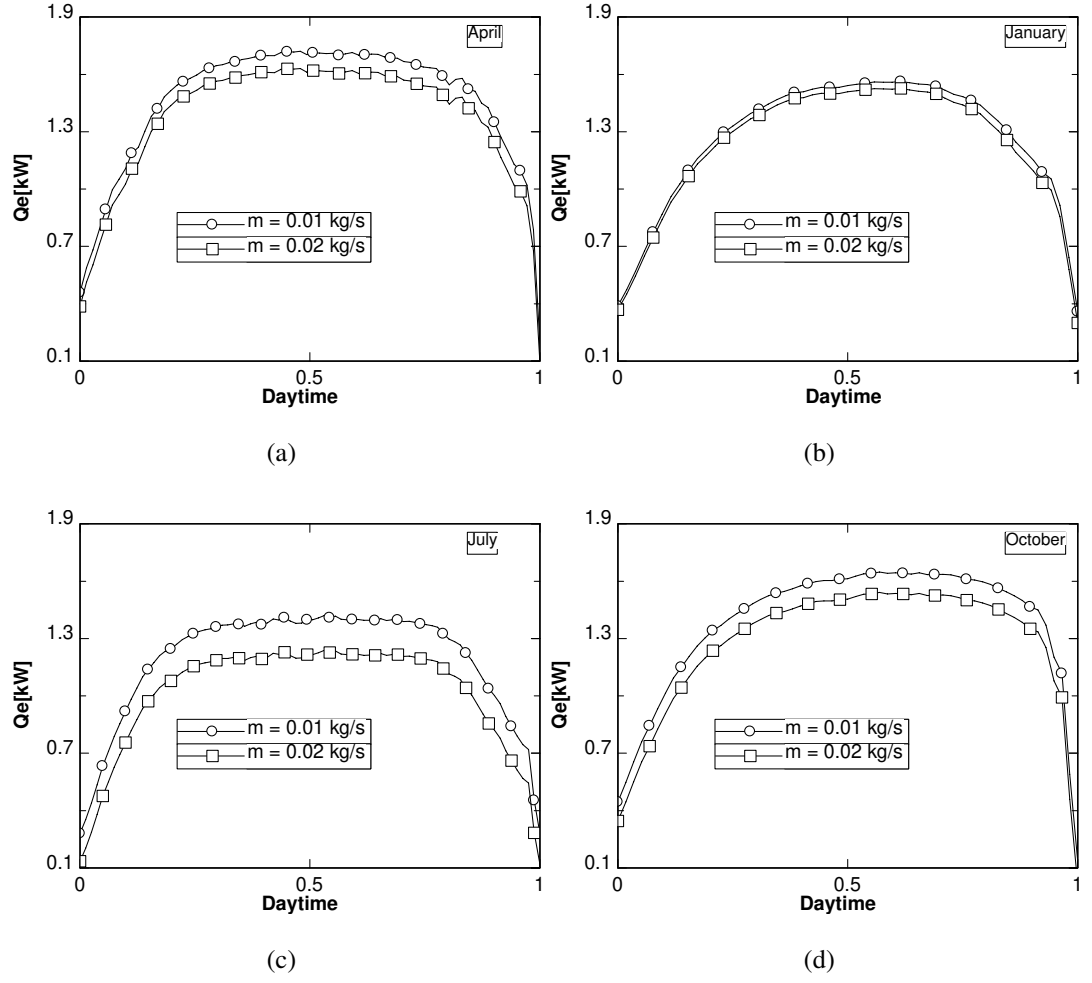


Figure 4.10: Time evolution of cooling power along the representative days of each month

Table 4.3: Average COP, cooling power and total cooling energy

	$\dot{m} [kg s^{-1}]$	January	April	July	October
Ave. COP	0.01	0.702	0.665	0.610	0.658
	0.02	0.678	0.617	0.508	0.595
Ave. cooling power [kW]	0.01	1.263	1.457	1.182	1.424
	0.02	1.226	1.366	1.007	1.239
Total cooling energy [kWh]	0.01	11.16	17.48	16.15	12.89
	0.02	10.78	16.36	13.74	13.11

COP, the cycle performs better in January than the rest of the months. The reason is that the ambient temperature is relatively lower and hence the high pressure of the cycle is moderated by the lower ambient temperatures. That makes the separation of the refrigerant easier. Also it is worth mentioning that the representative day in January (and each of the others too) is a clear day. Besides, performing the highest COP, it has a good average daily cooling power of more than 1.2 kW. The total heat extracted from the cooling water stream in a whole day has the lowest value despite the high and cooling power due to the fact that the day time is lower than the rest of the months studied here. The total cooling energy is calculated by integrating data in Fig. 4.10 along time. The day in April yields also high values compared to the other months and yields the highest cooling power and total energy values. The reason is that the ambient temperatures are still not at the highest levels as in July and the incidence angle to the PTC has the minimum value during this month. The solar panel is east-west tracking but has constant tilt angle of  $40^\circ$  and located in Madrid at a latitude of  $40.33^\circ$ . The cycle performs the worst values in the July day when the ambient temperatures are the highest and the incidence angle is already high even though there is the highest incoming insolation. The total energy value is fairly good enough thanks to the longer day time in the northern hemisphere. Lastly, the cycle seems to produce fairly good results in October too.

The length where the solution is subcooled,  $L_{sub}$ , is plotted in Fig. 4.11. With a higher mass flow rate, it is more likely to have a subcooled zone in the tube. Also, near sunrises and sunsets where irradiance is minimum, the length of the subcooled zone is performing its maximum. In January, due to low internal pressure values, the solution inlet is almost always saturated. In April and October for a mass flow rate of  $0.02 \text{ kg s}^{-1}$ , the subcooled length is observed to have nonzero values at low irradiance period, yet for the lower mass flow rate it is zero all the time of the day. In July, the subcooled length is calculated to be zero for both flow rates, yet only for the higher flow rate the length is around 0.25 m except near sunrise and sunset. All in all, apart from sunrise and sunset times, the subcooled length is usually very short. In other words, the solution reaches saturation temperature immediately after entering the desorber tube.

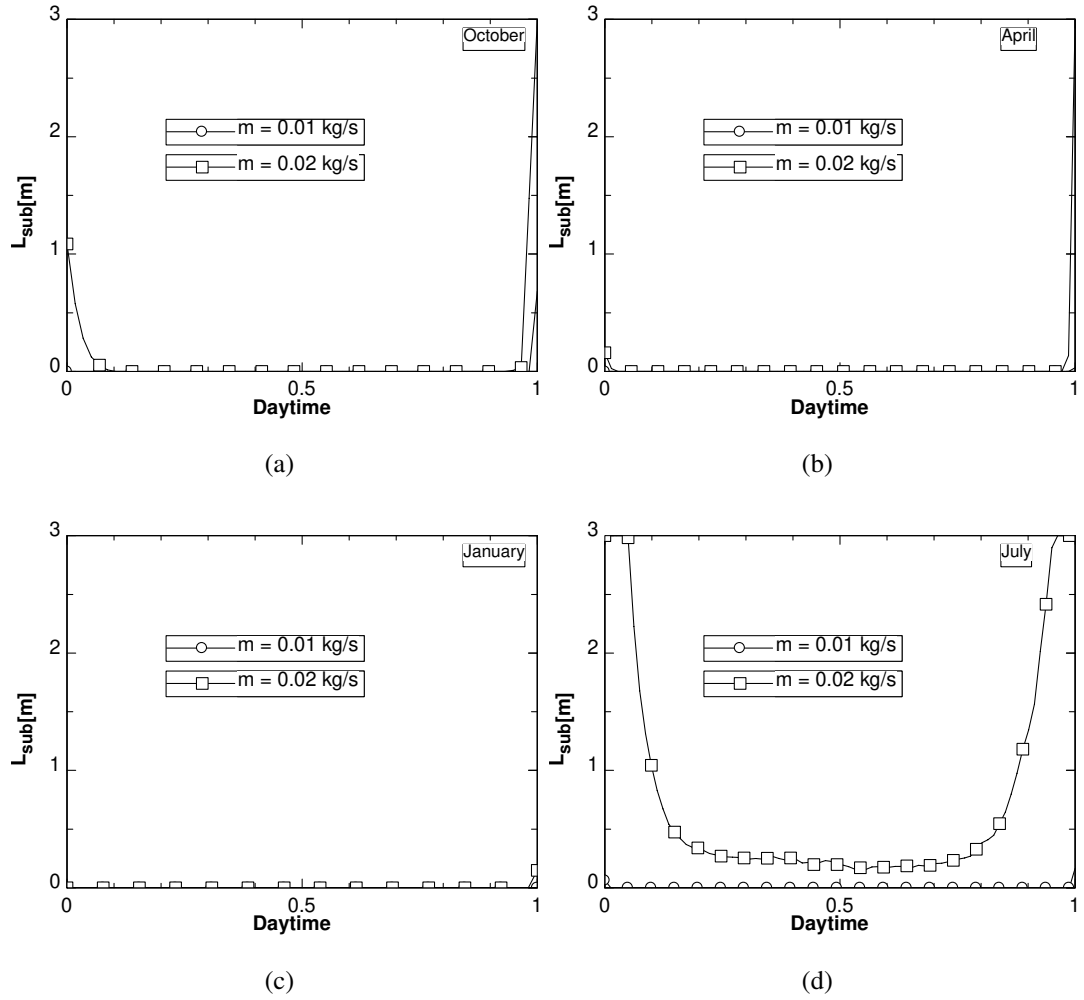


Figure 4.11: Time evolution of subcooled zone length along the representative days of each month

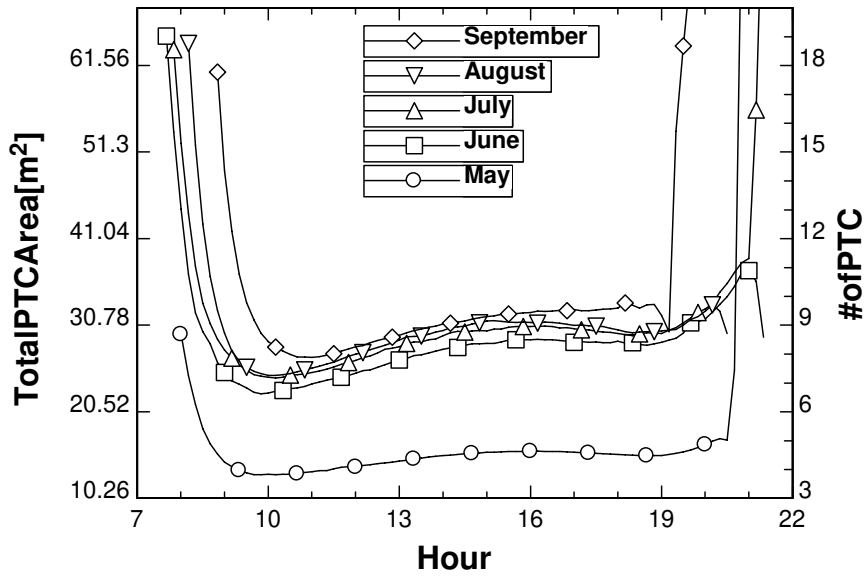


Figure 4.12: Required PTC area

#### 4.3 Thermodynamic simulation of a representative building

The set of thermodynamic equations are solved iteratively. The aim is to calculate to evaluate the minimum number of the PTCs to supply enough cooling power to the model flat. Moreover, the cooling COP of the cycle has been calculated and finally the effectiveness of the proposed desorber design has been evaluated. Each calculation has repeated for five different months. The required PTC area has been plotted in Fig. 4.12.

Slightly more than  $30m^2$  of PTC area is reasonable in order to maintain the comfort temperature in an apartment which has  $30m^2$  living area for a duration from 10am to 8pm. That area corresponds to 9 to 10 PTCs of the type that is assumed in the study. It is worth to note that the number of PTCs is fairly constant along the day, thus not requiring much heat or cold storage. Note that this number drops to 5 PTCs for May when the solar incidence angle is minimum for a  $40^\circ$  tilted surface and cooling load is relatively lower as illustrated in Fig. 2.9 and Fig. 2.10.

Besides, the cooling COP of the cycle is calculated hourly for each month. It is

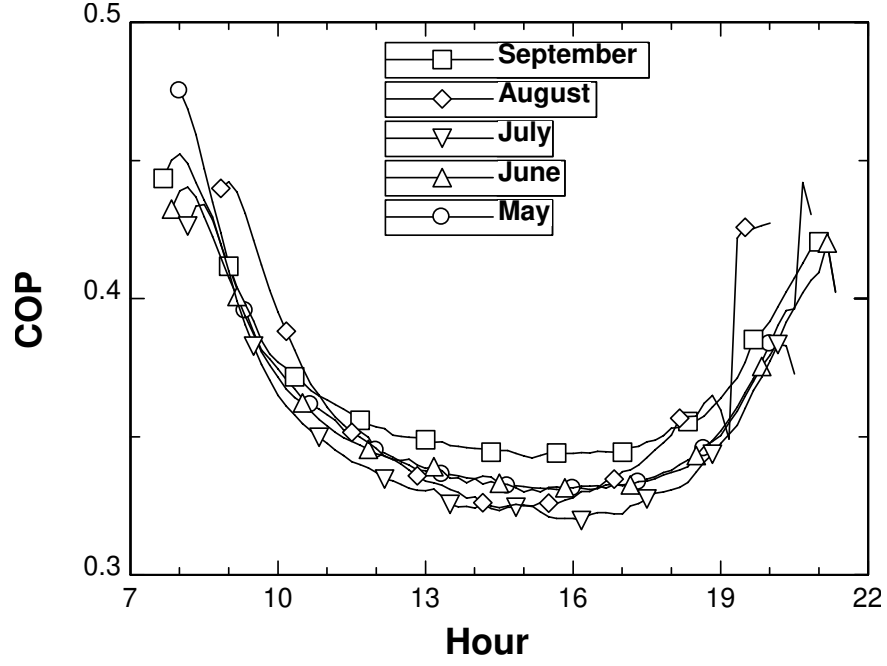


Figure 4.13: Variation of COP during daytime

defined as the ratio of the cooling power created and the total power input.

$$COP = \frac{\dot{Q}_e}{n\dot{G}_{t,b}w_aL_a + W_{pump}} \quad (4.5)$$

where  $\dot{Q}_e$  is the cooling power created;  $n$ ,  $\dot{G}_{t,b}$ ,  $W_a$ ,  $L_a$ , and  $W_{pump}$  are the number of PTCs, the beam solar irradiance for 40 °tilted surface with E-W tracking, aperture width, aperture length, and the power supplied by the solution pump respectively. The hourly variation of COP is presented in Fig. 4.13.

Finally, it is required to examine how well functioning the replacement of the classical desorber heat exchanger. One method, in order to achieve that, can be calculating the ratio of the power introduced to the circulating fluid to the total heat input from the solar resource, which is called effectiveness.

$$\epsilon = \frac{\dot{Q}}{\dot{Q}_{max}} = \frac{\dot{Q}_d}{n\dot{G}_{t,b}W_aL_a} \quad (4.6)$$

Which is, in other words, the ratio of the energy introduced to the running fluid and

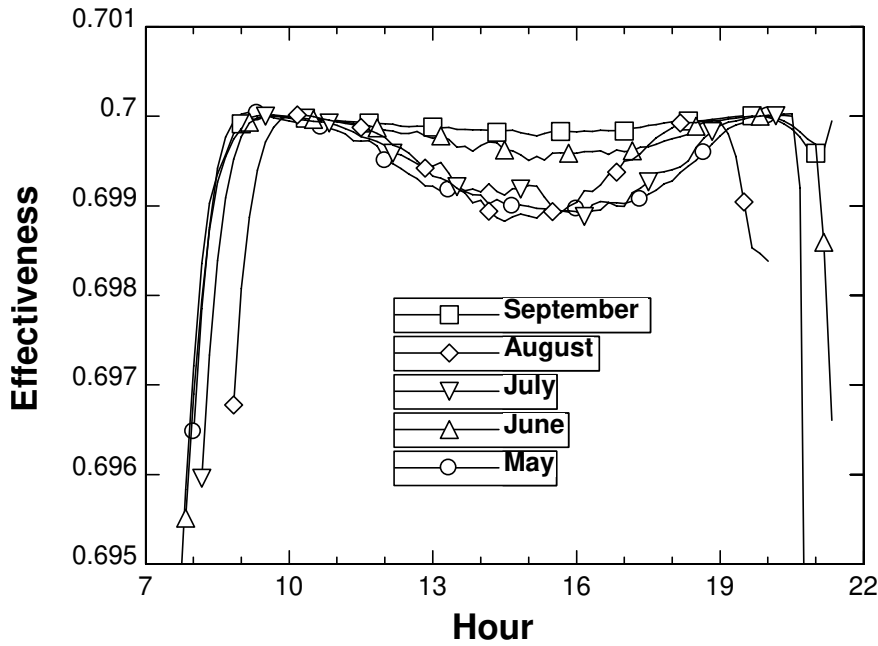


Figure 4.14: Variation of Effectiveness during daytime

the possible theoretical amount that could be introduced in. The hourly distribution of effectiveness is plotted in Fig. 4.14. It varies around 0.7.

The study is aimed to compare and contrast the proposed design [64, 58, 65] with conventional ones in the literature. Some of the analogues work have been reviewed. In 2008, Mazloumi et.al. ran a simulation of a single effect absorption cycle with  $LiBr - H_2O$  as running fluid [90]. They have used a PTC combined with a storage tank. They evaluated the minimum required area of PTC and storage tank volume in order to meet an average house's cooling demand in Ahwaz, Iran. They assumed a maximum of 17.5kW of cooling load and an evaporation temperature of 6 °C. Yet, it is not mentioned explicitly how the cooling load is determined. On the other hand, they have used the measured meteorological data as an input to their simulation. Their design differs from the current one by using different solution for absorption cycle and having a storage tank, however, both simulations solve single effect absorption cycle with akin input parameters. Mazloumi et.al. calculated 60  $m^2$  collector area is to supply cooling demand of an ordinary house in their climate. They have reported a range of COP that their design worked in from 0.67 to 0.76. The next simulation results are from Athens, Greece by Tzivanidis et. al. [91]. Their simulation, like Mazloumi et.

al., solves for a single-effect absorption cycle using  $LiBr - H_2O$  with a combination of PTC and storage tank. However, they mention about combining PTCs in parallel and their meteorological data is calculated using the software TRNSYS. They have estimated the maximum cooling load of a  $25\text{ m}^2$  room would be 3 kW. Assuming a linear relation, they concluded that the maximum cooling load of a  $100\text{ m}^2$  apartment would be 12 kW. Their results showed that the required number of PTC to cool down a  $100\text{ m}^2$  apartment to be 4. Note that their PTC have an area of  $14\text{ m}^2$ , so that in total that sums up to  $56\text{ m}^2$  PTC area. The produced total cooling energy they have calculated is 150 kWh for a 12.5 h period in July. They have assumed an ambient temperature dependent COP taken from literature which mainly varies between 0.6 and 0.8. These case studies have some more input and output parameters due to their specific designs like the mass flow rates of PTC and desorber separately, and the volume of the storage tank. We have mentioned about the comparable design parameters only. Şahin et.al. [87] have investigated the required total PTC area as  $50\text{ m}^2$  for the same sample flat studied in this work which is located in a Mediterranean city of southern Turkey. They simulated a single effect absorption cycle running water-ammonium with a classical desorber heat exchanger. Their design doesn't have a storage tank, but the heat transfer fluid is heated in PTC and the energy is transferred using a heat exchanger (desorber) to the absorption cycle. They have reported COP between 0.4 and 0.5 and desorber effectiveness of 0.75. In the current study an enhanced version of absorption cycle has been simulated for similar conditions to those mentioned. The total PTC area that is adequate for cooling has been calculated to be  $30\text{ m}^2$  for a  $30\text{ m}^2$  flat. The cooling COP of the suggested design varies between 0.30 and 0.45. On the other hand, the suggested desorber design resulted in slightly lower than 0.7 of efficiency on average.

The current design is compared to some other similar studies in the literature. Tab. 4.4 demonstrates the summary of the comparison. All of the reference studies are simulating single effect absorption cycle using PTC. They have similar condensation temperatures varying between  $6^\circ$  and  $10^\circ$ . There are two main differences. The first one is the solutions and the locations of the cities which are in Iran, Greece, Turkey and finally the current study is in Spain. All of the studies assumed their local weather data with a representative space of various cooling demand. The second difference

Table 4.4: Summary of the comparison

	Cycle	Solution	COP	$A_{room}/A_{col}$	$\dot{Q}_{e,max}/A_{col}$
Mazloumi et al.	SE Abs.	$H_2O/LiBr$	0.67-0.76	2.00	$0.29 \text{ kW/m}^2$
Tzivanidis et al.	SE Abs.	$H_2O/LiBr$	0.60-0.80	1.79	$0.12 \text{ kW/m}^2$
Şahin, et al.	SE Abs.	$NH_3/H_2O$	0.40-0.50	0.60	$0.20 \text{ kW/m}^2$
Current design	SE Abs.	$NH_3/LiNO_3$	0.30-0.45	2.00-1.00	$0.34 \text{ kW/m}^2$

is the solution pairs. Due to the different chemical properties of the solutions the cycles are not expected to work in the same COP range. It has been shown that  $LiBr - H_2O$  would have higher COP values than  $NH_3 - H_2O$  and  $NH_3 - LiNO_3$  [92]. On the other hand, the goal is to determine the minimum PTC area for human comfort which involves more parameters beside COP and becomes more complicated to achieve. As a comparison parameter, the air-conditioned area ( $A_{room}$ ) is divided by the minimum required collector area ( $A_{col}$ ). This parameter lays on the assumption that the heights of the spaces are identical. Higher value of the area ratio is preferred due to a reduced footprint of the collectors. The proposed design requires half of the room for May and for the summer period collector area is equal to flats base area. The ratios of the references fall in to the range of 0.60 to 2.00. The last parameter observed is the generated maximum cooling power. Yet, due to various input parameters of the reference studies, it is better to normalize the maximum cooling power with the collector area. That would give the maximum cooling power per collector area. The current design resulted in a better performance in that parameter by  $0.34 \text{ kW/m}^2$ .

#### 4.4 Experimental results of the proposed generator/seperator

A theoretical analysis of an innovative solar direct vapor generator/seperator proposed herewith has been carried out. The steady-state 1D numerical finite differences model developed results of great help to evaluate the PTC performances as partially filled vapor generator through the simulation of the two-phase stratified flow and heat transfer inside the receiver tube, adopting a simplified approach coherent with the objective of the present work. Results confirm the suitability of small-scale PTCs for the proposed



scope and validate the concept of direct vapor generation through stratified counter-current two-phase flow. The influence of main design and operative parameters has been scrutinized. Tilt angle resulted irrelevant on generator performances, identifying a paramount advantage for installation on roofs and sloped terrains. The solar radiance and collector aperture have been confirmed as determinant parameters. Operative parameters, like solution mass flow rate as well as condenser and evaporator temperatures have shown a non-negligible effect on ammonia generation capacity and efficiency. Quantitative evaluation of solar collector performances has been provided in a comprehensive operative range thanks to the reasonable simplifying assumptions and the semi-empirical formulation of boiling phenomena by referred authors. A single-effect absorption cycle has been integrated with a parabolic trough collector drawing inside it the inner working solution of the absorption machine. That avoids the HTF and an extra heat exchanger. Also using the solution pair  $NH_3 - LiNO_3$ , the solution rectifier that is necessary for the  $NH_3/H_2O$  pair is avoided too. All of those results in an absorption machine with a smaller footprint, lower in price and simpler in design. Besides, that it is placed outdoors makes it safer to use and benefits of not occupying space inside the buildings. The thermodynamic simulation of the absorption machine integrated with the solar collector is performed in order to anticipate the behavior of the proposed design. The simulations are done along four representative days of the four seasons in Madrid, Spain. The PTC is set to be east-west tracking with a constant tilt angle, year-round optimum in this location. The properties of the PTC are taken from a real one and the irradiance and temperature values are measured in Madrid, Spain for clear days. The cycle is set to cool down 4 °C inlet water stream with a  $0.6 \text{ kg s}^{-1}$  mass flow rate. The results reveal the cooling and cooling power of the absorption machine along the day. A maximum of  $0.42 \text{ kW m}^{-2}$  of average cooling power has been reached. Also the subcooled length of the desorber tube has been calculated which has a vital role in the performance of the proposed solar integrated cycle. Results show that this length is small for the application data, thus supporting the viability of the technology proposed. An application of the system for a studio flat has revealed that the base area of a studio flat is sufficient to implement solar panels of PTC type to respond to the cooling need for human comfort. On the other hand, the experimental data has shown that the subcooled zone in the receiver tube has no simple correlation with heat input and collector effectiveness. However, the length

has a clear dependency on the desorption rate of the design. Note that the desorption rate is linear with the saturation temperature and/or with the pressure difference. Increasing pressure difference or higher saturation temperatures results in higher desorption rate. In other words, lower subcooled length causes higher desorption rates. The simulation results for the calculation of the effect of the inclination angle of the PTC has shown that the angle has no significant effect on the refrigerant generation. In the experiments that have been performed at 20° 40° and 45° verified that there is no variation of the performance of the system. However, on the other hand, This phenomenon shouldn't create a confusion that the variation of the inclination angle changes the incidence angle and affects the heat input to the system. Varying heat input has an effect on the performance of generation of refrigerant. The finite difference simulation of the receiver tube as a desorber resulted in a separation rate varying from 2% to 16% as shown earlier. The simulation has run for different lengths of PTC with a constant width. In the experiment, the length of the PTC is 3 meters with a 3,42  $m^2$  aperture area. The corresponding simulation results have been plotted together with the experiments. The experimental data for the separation rate changes between 1% to 4%. Both results have been demonstrated in Fig. 4.15.

In the simulation of the cycle [58] the length of the subcooled zone is demonstrated as a function of the hour of the day. In order to compare with the experimental data the proper representation of the dependency should be a plot of Irradiance vs Length. The plot has been regenerated and compared with the experimental results in Fig. 4.16.

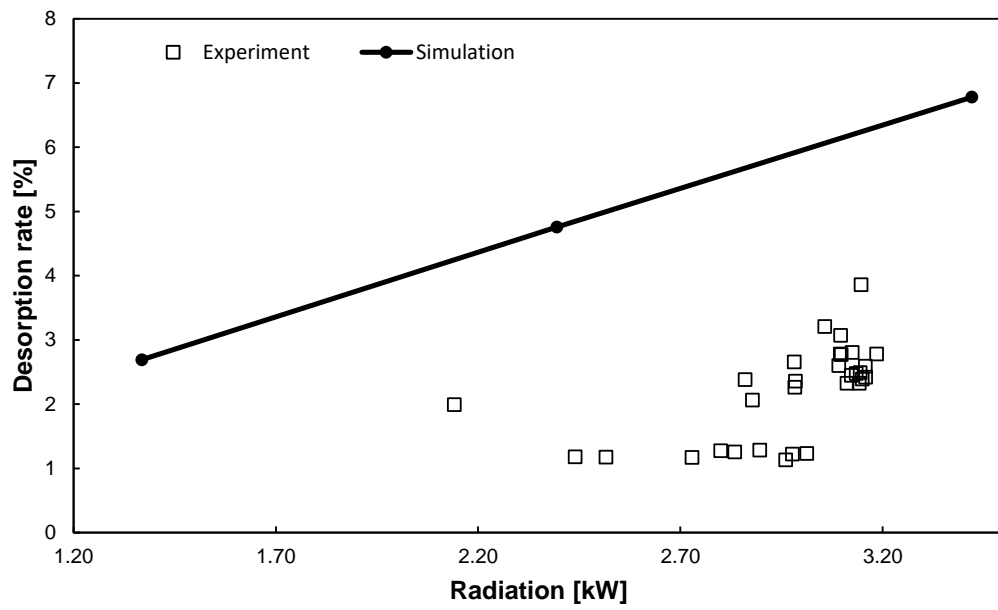


Figure 4.15: Desorption rate comparison with experiment

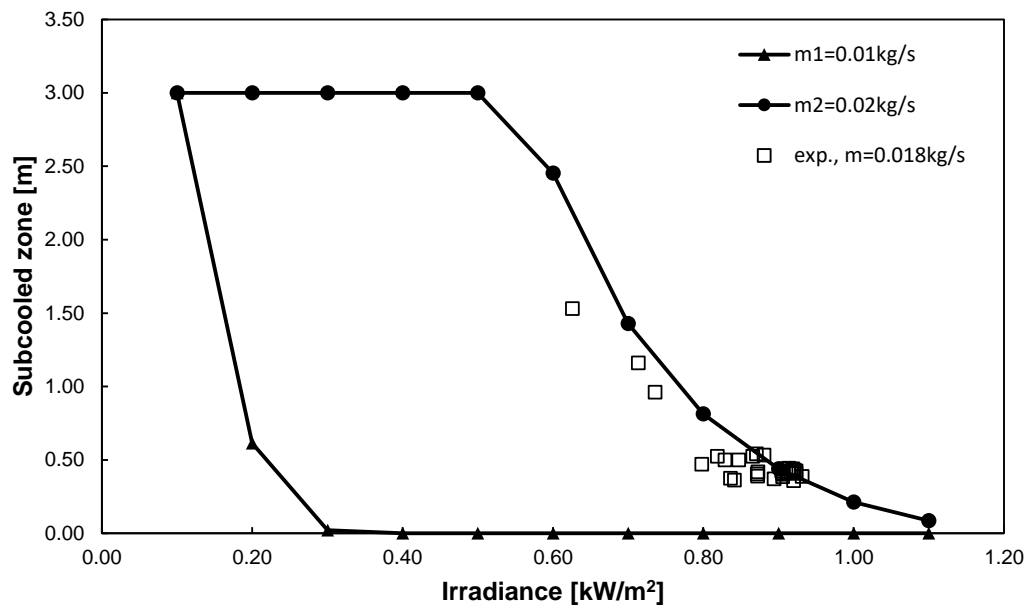


Figure 4.16: Variation of subcooled zone with irradiance

In the study of the simulation of the studio flat it has been calculated that the effectiveness of the desorber tube is constant at 0.7 during the day. The experiment has shown that the effectiveness of the desorber tube is slightly less than this value. It varies around 0.65 as demonstrated in Fig. 4.17.

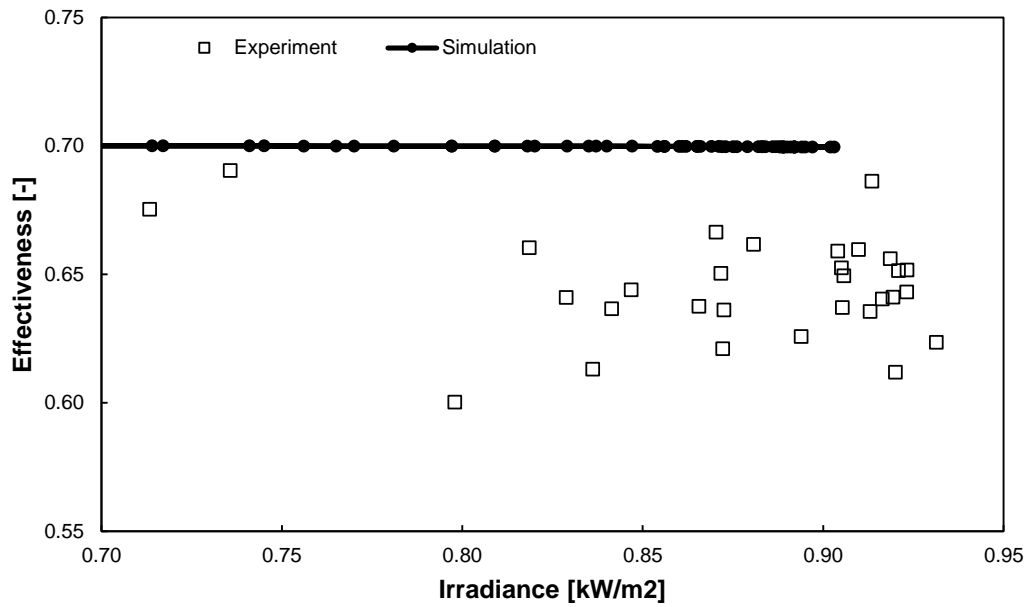


Figure 4.17: Variation of Effectiveness with irradiance

## CHAPTER 5

### CONCLUSION

Energy security is an utmost importance issue for all the countries. Beside supplying the demand from local sources, in other words being independent from others, it is better to get advantage from natural sources like solar energy, wind power, geothermal energy etc. Also note that this would be completed by being energy efficient. Consumption of energy should be diminished in a way that the economy is not effected. One of the solutions of the problem is building energy efficient buildings and reduce the required energy power. However, one supposed to know how efficient a building is at which locations on the earth. For that reason there are several standards globally. One can name some common ones as Passive House, LEED and BREEAM. The cooling load of a building in the standards of for example Passive House supposed to be less than  $10W/m^2$ . The experimental results, in this study, shows that the total cooling power of the proposed design is  $5.77W/m^2$ . This value corresponds to 58% of the required total value. It is not able to satisfied the cooling demand completely. On the other hand, the standard requires a renewable energy generation of  $60kWh/(m^2a)$ . The current designs satisfies  $14kWh/(m^2a)$  where it corresponds to 23% of the required amount. The absorption cooling machine with the improvement suggested can be an important part of an energy efficient building. In the case of industrial applications, it should be considered as an auxiliary system to the classical cooling equipment.

The refrigeration technology in the commonly used form that is called vapor compression cycle. However, there are many others like absorption cooling. Absorption cooling cycle, with a very basic definition, replaces the pump the refrigeration cycle with a chemical pump. One of the advantages of it is that it is compatible with solar

energy. Researchers are working on the improvements of the technology as in this study it has been boosted with replacing the desorber which is a heat exchanger with the solar collector tube of a parabolic trough collector. The improvement has brought some advantage over the conventional design. To name the advantages cooling power per collector area has been observed. It has showed a great improvement over conventional cycles at similar working conditions with a maximum cooling power per collector area of  $0.34 \text{ kW/m}^2$  while the others varied between  $0.12 \text{ kW/m}^2$  and  $0.29 \text{ kW/m}^2$ .

The proposed design introduces other advantages. First of all, the number of components in the systems decreases. Conventional design requires an extra pump, heat exchanger and requires heat transfer fluid with an extended length of tubing. Those are directly influencing the footprint. Buildings have limited space for such equipment and reduced sizes are always welcomed. Also note that less equipment results in cheaper machines. The costs of the proposed absorption machine is expected to be less. Note that the footprint and the cost are the main obstacles in front of the absorption cooling technology. On top of this, avoiding the usage of storage tanks simplifies and decreases the cost of the system even more.

The selection of the solution pair is of great importance as well.  $\text{NH}_3/\text{LiNO}_3$  do not require a rectifier due to the fact that  $\text{LiNO}_3$  is not evaporating and crystallization is hardly observed for working condition of an absorption machine [92] [93]. On the other hand,  $\text{NH}_3$  should be handled carefully due to its hazard on human health [94], yet it is a compound that is found in nature and has zero global warming potential (GWP) and ozone depletion potential (ODP) [95]. The evaluated properties from the simulations with real meteorological data and the comparison of similar studies reveal the potential and competitiveness of the current design.

To sum up, the study is proposing a boosted design for solar absorption cooling cycle that can be implemented in energy efficient buildings. Its properties has been studied numerically and theoretically. The results of both have been compared and also they have been compared and contrasted to the conventional designs. It is observed that the usage of the absorption cycle assist energy efficient building catch local and international standards. On the other hand, it is open to research and there is more work

to increase the performance of the technology. To name some of them:

- The proposed design should be tested with half-effect, double-effect series, double-effect reverse and triple-effect configurations.
- The solution pairs would change the characteristics of the design. The  $H_2O - NH_3$  and  $LiBr - H_2O$  solutions have well studied properties and commonly used pairs. One should test the performance with those different solution pairs. As an extension of those, instead of a pair the usage of a triple solutions would be interesting to test with the proposed design.
- It is reported that a good improvement is to replace the classical absorber with an ejector and design an innovative adiabatic absorber [96]. The combined effect with the ejector seems to be a promising improvement.
- It would be a good practice to study the performance of heating beside refrigerating using absorption cycle. Due to the fact that one may not need refrigeration but heating and it would be better using it for other purposes instead of leaving it abandoned. Also note that one may not require refrigeration neither heating but electricity. Hence, using the system for cooling, heating and electricity generation in the same machine would be a handy way of using the technology.





## REFERENCES

- [1] Y. Wang, J. Kuckelkorn, F.-Y. Zhao, S. Hartmut, and W. Lang, “A state of art of review on interactions between energy performance and indoor environment quality in passive house buildings,” *Renewable and Sustainable Energy Reviews*, 11 2016.
- [2] X. Cao, X. Dai, and J. Liu, “Building energy-consumption status worldwide and the state-of-the-art technologies for zero-energy buildings during the past decade,” *Energy and Buildings*, vol. 128, pp. 198 – 213, 2016.
- [3] W. Feist, J. Schnieders, V. Dorer, and A. Haas, “Re-inventing air heating: Convenient and comfortable within the frame of the passive house concept,” *Energy and Buildings*, vol. 37, no. 11, pp. 1186 – 1203, 2005. Research That Inspires 125 Years of EMPA.
- [4] J. Zhu and B. Chen, “Simplified analysis methods for thermal responsive performance of passive solar house in cold area of china,” *Energy and Buildings*, vol. 67, pp. 445 – 452, 2013.
- [5] J. Schnieders, W. Feist, and L. Rongen, “Passive houses for different climate zones,” *Energy and Buildings*, vol. 105, 07 2015.
- [6] M.-I. Mihai, V. Tanasiev, C. Dinca, A. Badea, and R. Vidu, “Passive house analysis in terms of energy performance,” *Energy and Buildings*, vol. 144, pp. 74–86, 05 2017.
- [7] L. Wang, J. Gwilliam, and P. Jones, “Case study of zero energy house design in uk,” *Energy and Buildings*, vol. 41, no. 11, pp. 1215 – 1222, 2009.
- [8] H. Truong and A. M. Garvie, “Chifley passive house: A case study in energy efficiency and comfort,” *Energy Procedia*, vol. 121, pp. 214 – 221, 2017. Improving Residential Energy Efficiency International Conference, IREE 2017.

- [9] P. H. Institute, “Criteria for the passive house, enerphit and phi low energy building standard,” Aug 2016. [Online; accessed 15-March-2020].
- [10] G. Mustafaraj, G. Lowry, and J. Chen, “Prediction of room temperature and relative humidity by autoregressive linear and nonlinear neural network models for an open office,” *Energy and Buildings*, vol. 43, no. 6, pp. 1452 – 1460, 2011.
- [11] “Criteria for the passive house, enerphit and phi low energy building standard,” Mar 2020. [Online; accessed 22-March-2020].
- [12] J. H. Scofield, “Do leed-certified buildings save energy? not really...,” *Energy and Buildings*, vol. 41, no. 12, pp. 1386 – 1390, 2009.
- [13] F. Asdrubali, G. Baldinelli, F. Bianchi, and S. Sambuco, “A comparison between environmental sustainability rating systems leed and itaca for residential buildings,” *Building and Environment*, vol. 86, pp. 98 – 108, 2015.
- [14] W. Lee and J. Burnett, “Benchmarking energy use assessment of hk-beam, breeam and leed,” *Building and Environment*, vol. 43, no. 11, pp. 1882 – 1891, 2008.
- [15] “Leed green associate credentials,” Mar 2020. [Online; accessed 22-March-2020].
- [16] V. Olgyay and J. Herdt, “The application of ecosystems services criteria for green building assessment,” *Solar Energy*, vol. 77, no. 4, pp. 389 – 398, 2004. The American Solar Energy Society’s Solar 2003 Special Issue.
- [17] M. Kabak, E. Köse, O. Kırılmaz, and S. Burmaoğlu, “A fuzzy multi-criteria decision making approach to assess building energy performance,” *Energy and Buildings*, vol. 72, pp. 382 – 389, 2014.
- [18] BREEAM, “How breeam certification works,” 2020. [Online; accessed 16-March-2020].
- [19] G. Hundy, A. Trott, and T. Welch, “Chapter 1 - fundamentals,” in *Refrigeration, Air Conditioning and Heat Pumps (Fifth Edition)* (G. Hundy, A. Trott, and T. Welch, eds.), pp. 1 – 18, Butterworth-Heinemann, fifth edition ed., 2016.

- [20] K. Herold, R. Radermacher, and S. Klein, *Absorption Chillers and Heat Pumps*. Taylor & Francis, 1996.
- [21] R. American Society of Heating and I. Air-Conditioning Engineers, *2017 ASHRAE® Handbook - Fundamentals (SI Edition)*. American Society of Heating, Refrigerating and Air-Conditioning Engineers, Inc. (ASHRAE), 2017.
- [22] H. Perez-Blanco, “Absorption heat pump performance for different types of solutions,” *International Journal of Refrigeration*, vol. 7, no. 2, pp. 115 – 122, 1984.
- [23] R. American Society of Heating and I. Air-Conditioning Engineers, *2017 ASHRAE® Handbook - Fundamentals (SI Edition)*. American Society of Heating, Refrigerating and Air-Conditioning Engineers, Inc. (ASHRAE), 2017.
- [24] P. Holmberg and T. Berntsson, “Alternative working fluids in heat transformers,” *ASHRAE Transactions*, vol. 96, pp. 1582–1589, 1990.
- [25] J. Sun, L. Fu, and S. Zhang, “A review of working fluids of absorption cycles,” *Renewable and Sustainable Energy Reviews*, vol. 16, no. 4, pp. 1899 – 1906, 2012.
- [26] G. S. Lorenzo De Pascalis and F. Carluccio, *Handbook of Research on Advances and Applications in Refrigeration Systems and Technologies*. ASHRAE Transactions, 2015.
- [27] O. Özkan, A. Güvenç Yazıcıoğlu, and D. K. Baker, *Design and modeling of a novel rectifier with ceramic hollow fiber membrane contactor for miniaturized absorption cooling devices. [Electronic resource]*. METU, 2015.
- [28] R. American Society of Heating and I. Air-Conditioning Engineers, *2017 ASHRAE® Handbook - Fundamentals (SI Edition)*. American Society of Heating, Refrigerating and Air-Conditioning Engineers, Inc. (ASHRAE), 2017.
- [29] M. de Vega, M. Venegas, and N. García-Hernando, “Modeling and performance analysis of an absorption chiller with a microchannel membrane-based absorber using  $\text{LiBr-H}_2\text{O}$ ,  $\text{LiCl-H}_2\text{O}$ , and  $\text{LiNO}_3\text{-NH}_3$ ,” *International Journal of Energy Research*, vol. 42, no. 11, pp. 3544–3558, 2018.

- [30] M. B. K. Lei, "Evaluation of a solar-driven absorption cycle heat pump part i: Design theory, development, and basic evolution," *Transactions of the ASAE*, vol. 37, no. 4, pp. 1309–1318, 1994.
- [31] K. Herold, R. Radermacher, and S. Klein, *Absorption Chillers and Heat Pumps*. Taylor & Francis, 1996.
- [32] M. Moran, H. Shapiro, D. Boettner, and M. Bailey, *Fundamentals of Engineering Thermodynamics*. Wiley, 2010.
- [33] K. Herold, R. Radermacher, and S. Klein, *Absorption Chillers and Heat Pumps*. Taylor & Francis, 1996.
- [34] I. Ferreira, "Thermodynamic and physical property data equations for ammonia-lithium nitrate and ammonia-sodium thiocyanate solutions," *Solar Energy*, vol. 32, no. 2, pp. 231 – 236, 1984.
- [35] X. Liao and R. Radermacher, "Absorption chiller crystallization control strategies for integrated cooling heating and power systems," *International Journal of Refrigeration*, vol. 30, no. 5, pp. 904 – 911, 2007.
- [36] J. Fernández-Seara, J. Sieres, and M. Vázquez, "Heat and mass transfer analysis of a helical coil rectifier in an ammonia–water absorption system," *International Journal of Thermal Sciences*, vol. 42, no. 8, pp. 783 – 794, 2003.
- [37] L. Domínguez-Inzunza, J. Hernández-Magallanes, M. Sandoval-Reyes, and W. Rivera, "Comparison of the performance of single-effect, half-effect, double-effect in series and inverse and triple-effect absorption cooling systems operating with the  $\text{nh}_3$ – $\text{lino}_3$  mixture," *Applied Thermal Engineering*, vol. 66, no. 1, pp. 612 – 620, 2014.
- [38] B. H. Gebreslassie, M. Medrano, and D. Boer, "Exergy analysis of multi-effect water– $\text{liBr}$  absorption systems: From half to triple effect," *Renewable Energy*, vol. 35, no. 8, pp. 1773 – 1782, 2010.
- [39] R. Maryami and A. Dehghan, "An exergy based comparative study between  $\text{liBr}$ /water absorption refrigeration systems from half effect to triple effect," *Applied Thermal Engineering*, vol. 124, pp. 103 – 123, 2017.

- [40] J. Wang and D. Zheng, “Performance of one and a half-effect absorption cooling cycle of h<sub>2</sub>o/libr system,” *Energy Conversion and Management*, vol. 50, no. 12, pp. 3087 – 3095, 2009.
- [41] D. C. Erickson, “One-and-a-half effect absorption cycle,” *patent*, no. US5016444A, 1989.
- [42] D. Hong, G. Chen, L. Tang, and Y. He, “Simulation research on an eax (evaporator-absorber-exchange) absorption refrigeration cycle,” *Energy*, vol. 36, no. 1, pp. 94 – 98, 2011.
- [43] X. Yan, G. Chen, D. Hong, S. Lin, and L. Tang, “A novel absorption refrigeration cycle for heat sources with large temperature change,” *Applied Thermal Engineering*, vol. 52, no. 1, pp. 179 – 186, 2013.
- [44] D. Hong, G. Chen, L. Tang, and Y. He, “A novel ejector-absorption combined refrigeration cycle,” *International Journal of Refrigeration*, vol. 34, no. 7, pp. 1596 – 1603, 2011. Ejector Technology.
- [45] S. B. Riffat, L. Jiang, and G. Gan, “Recent development in ejector technology—a review,” *International Journal of Ambient Energy*, vol. 26, no. 1, pp. 13–26, 2005.
- [46] S. He, Y. Li, and R. Wang, “Progress of mathematical modeling on ejectors,” *Renewable and Sustainable Energy Reviews*, vol. 13, no. 8, pp. 1760 – 1780, 2009.
- [47] L. Jiang, Z. Gu, X. Feng, and Y. Li, “Thermo-economical analysis between new absorption–ejector hybrid refrigeration system and small double-effect absorption system,” *Applied Thermal Engineering*, vol. 22, no. 9, pp. 1027 – 1036, 2002.
- [48] D. Colorado and W. Rivera, “Performance comparison between a conventional vapor compression and compression-absorption single-stage and double-stage systems used for refrigeration,” *Applied Thermal Engineering*, vol. 87, pp. 273 – 285, 2015.

- [49] J. Fernández-Seara, J. Sieres, and M. Vázquez, “Compression–absorption cascade refrigeration system,” *Applied Thermal Engineering*, vol. 26, no. 5, pp. 502 – 512, 2006.
- [50] C. Cimsit and I. T. Ozturk, “Analysis of compression–absorption cascade refrigeration cycles,” *Applied Thermal Engineering*, vol. 40, pp. 311 – 317, 2012.
- [51] S. Garimella, A. M. Brown, and A. K. Nagavarapu, “Waste heat driven absorption/vapor-compression cascade refrigeration system for megawatt scale, high-flux, low-temperature cooling,” *International Journal of Refrigeration*, vol. 34, no. 8, pp. 1776 – 1785, 2011.
- [52] V. Jain, S. Kachhwaha, and G. Sachdeva, “Thermodynamic performance analysis of a vapor compression–absorption cascaded refrigeration system,” *Energy Conversion and Management*, vol. 75, pp. 685 – 700, 2013.
- [53] Y. Xu, F. Chen, Q. Wang, X. Han, D. Li, and G. Chen, “A novel low-temperature absorption–compression cascade refrigeration system,” *Applied Thermal Engineering*, vol. 75, pp. 504 – 512, 2015.
- [54] K. Dao, “Regenerative absorption cycles with multiple stage absorber,” 1991.
- [55] K. W. Kauffman, “Variable effect absorption machine and process.”
- [56] W. J. Biermann, “Variable effect desorber-resorber absorption cycle.”
- [57] A. Lecuona, R. Ventas, C. Vereda, and R. López, “Absorption solar cooling systems using optimal driving temperatures,” *Applied Thermal Engineering*, vol. 79, pp. 140 – 148, 2015.
- [58] S. B. Celik, A. Lecuona-Neumann, P. A. Rodriguez-Aumente, and A. Famiglietti, “Modelling of an absorption cycle with a direct ammonia vapor generator inside a concentrating parabolic trough solar collector,” *EuroSun 2018 Conference Proceeding*, 2018.
- [59] L. Kairouani and E. Nehdi, “Cooling performance and energy saving of a compression–absorption refrigeration system assisted by geothermal energy,” *Applied Thermal Engineering*, vol. 26, no. 2, pp. 288 – 294, 2006.

- [60] J. Koehler, W. J. Tegethoff, D. Westphalen, and M. Sonnekalb, "Absorption refrigeration system for mobile applications utilizing exhaust gases," *Heat and Mass Transfer*, vol. 32, no. 5, pp. 333–340, 1997.
- [61] F. Táboas, M. Bourouis, and M. Vallès, "Analysis of ammonia/water and ammonia/salt mixture absorption cycles for refrigeration purposes in fishing ships," *Applied Thermal Engineering*, vol. 66, no. 1, pp. 603 – 611, 2014.
- [62] D. Barlev, R. Vidu, and P. Stroeve, "Innovation in concentrated solar power," *Solar Energy Materials and Solar Cells*, vol. 95, no. 10, pp. 2703 – 2725, 2011.
- [63] F. Assilzadeh, S. Kalogirou, Y. Ali, and K. Sopian, "Simulation and optimization of a lib solar absorption cooling system with evacuated tube collectors," *Renewable Energy*, vol. 30, no. 8, pp. 1143 – 1159, 2005.
- [64] A. Lecuona-Neumann, R. Ventas-Garzón, V. Vereda-Ortiz, and M. Legrand, "Linear tube solar receiver as stratified flow vapor generator/separators for absorption machines using  $\text{NH}_3/\text{LiNO}_3$ ," *ISES*, 2016.
- [65] A. Famiglietti, A. Lecuona, J. I. Nogueira, and B. Celik, "Direct ammonia vapor generation inside a concentrating parabolic trough solar collector for an ammonia/lithium nitrate absorption machine. theoretical study," *13th IIR Gustav Lorentzen Conference*, 2018.
- [66] Y. Nakayama and R. Boucher, "8 - flow in a water channel," in *Introduction to Fluid Mechanics* (Y. Nakayama and R. Boucher, eds.), pp. 136 – 147, Oxford: Butterworth-Heinemann, 1998.
- [67] D. Barr, "Discussion of accurate explicit equation for friction factor," *J. Hydraul. Div., Am. Soc. Civ. Eng.*, vol. 103, no. HY3, 1977.
- [68] B. C. Yen, "Channel flow resistance : centennial of manning's formula," (Littleton, Colo.), Water Resources Pub., 1991.
- [69] N. H. Chen, "An explicit equation for friction factor in pipe," *Industrial & Engineering Chemistry Fundamentals*, vol. 18, no. 3, pp. 296–297, 1979.

- [70] D. a. BARR, “Technical note. solutions of the colebrook-white function for resistance to uniform turbulent flow.,” *Proceedings of the Institution of Civil Engineers*, vol. 71, no. 2, pp. 529–535, 1981.
- [71] M. O. E. S. A. P. D. B. P. Michel, “Bottom friction formulations for free surface flow modeling,” *8th NCTAM Congress*, 2009.
- [72] J. A. Swaffield and S. Bridge, “Applicability of the colebrook-white formula to represent frictional losses in partially filled unsteady pipeflow,” *Journal of Research of the National Bureau of Standards*, vol. 88, 1983.
- [73] P. I. Frank, P. D. David, L. B. Theodore, and S. L. Adrienne, *Fundamentals of Heat and Mass Transfer*. John Wiley & Sons, 6 ed., 2007.
- [74] I. E. Idelchik, *Handbook of Hydraulic Resistance*. Jaico Publishing House, 3 ed., 2005.
- [75] ISO, “Iso 9806:2017(en),” *International Standards Office*, 2017.
- [76] K. E. Gungor and R. H. S. Winterton, “A general correlation for flow boiling in tubes and annuli,” *International Journal of Heat and Mass Transfer*, vol. 29, 1986.
- [77] K. Stephan and M. Abdelsalam, “Heat-transfer correlations for natural convection boiling.,” *International Journal of Heat and Mass Transfer*, vol. 23, 1980.
- [78] Ünal H. C., “Prediction of nucleate pool boiling heat transfer coefficients for binary mixtures,” *International journal of heat and mass transfer*, 1986.
- [79] H. Kretzschmar, “Property library for ammonia libnh3 fluidmat for mathcad,” 2016.
- [80] S. Libotean, D. Salavera, M. Valles, X. Esteve, and A. Coronas, “Vapor-liquid equilibrium of ammonia + lithium nitrate + water and ammonia + lithium nitrate solutions from (293.15 to 353.15) k,” *Journal of Chemical & Engineering Data*, vol. 52, no. 3, pp. 1050–1055, 2007.
- [81] S. Libotean, A. Martín, D. Salavera, M. Valles, X. Esteve, and A. Coronas, “Densities, viscosities, and heat capacities of ammonia + lithium nitrate and



- ammonia + lithium nitrate + water solutions between (293.15 and 353.15) K,” *Journal of Chemical & Engineering Data*, vol. 53, no. 10, pp. 2383–2388, 2008.
- [82] L. G. Farshi, C. I. Ferreira, S. Mahmoudi, and M. Rosen, “First and second law analysis of ammonia/salt absorption refrigeration systems,” *International Journal of Refrigeration*, vol. 40, pp. 111 – 121, 2014.
- [83] “Index,” in *Concentrating Solar Power Technology* (K. Lovegrove and W. Stein, eds.), Woodhead Publishing Series in Energy, pp. 662 – 674, Woodhead Publishing, 2012.
- [84] H. W. F. Tillner-Roth R and B. H. D., *A new fundamental equation for ammonia; Eine neue Fundamentalgleichung fuer Ammoniak*. Deutscher Kaelte- und Klimatechnischer Verein e.V., Stuttgart (Germany), Dec 1994.
- [85] “F-chart software.” <http://www.fchartsoftware.com/>. Accessed: 11/04/2020.
- [86] R. López, A. Lecuona, R. Ventas, and J. Nogueira, “1-d transient numerical modeling of counter-current two-phase stratified flow inside a medium temperature solar linear collector,” *Energy Conversion and Management*, vol. 155, pp. 218 – 229, 2018.
- [87] B. Şahin, M. Bilgili, A. Çetingöz, and N. Kurtulmuş, “Mersin İli için güneş enerji destekli absorpsiyonlu soğutma sisteminin performans analizi,” *Çukurova Üniversitesi Mühendislik-Mimarlık Fakültesi Dergisi*, vol. 32, pp. 187 – 196, 2017.
- [88] B. U. S. of Public Health, “Confidence intervals.” [Online; accessed 21-June-2020].
- [89] A. E. de Meteorología, “Standard climate values. madrid, retiro.,” March 2018. [Online; accessed 16-March-2018].
- [90] M. Mazloumi, M. Naghashzadegan, and K. Javaherdeh, “Simulation of solar lithium bromide–water absorption cooling system with parabolic trough collector,” *Energy Conversion and Management*, vol. 49, no. 10, pp. 2820 – 2832, 2008.

- [91] C. Tzivanidis and E. Bellos, “The use of parabolic trough collectors for solar cooling – a case study for athens climate,” *Case Studies in Thermal Engineering*, vol. 8, pp. 403 – 413, 2016.
- [92] J. Cerezo, R. Romero, J. Ibarra Bahena, A. Rodríguez-Martínez, G. Montero, and A. Acuña, “Dynamic simulation of an absorption cooling system with different working mixtures,” *Energies*, vol. 11, 01 2018.
- [93] R. Ventas, A. Lecuona, A. Zacarías, and M. Venegas, “Ammonia-lithium nitrate absorption chiller with an integrated low-pressure compression booster cycle for low driving temperatures,” *Applied Thermal Engineering*, vol. 30, no. 11, pp. 1351 – 1359, 2010.
- [94] G. A. Zuniga, *Layer of protection analysis applied to ammonia refrigeration systems*. Texas A&M University, 2008. Master’s thesis.
- [95] B. Bolaji and Z. Huan, “Thermodynamic analysis of performance of vapour compression refrigeration system working with r290 and r600a mixtures,” *Scientia Iranica*, vol. 20, pp. 1720–1728, 08 2013.
- [96] R. Ventas, C. Vereda, A. Lecuona, M. Venegas, and M. del Carmen Rodríguez-Hidalgo, “Effect of the nh<sub>3</sub>–lino<sub>3</sub> concentration and pressure in a fog-jet spray adiabatic absorber,” *Applied Thermal Engineering*, vol. 37, pp. 430 – 437, 2012.

## **APPENDIX A**

### **TECHNICAL DRAWINGS**



**Curvas características**

Q= Caudal en m<sup>3</sup>/h, m<sup>3</sup>/s y cfm.

Pe= Presión estática en mmH<sub>2</sub>O, Pa e inwg.

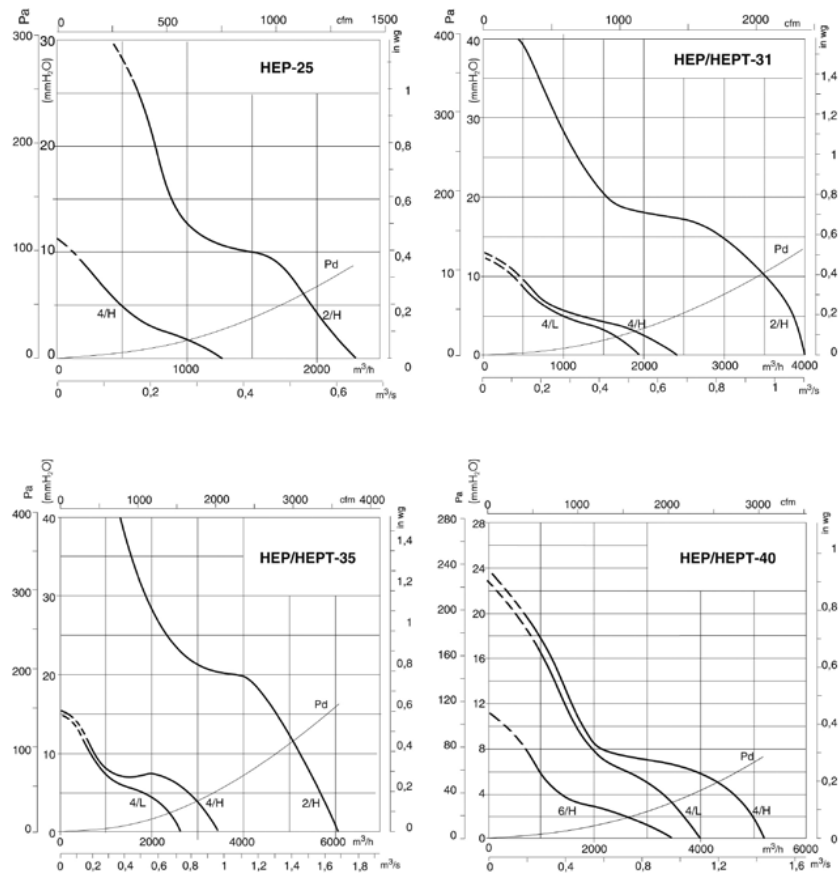


Figure A.2: Condenser

## EVAPORADOR - 50 Hz

Fecha 21/09/2012  
 Cliente AD6265-D  
 Referencia AD6265-D

**Modo de operación** Amoníaco Bomba- **Tipo de** Airmax II **Modelo** ILBH501BS  
 Tipo de calculo Rating

Capacidad calculada 5.15 kW

### Dimensiones

Longitud	1430 mm	Peso Estándar	103 kg
Altura	946 mm		
Fondo	801 mm		
Embalaje	Jaula	Volumen embalaje	2.0 m³

### Datos térmicos

Refrigerante	Ammonia
Temperatura del aire	-25.0 °C / -26.7 °C
Humedad relativa	85.0 %
Temp. de evaporación	-31.0 °C
Diferencia de temperatura	6.0 K DT1

### Datos de ventiladores

Caudal de aire:	7724 m³/h	Número de ventiladores	1
Tiro de aire	33.9 m	Diámetro del ventilador	500.0 mm
Velocidad de rotación	1210 rpm	Voltaje	230V
Potencia nominal total	770 W	Alimentación	1ph
Corriente nominal total <sup>(2)</sup>	3.4 A	Conexión	-
Total Corriente Plena Carga	4.1 A		
Presión sonora (3.0 m) <sup>(1)</sup>		53 dB(A)	
Potencia sonora		74 dB(A)	

### Datos batería

Material del tubo	Ac. Inoxidable	Material aletas	Aluminio
Separación de aletas	10.0 mm	Número de circuitos	5
Superficie	39.6 m²	Volumen interno	10.1 litros
Conexiones (In-Out)	1" - 1 1/2"	Lado conexiones	Izquierda - estándar

### Bastidor y Carcasa

Material de la carcasa	Acero galvanizado
Coil frame material	Aluzinc

### NOTAS

<sup>(1)</sup> Usando EN 13487 a 3m en condiciones de campo abierto

<sup>(2)</sup> Corriente nominal para Taire=20°C. Puede haber variaciones, debido a diferente tensión o Taire

<sup>(5)</sup> Single electrical heater 230V

Figure A.3: Evaporator

# Micro Motion® Series 1000 and Series 2000 Transmitters with MVD™ Technology

Micro Motion® Series 1000 and Series 2000 transmitters with MVD™ technology deliver powerful features that make managing your process easier.

**Advanced architecture with flexible installation options**

- Integral or remote mounting provides maximum flexibility
- Cost-effective 4-wire interface reduces installation costs
- Remote field mount models available with stainless steel housing for harsher environments
- DIN rail option reduces complexity and increases versatility



**Wide variety of I/O and application capabilities to fit your needs**

- High-speed DSP for accuracy under the toughest conditions—entrained gas, high noise, high turndown, and more
- Concentration and net flow measurement eliminate the need for additional instruments
- Approved for custody transfer and certified for SIL2 and SIL3, which provides measurement confidence and reliability
- WirelessHART® option allows you to gain access to additional diagnostics and process information without added wiring costs

2200S	2400S	1700 2700	1500 2500	3300 3350	3500 3700	5700
Compact integral 2-wire transmitter	Compact integral transmitter	Versatile field- mount transmitter	Compact control- room transmitter	Frequency-input discrete controller	Integrated control and measurement platform	Advanced field - mount transmitter

MICRO MOTION®



Figure A.4: Flowmeter

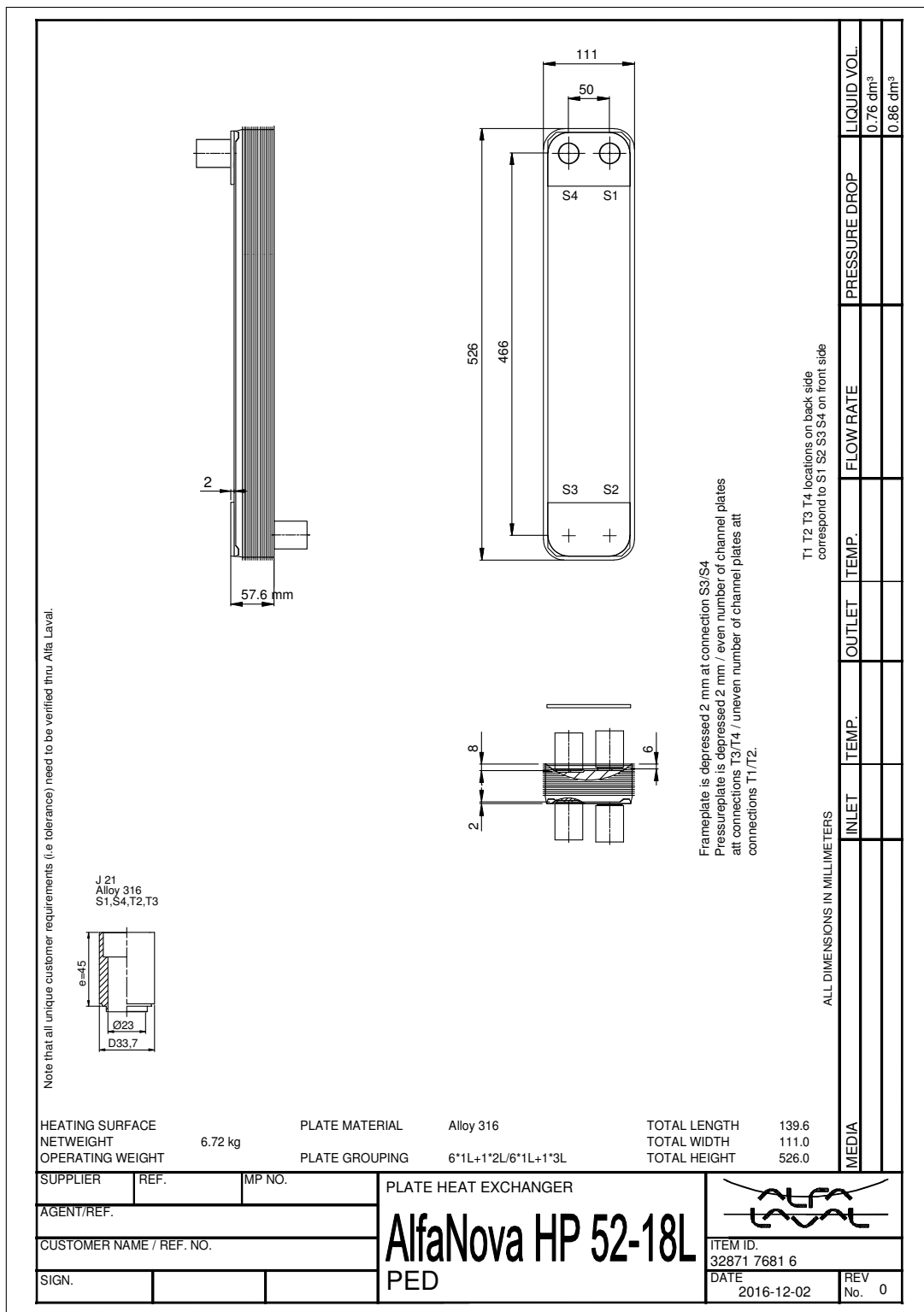




Figure A.5: Heat Exchanger



Operating instructions  
Betriebsanleitung  
Mode d'emploi  
Manual de instrucciones

Pressure transmitter model A-10	GB
Druckmessumformer Typ A-10	D
Transmetteur de pression type A-10	F
Transmisor de presión modelo A-10	E



Pressure transmitter model A-10


  
Part of your business

Figure A.6: Pressure Sensor



## Pump Technicals - PCP

### "Duty Parameters"

Fluid	: CHEMICALS	Flow Rate (l/hr.)	: 179.28
Chemical Composition	:	Suction Pressure / Head	:
Specific Gravity	: 1	Discharge Pressure (Kg/Cm2)	:
P.H. Value	: -	Differential Pressure (Kg/Cm2)	: 24.00
Size Of Solid (mm) /%	:	NPSH (A) (Mt)	: 8
Nature Of Solid	:	Running Hours Per Day	:
Pumping Temp (°C)	: 25	Type Of Duty	:
Viscosity (CST)	: 5 - 5	Type Of Location	:

### "Pump Operating Parameters"

Pump Model	: RDCA494E7CF1L	Pump Design	:
Absorbed Power (KW)	: 0.72	Type of Joint	: Universal Cardan Joint with 24 Mths Warranty
Pump Speed (Rpm)	: 281.00	Rec. Prime Mover Rating (KW)	:
NPSH (R) (Mt)	: 1.6	Direction Of Rotation	: CCW (Suction on Gland)
Volumetric Efficiency	: 29.51%	Starting Method	: Direct on Line
Mechanical Efficiency	: 16.47%	Starting Torque (N-m)	: 30.90 N-m
Disc. Connection/ Size	: Flange/ 50 mm	Running Torque (N-m)	: 24.63 N-m
Disc. Location/ Rating/ Facing	: End/ BS:4504/ RF		:
Suc. Location/ Rating/ Facing	: Top/ BS:4504/ RF		:
Suc. Connection/Size	: Flange/ 50 mm		:
Rubbing Velocity (meter/sec)	: 0.44		:
Partical Velocity (meter/sec)	: 0.28		:
Drive Type	: Direct Drive Geared-Motor 4poles NORD 1,5kW, SK172.1(F)-90LH/4(TF), i:5.14, 400V, 50Hz, 3ph, IP55, with PTC's		

### "Material of Construction"

Pump Latern	: Cast Stainless Steel CF8M as per ASTM A351 (cast SS316)
Pump Housing	: Cast Stainless Steel CF8M as per ASTM A351 (cast SS316)
Rotor	: Stainless Steel AISI 316 (IS:2553) - HCP
Shaft	: Stainless Steel AISI 316 (IS:2553) - HCP
Stator	: RE-EPDM Black

### "Shaft Sealing Arrangement"

Type Of Gland Packing	:
Lantern Ring Location	:
Make of Meachnical Seal / seals	: Mechanical seal SiC-SiC / EPDM

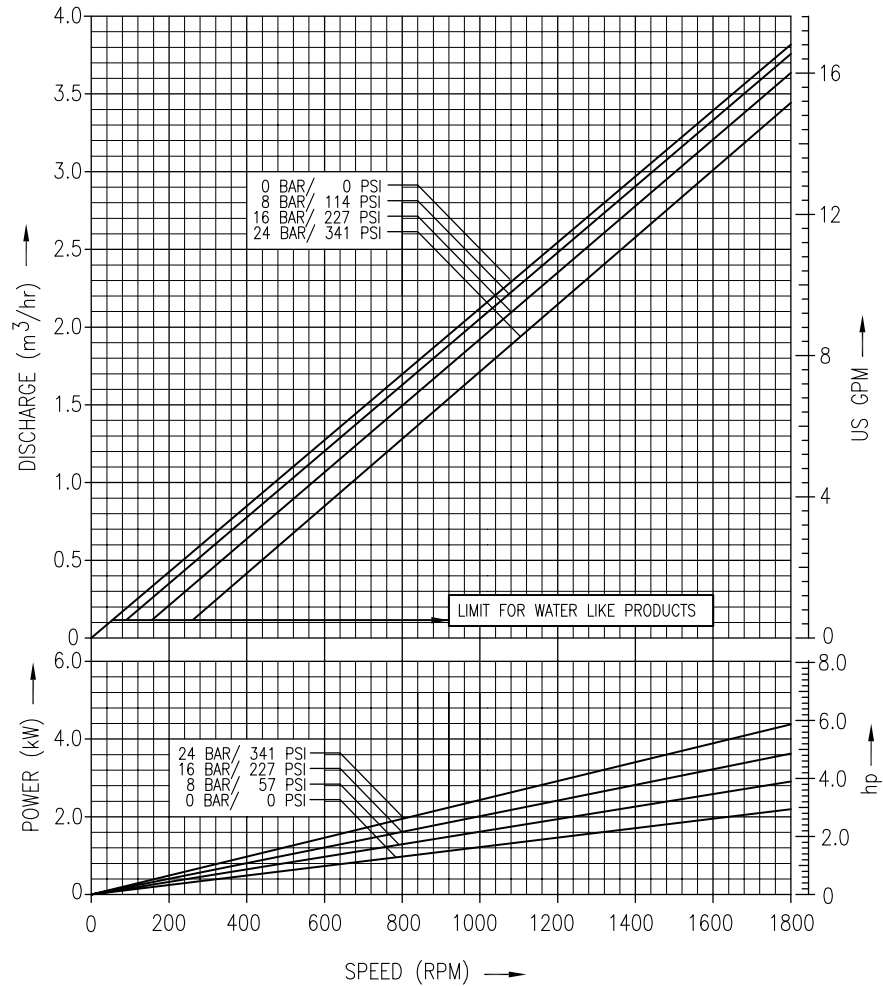
We recommend the use of relief valve immediately after pump discharge.

Figure A.7: Pump



**ROTO PUMPS LTD.**  
PERFORMANCE CURVE

PUMP MODEL: D 494	
GRAPH NO: R-S-376-05	
STARTING TORQUE	30 Nm
	22 Lb-ft.



NOTE:

1. TESTED ON WATER AT 20°C FOR RA & RR STATOR.
2. TOLERANCE ACCORDING TO VDMA 24284 TABLE 5, GROUP II.
3. PSI VALUES ROUNDED OFF TO NEAREST ZERO.

Figure A.8: Performance Curve of the Pump

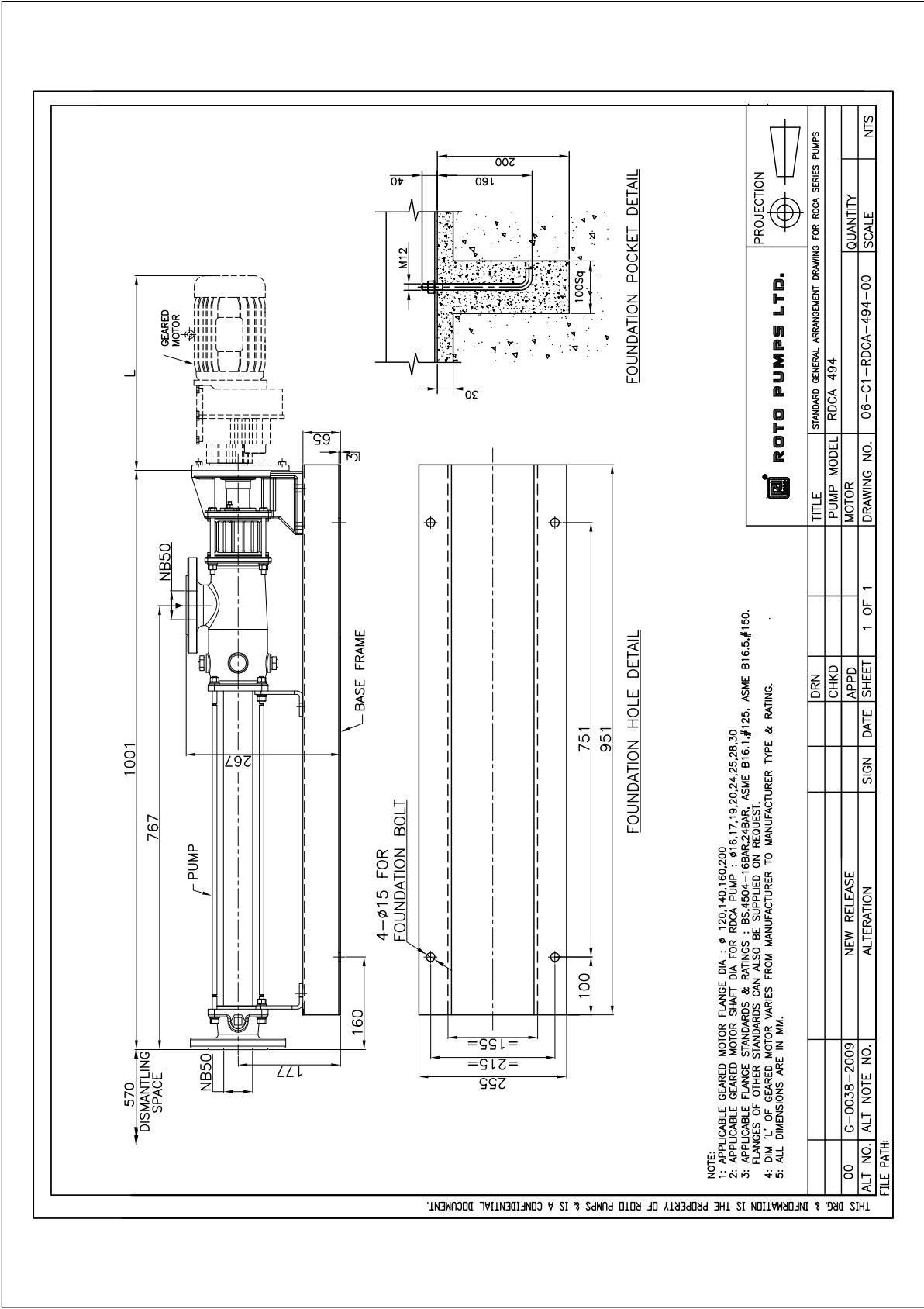


Figure A.9: Technical Drawing of the Pump

## Performance specifications

### Reference operating conditions

For determining the performance capabilities of our meters, the following conditions were observed/utilized:

- Water at 68 to 77 °F and 14.5 to 29 psig (20 to 25 °C and 1 to 2 barg)
- Accuracy based on industry leading accredited calibration stands according to ISO 17025
- All models have a density range up to 5 g/cm<sup>3</sup> (5000 kg/m<sup>3</sup>)

### Accuracy and repeatability on liquids and slurries

Performance Specification	Standard	Optional <sup>(1)</sup>
Mass/volume flow accuracy <sup>(2)(3)</sup>	±0.10% of rate	±0.05% of rate
Mass/volume flow repeatability	±0.05% of rate	±0.025% of rate
Density accuracy <sup>(4)(5)</sup>	±0.0005 g/cm <sup>3</sup> (±0.5 kg/m <sup>3</sup> )	±0.0002 g/cm <sup>3</sup> (±0.2 kg/m <sup>3</sup> )
Density repeatability	±0.0002 g/cm <sup>3</sup> (±0.2 kg/m <sup>3</sup> )	±0.0001 g/cm <sup>3</sup> (±0.1 kg/m <sup>3</sup> )
Temperature accuracy	±1 °C ±0.5% of reading	
Temperature repeatability	±0.2 °C	

(1) Optional accuracy is not available for high temperature models (base model code A/B) or high capacity models (CMFHC2/3/4)

(2) Stated flow accuracy includes the combined effects of repeatability, linearity, hysteresis, and orientation.

(3) For cryogenic applications, liquid accuracy is ±0.35% of rate.

(4) The standard density accuracy option for the sensor models CMFS010, CMFS015 is ±0.002 g/cm<sup>3</sup> (±2 kg/m<sup>3</sup>), optional accuracy is ±0.0005 g/cm<sup>3</sup> (±0.5 kg/m<sup>3</sup>).

(5) The standard density accuracy option for the sensor model CMFS007 is ±0.002 g/cm<sup>3</sup> (±2 kg/m<sup>3</sup>).

### Accuracy and repeatability on gases

Performance specification	CMF models	CMFS models
Mass flow accuracy	±0.35% of rate	±0.25% of rate
Mass flow repeatability	±0.20% of rate	
Temperature accuracy	±1 °C ±0.5% of reading	
Temperature repeatability	±0.2 °C	

Figure A.10: Accuracy of the Pump



## OPTIFLEX 1300 C Hoja de datos técnica

Transmisor de nivel de radar guiado (TDR) para aplicaciones complejas de nivel y de interfase

- Equipo universal que puede medir el nivel de líquidos, pastas, granulados, polvo e interfase de líquidos
- Fácil de instalar: no requiere calibración in situ
- Opera hasta 300 bar / 4350 psi

**HART**   
COMMUNICATION PROTOCOL



© KROHNE 11/2015 - 4001102503 - TD OPTIFLEX 1300 R13 es

**KROHNE**

Figure A.11: Measure of the Tank level

Pantalla e interfaz de usuario	
Pantalla	Pantalla LCD
	9 líneas, 160 × 160 píxeles en escala de grises de 8 bits, con teclado con 4 botones
Idiomas de la interfaz	Inglés, alemán, francés, italiano, español, portugués, japonés, chino simplificado y ruso

**Precisión**

Resolución	1 mm / 0,04"
Repetibilidad	±1 mm / ±0,04"
Precisión (en el modo directo)	<b>Líquidos:</b> ±3 mm / ±0,12", cuando la distancia es < 10 m / 33 ft; ±0,03% de la distancia medida cuando la distancia es > 10 m / 33 ft <b>Polvos:</b> ±20 mm / ±0,8" <b>Interfase:</b> ±10 mm / ±0,4" (constante cr) ±20 mm / ±0,8" (constante cr)
Precisión (en el modo TBF)	±20 mm / ±0,8" (constante cr)
Capa mínima (interfase)	50 mm / 2"
<b>Condiciones de referencia según EN 60770</b>	
Temperatura	+20°C ±5°C / +68°F ±10°F
Presión	1013 mbara ±20 mbar / 14,69 psia ±0,29 psi
Humedad relativa del aire	60% ±15%

**Condiciones de funcionamiento**

Temperatura	
Temperatura ambiental	-40...+80°C / -40...+176°F Ex: consulte las instrucciones de funcionamiento adicionales o los certificados de aprobación
Temperatura de almacenamiento	-40...+85°C / -40...+185°F
Temperatura de la conexión de proceso	<b>Estándar</b> -50...+200°C / -58...+392°F (según los límites de temperatura del material de la junta. Consulte "Materiales" en esta tabla). Ex: consulte las instrucciones de funcionamiento adicionales o los certificados de aprobación) ② <b>Versiónes de alta temperatura (HT) y alta temperatura / alta presión (HT/HP) con juntas FKM/FPM y Kalrez® 6375</b> +300°C / +572°F (sólo sonda mono-cable Ø2 mm / 0,08") Ex: consulte las instrucciones de funcionamiento adicionales o los certificados de aprobación) ② <b>Versiónes HT y HT/HP con juntas EPDM</b> +250°C / +482°F (sólo sonda mono-cable Ø2 mm / 0,08") Ex: consulte las instrucciones de funcionamiento adicionales o los certificados de aprobación) ②

Figure A.12: Accuracy of the Tank Level





# CV

Sitki Berat Celik  
Istanbul/Turkey  
+90 552 281 8889  
[beratcelik@gmail.com](mailto:beratcelik@gmail.com)  
September, 2020

Education	<b>Doctor of Philosophy, PhD</b>	2012-2020
	Mechanical Engineering, Middle East Technical University (METU), Turkey <b>Thesis Title:</b> Performance evaluation of linear tube solar receiver as stratified flow vapor generator/separator for absorption machines using $\text{NH}_3/\text{LiNO}_3$ <b>Field:</b> Solar Energy, CSP, Adsorption, Absorption, Experimental Heat Transfer and Fluid Mechanics, CFD	
	<b>Master of Science, MSc</b>	2010-2012
	Mechanical Engineering, Middle East Technical University, Turkey <b>Thesis Title:</b> Analysis of single phase fluid flow and heat transfer in slip flow regime by parallel implementation of the Lattice Boltzmann Method on GPUs. <b>Industrial applications</b> of the thesis are about Microelectromechanical Systems, Heat Removal Systems, Micro Injectors, Cell Separation and Counting, DNA Replication, Micro mechanical Valves, Fluid Meters, CFD Design and Programming.	
	<b>Bachelor of Science, BSc</b>	2006-2010
	Mechanical Engineering, Middle East Technical University, Cyprus	
Career Interests	Solar Energy, CSP, CFD, FEM, LBM, Experimental and Mathematical Analysis of Thermo-fluid Designs, MEMS and Lab-on-a-Chip Devices	
Professional Experience	<b>Visitor Researcher</b>	2017-2018
	in Universidad Carlos III de Madrid	
	<b>Researcher</b>	2015-2017
	in the heat transfer laboratory of METU	
	<b>Teaching &amp; Research Assistant</b>	2011-2015
	in the Mechanical Eng. dept. of METU Assisting courses in the field of fluid mechanics and heat transfer	
	<b>Research Assistant</b>	2010-2012
	in a project of Scientific and Technological Research Council of Turkey (TUBITAK)	
	<b>The courses tutored:</b> Numerical Methods in Engineering, Introduction to Finite Element Method, Fluid Mechanics, Advanced Boundary Layer, Fluid Mechanics Laboratories, Heat Transfer, Heat Transfer Laboratories, Thermodynamics, Technical Drawing	
Volunteer Work	<b>Erasmus Student Network (ESN)</b>	2010-2017
	Erasmus Student Network is the biggest interdisciplinary student associations in Europe. It aims to support and develop student exchange. <a href="http://www.esn.org">www.esn.org</a> <b>Board Member of ESN Turkey</b>	2013-2014
	Governmental relations via National Agency and Ministry for EU Affairs. ESNinBusiness Project: Meeting the leading companies with the human resource in the network. Strategic Planning of ESN Turkey.	
Honors & Awards	Scholarship of Scientific and Technological Research Council of Turkey	2017-2018
	Scholarship of Scientific and Technological Research Council of Turkey	2010-2011
	Honor Standing in Undergraduate School	2009-2010
	National Scholarship throughout the secondary education	2000-2003